SIMULATION AND BALLOON-BORNE OBSERVATION OF ENERGETIC RADIATION AND ELECTROMAGNETIC FIELDS FROM THUNDERSTORMS AND LIGHTNING

BY

MAHDI BAGHERI

B.S. in Physics, Isfahan University of Technology, Iran, 2010
M.S. in Physics, University of Tehran, Iran, 2013

DISSERTATION

Submitted to the University of New Hampshire
in Partial Fulfillment of
the Requirements for the Degree of

Doctor of Philosophy

in

Physics

September 2019

This dissertation has been examined and approved in partial fulfillment of the requirements for the degree of Doctor of Philosophy in Physics by:

Dissertation Director, Joseph R. Dwyer,
Professor of Physics and Space Science

Ningyu Liu,
Associate Professor of Physics and Space Science

Mark L. McConnell,
Professor of Physics and Space Science

Marc Lessard,
Associate Professor of Physics and Space Science

Karsten Pohl,
Professor of Physics and Material Science

on June 10, 2019.

Original approval signatures are on file with the University of New Hampshire Graduate School.

To my beloved parents, ***Soraya*** *and* ***Karim****, for their unending love and absolute support.*

ACKNOWLEDGMENTS

I would like to take some time to thank all the people without whom this work would never have been possible. First and foremost, my heartiest gratitude to my supervisor, Prof. Joseph R. Dwyer. I greatly appreciate the freedom you have given me to find my own path and the guidance and support you offered when needed. Your straightforward criticism combined with heart-warming support have given me great confidence as a researcher, and at the same time made me realize that I am only a beginner in this exciting profession.

I am thankful to the members of my committee, Prof. Mark McConnell, Dr. Ningyu Liu, Prof. Marc Lessard and Prof. Karsten Pohl for their friendly guidance, brilliant comments and thoughtful suggestions. Furthermore, I would like to thank Prof. Hamid K. Rassoul for his infinite support and kindness during three years of balloon campaign.

I am extremely thankful to my parents, Karim and Soraya, for giving birth to me at the first place and supporting me spiritually throughout my life. I am also thankful to my sisters and brothers for their inexhaustible encouragement and support throughout my life. I thank Mr. Christopher F. Sterpka for his true friendship, exciting discussions and everything I learned from him. I also thank my friends at the University of New Hampshire, Iman, Masoumeh and Shokoufeh for all the great moments we had together.

I would like to express my deepest appreciation to my beloved wife, Farzane, who spent sleepless nights with me and was always my support in the moments when there was no one to answer my queries. We started this amazing journey together and we are ending it together. Her support and encouragements were in the end what made this dissertation possible.

I would also like to thank the National Science Foundation (NSF) for their financial support. This work was supported by NSF awards AGS-1519236 and AGS-1618457.

TABLE OF CONTENTS

LIST OF TABLES

Table **Page**

LIST OF FIGURES

Figure **Page**

ABSTRACT

Simulation and Balloon-Borne Observation of Energetic Radiation and Electromagnetic Fields from Thunderstorms and Lightning

by

Mahdi Bagheri
University of New Hampshire, September, 2019

With more than 250 years after Benjamin Franklin's experiments, we still do not know how lightning works at the most fundamental levels. Recently, observations of high energy radiations produced during lightning activities, such as TGFs, X-rays and Gamma-ray Glows, have opened a new path for the study of lightning-related phenomena known as High-Energy Atmospheric Physics. TGFs are short and bright bursts of gamma rays associated with the early stages of positive intra-cloud lightning, while gamma-ray glows are long lasting emissions of gamma rays which would be terminated by the occurrence of lightning flash. It has been suggested that these radiations are produced by the bremsstrahlung radiation of energetic electrons, known as runaway electrons, that are accelerated by the ambient electric field inside thunderclouds. In this thesis, we have performed Monte Carlo simulations and developed balloon-borne experiments to understand and characterize the spectral and temporal properties of TGFs and Gamma-ray Glows.

In Chapter 2, we used REAM Monte Carlo simulation to investigate the generation and propagation of runaway electrons and gamma-ray flashes through Venus middle and upper clouds. We found out that similar avalanche length, energy spectrum and electric field threshold would be expected from Venus middle clouds compared to that at the sea level of the Earth. It seems if electrification occurs in the clouds of Venus, and the gamma-ray flashes initiate in the middle and upper clouds are similar to that on the Earth, they should be detectable by spacecrafts at low-Venus orbit. We propose calling these events Venusian Gamma-ray Flashes (VGFs).

One of the challenges with the TGFs is the disentanglement of the source altitude and the width and direction of the gamma-ray beam using single point spacecraft measurements, which

has hampered attempts to constrain TGF models. In Chapter 3, we have modified the REAM code to record the linear polarization of X-rays and gamma rays as a function of source altitude and beam geometry. We found that TGFs seen in space have polarizations as high as 10%, but because only a few tens of counts are typically detected by spacecraft, detecting this level of polarization is unlikely. Furthermore, very low-altitude ground-level TGFs showed a maximum polarization of 13% on the ground, with the TGF's fluence being large enough for polarimetry. The polarization degree reached its maximum further away from the z-axis as the TGF's beam broadened.

Another mystery about TGFs is their temporal distribution. Recent observations of TGFs by spacecrafts show significantly longer duration than predicted by the existing models which are affected by deadtime and pulse pileup. This raises this question: what is the actual timescale of TGFs at the source and what processes cause its duration to be prolonged in space? In Chapter 4, we have investigated the effect of beam geometry and source altitude on the spectral and temporal distribution of TGFs seen in space. Our results suggest that incompressible time dispersion caused by Compton scattering for instantaneous sources is about 20 μs at 300 km distance which is about 2.5 times smaller than what it was thought before.

One of the greatest unsolved problems in the atmospheric sciences is lightning initiation. Since the electric field threshold for the production of gamma-ray glows is less than the threshold for streamers to form, it is expected that lightning initiation should be preceded by gamma-ray glows. In Chapter 5, we have designed balloon-borne instrumentation for flying into thunderstorms with the aim of detecting gamma-ray glows. The instrumentation includes one BGO scintillator coupled to a Silicone Photomultiplier, two Geiger-Muller tubes, and an electric field mill, designed to measure both polarity and amplitude of the vertical electric field inside the thunderclouds. The insertion of scintillator between two GM tubes along with the electric field's polarity helps us to differentiate between gamma rays, electrons and positrons. We have conducted several test flights of this system during the summers of 2017 and 2018 and their result are provided.

CHAPTER 1

INTRODUCTION

1.1 Lightning Phenomenology

Lightning is one of the most energetic geophysical phenomena, producing the brightest light and loudest sound commonly occurring on Earth. Because of its high rate of occurrence ($\sim$ 100 discharges per second, 8 million discharges per day, or 6 $km^{-2}yr^{-1}$), one might think lightning is well understood, but that is not the case. Over the last century, there has been enormous progress towards our understanding of lighting phenomenology. However, lightning's seemingly random occurrence in space and time and the wide range of its significant time variation, from tens of nanoseconds for many individual processes to more than a second for the total discharge, and its obscuration by the thundercloud producing it makes lightning particularly difficult to study *[Dwyer and Uman, 2014]*.

Lightning is a kilometer-scale transient high-current electric discharge which is mostly produced by electrified thunderclouds. The main electrification mechanism for a thundercloud is suggested to be based on the collisions between soft hail (graupel) particles and small crystals of ice in the presence of unfrozen super-cooled water droplets. In this process, positively charged ice crystals are moved via updrafts to the upper part of the thundercloud ($\sim$ 10 km altitude); while the negatively charged hail forms at lower altitudes (6 – 8 km). An isolated mature thundercloud consists of tens of Coulombs of positive charge in the main positive charge region and somewhat similar negative charge in the main negative charge region. In addition to these two charge regions, a small positive charge region is found below the main negative charge which is suggested to be due to corona discharge originating from the ground and collisions between different types of precipitation particles at temperatures above 0°C (see Figure 1.1). The charge structure of a

thunderstorm is much more complex than illustrated in Figure 1.1 and varies from storm to storm *[Dwyer and Uman, 2014]*.

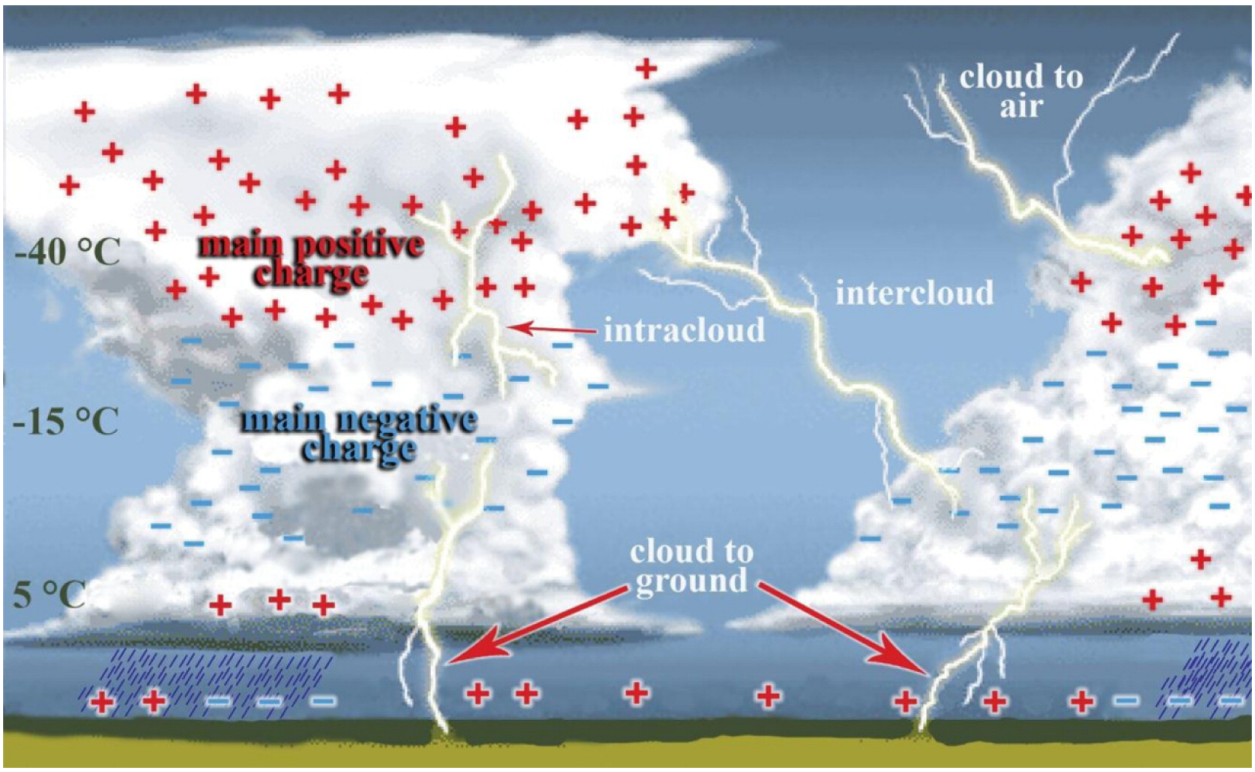

Figure 1.1: The charge structure of two simple isolated thunderclouds, representing the three main charge regions along with different types of lightning discharges.

Lightning activities are typically categorized as cloud-to-cloud (CC) and cloud-to-ground (CG) discharges, where more than 75% of them are associated with CC discharges. CG discharges could also be categorized by the sign of electrical charge carrier and direction of propagating leader as: (a) Downward negative, (b) Upward positive (c) Downward positive and (d) Upward negative which are pictured in Figure 1.2 respectively. About 90% of CG lightning flashes are downward negative, with the rest 10% being downward positive. The other two types are relatively uncommon and are upward initiated from mountaintops, tall man-made towers, or other tall objects, towards the cloud charge regions *[Dwyer and Uman, 2014]*.

Downward negative lightning as the most common type of CG flashes starts with a local discharge between the bottom of main negative charge region and small lower positive charge region underneath it, which provides free electron that are extremely mobile compared to heavier ionized

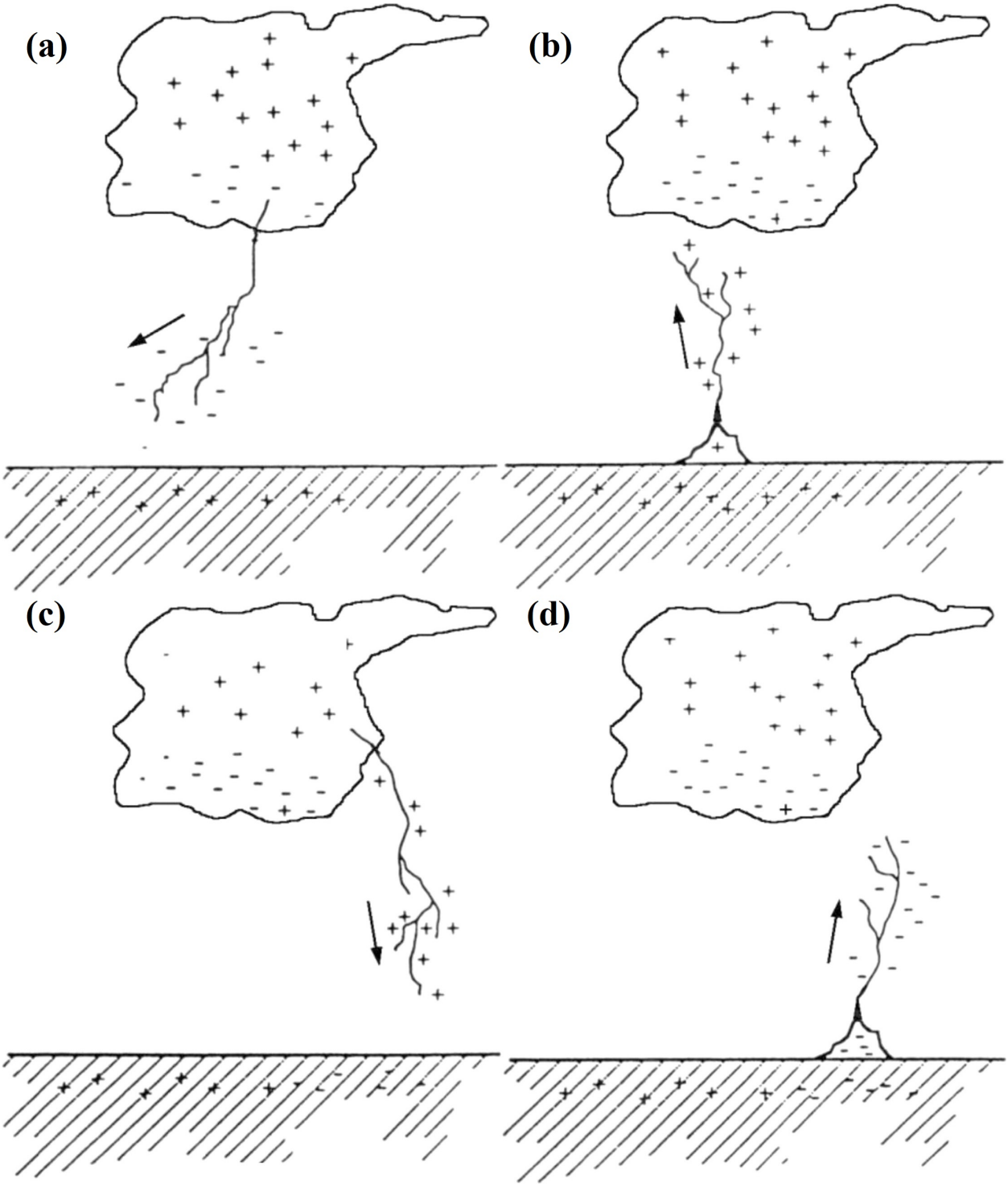

Figure 1.2: Types of cloud-to-ground lightning flashes categorized based on the sign of electrical charge and direction of the leader as: (a) Downward negative, (b) Upward positive (c) Downward positive and (d) Upward negative. From *Berger [1978]*.

atoms and molecules. As the electrons over-run the lower positive charge region, they neutralize a fraction of its positive charge and continue to travel towards the ground. The charge movement from the cloud to the ground occurs via a propagating electrical discharge mechanism called "stepped leader" (see Figure 1.3). Stepped leaders move downward in discrete luminous segments of tens of meters with timescales of tens of microseconds between luminous steps. Each negative leader step produces a pulse of visible light, a pulse of radio-frequency energy, and a pulse of X-rays, primarily in the 200 keV range. With an average speed of 2×10^5 m/s, stepped leader can travel from cloud to the ground in about 20 ms *[Nagai et al., 1982]*, where it meets the induced positive charge on the Earth surface and determines the lightning strike path. This is called the attachment process and is immediately followed by the first return stroke which is a bright channel of high temperature air with a maximum temperature near 30,000°C. The return stroke heats up the channel, expands the air spontaneously and produces the thunder which is a sound wave originating as an outward propagating shock wave from the expanding return stroke channel. After the first return stroke, if additional negative charge still exists at the upper part of previous stroke channel, a continuous propagating leader, called "dart leader", moves downward with a speed of about 10^7 m/s and deposit somewhat less charge along their path compared to stepped leaders. The dart leaders set the stage for subsequent return strokes, where about 80% of flashes that lower negative charge have more than one stroke, usually three to five. There are other types of leaders as well, such as "Dart-stepped leaders" and "chaotic dart leaders", which might occurs following the subsequent return strokes *[Rakov and Uman, 2003; Dwyer and Uman, 2014]*.

In the case of upward lightning, the leader propagates towards the cloud without producing any observable return stroke. However, it provides a connection between cloud and ground which allows dart leaders to move downward and produce subsequent return stokes. This is very similar to the case of rocket-triggered lightning, where lightning is artificially being initiated from natural thunderstorms via the rocket-and-wire technique. In this technique, the rocket carries the trailing wire to several hundreds of meters altitude in a few seconds, and then electrical breakdown occurs at the top of wire. The enhancement of ambient electric field between top of the wire and negative

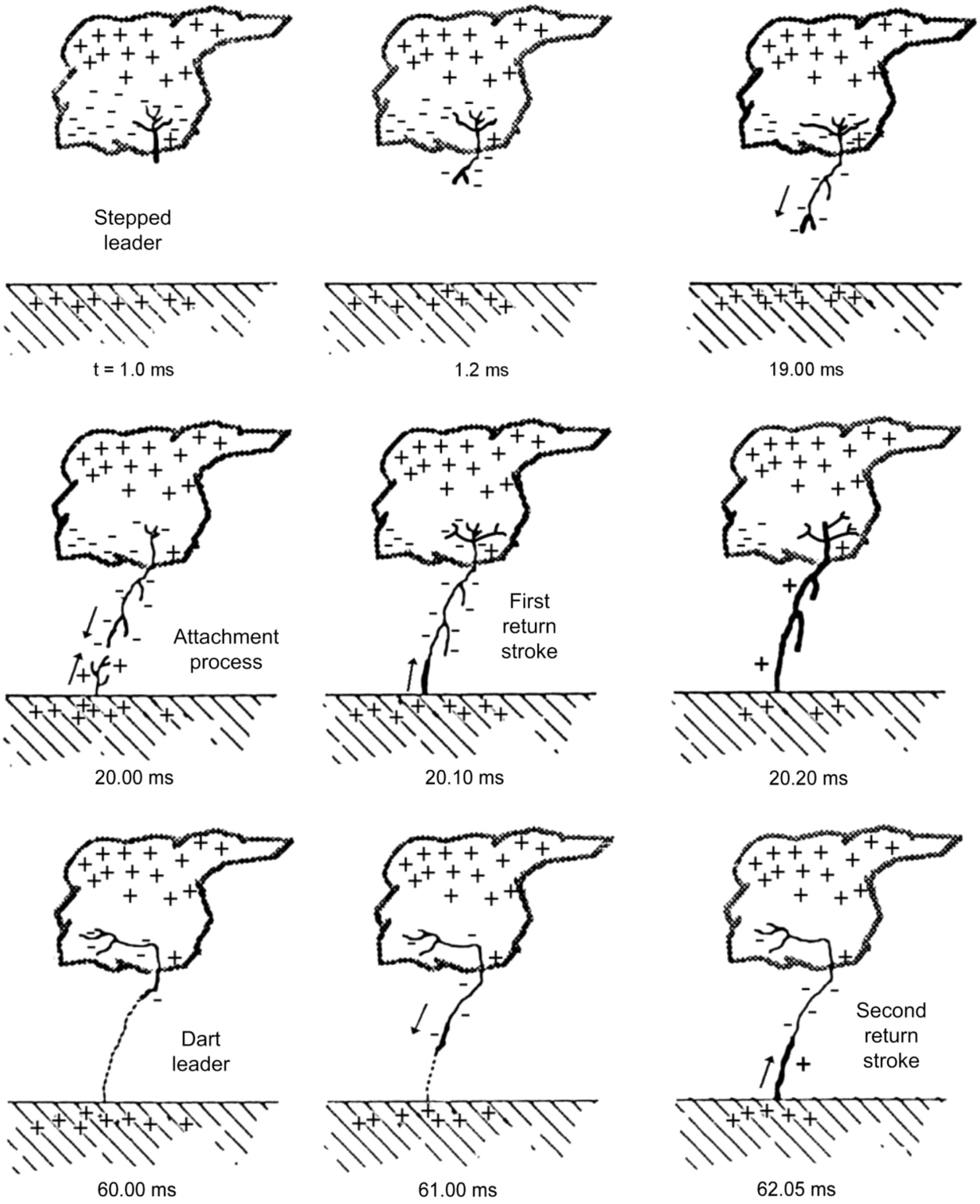

Figure 1.3: A schematic of the development of a negative cloud-to-ground (CG) lightning flash. From *Uman [2001]*.

cloud overhead will initiate a positively-charged leader (UPL) which then transforms to hundreds of amperes continuous current for tenth of a second and melts the wire. While the continuous current flows, a negative dart leader may propagate downward from the cloud to the ground which would be followed by subsequent return strokes. Every summer at the International Center for Lightning Research and Testing (ICLRT) located at north-central Florida, about 20-30 lightning flashes would be triggered via the same technique.

1.2 High-Energy Atmospheric Physics Theory

Until the beginning of 21^{st} century, lightning as a natural phenomenon was being studied under classical electrodynamics physics, however with the discovery of high-energy radiations associated with thunderstorm activities, such as Terrestrial Gamma-ray Flashes (TGFs) (short and bright burst of gamma rays), X-rays, gamma-ray glows, etc., there have been enormous efforts over the last decade to study these types of radiations in our atmosphere. The field of high-energy atmospheric physics started with the paper published in 1925 by C.T.R. Wilson, the winner of Noble prize in 1927 for the invention of cloud chamber, in which he proposed that a portion of energetic electrons and gamma radiations in our atmosphere might be produced by the electric fields of thunderclouds. Nowadays, it is known that lightning produces X-rays and gamma rays with energies that extend to tens of MeV, but the exact mechanism for their production and propagation is not well understood. It has been suggested that runaway electrons (electrons accelerated in the electric field of thunderclouds) interact with air atoms through bremsstrahlung scattering and produce X-rays and gamma ray. In the following, I will go over the theory of runaway electrons and the mechanism that can explain the production of energetic radiations in our atmosphere.

1.2.1 Wilson Runaway Electrons

When electrons are moving inside an electric field of thunderclouds, they gain energy from the ambient field and lose energy via ionization and atomic excitations (at energies less than tens of MeV) and bremsstrahlung emission (at energies above tens of MeV). If the rate of energy gain

exceeds the rate of energy loss in the medium, electrons accelerate to very high energies and run away. The amount of energy they gain depends on how large the electric field is. The magnitude of break-even field, which is the electric field that is required for electrons to run away, is about E_b = 2.05×10^5 V/m×N. N is the relative density of the air with respect to that sea level in the International Standard Atmosphere (ISA) system. By including the effect of elastic scattering, it has been shown by simulations that the minimum electric field required to produce runaway electrons is about 30% higher than E_b which is called runaway threshold field and it is equal to E_{th} = 2.67×10^5 V/m×N *[Dwyer, 2003]*. This value is comparable to the electric fields measured inside the clouds using balloon soundings which suggests a possible connection between the production of runaway electrons and initiation of lightning *[Marshall et al., 1995; Rakov and Uman, 2003]*. Elastic scattering makes the electrons travel a farther distance compared to a straight line by scattering them off the field lines which results to a larger energy loss. The energy loss per unit length for an electron (positron) in air versus its kinetic energy is plotted is Figure 1.4. The horizontal line and dashed line represent the electric force from a 5×10^6 V/m electric field and break-even field (E_b), respectively. Runaway electrons are being produced whenever the initial kinetic energy of electrons would be greater than the runaway threshold energy (ε_{th}). Such energetic seeds could be provided from cosmic rays or radioactive decays.

1.2.2 Cold (Thermal) Runaway Electron

The runaway threshold energy depends on the applied electric field and drops very quickly with increasing the electric field, in such a way that for electric fields above the critical field, $E_c \approx$ 3×10^7 V/m, all free electrons in the medium including low energy ones will run away. This is equivalent of placing the solid horizontal line in Figure 1.4 above the curved line and is called Cold or thermal Runaway Electron (CRE) mechanism. The critical field value is about ten times greater than conventional breakdown field (E_k = 3×10^6 V/m at sea level) and does not exist for a long period of time, since it would be discharged very quickly by the conventional breakdown *[Babich, 2003]*. However, it has been suggested that such high electric fields could form locally on

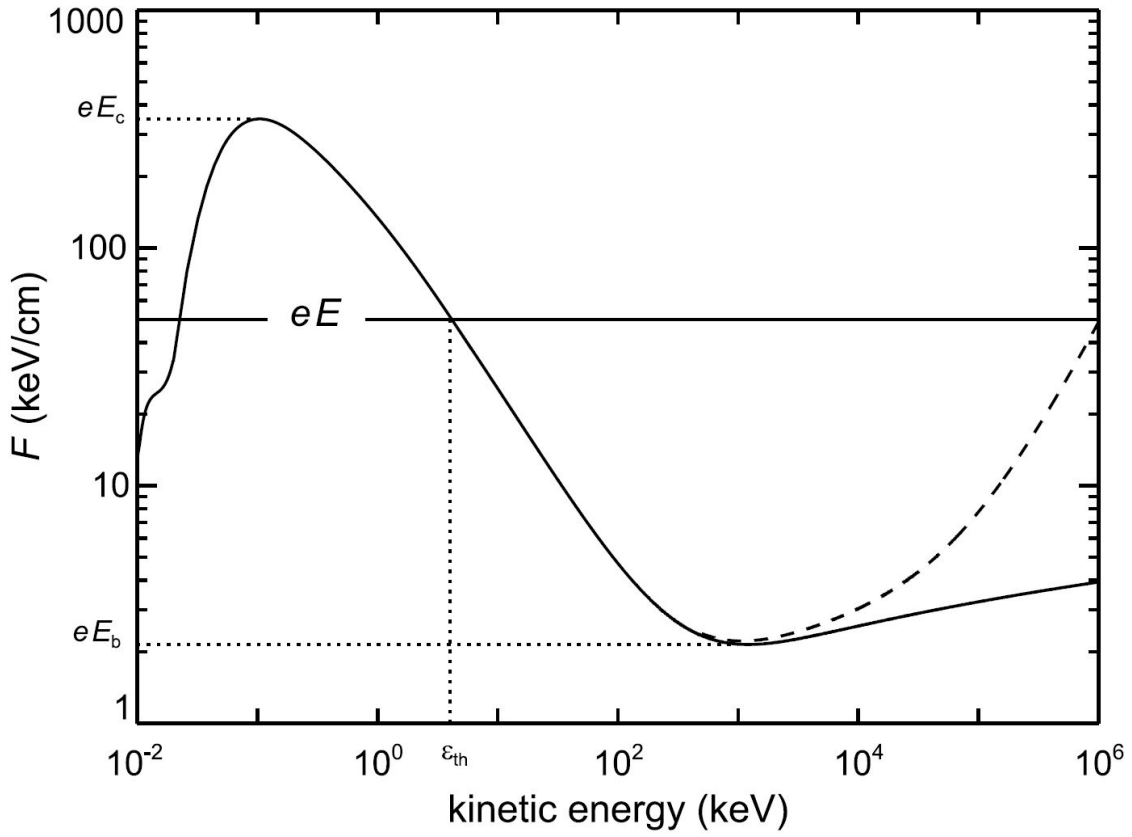

Figure 1.4: The effective frictional force experienced by an electron (positron) moving in the air versus its kinetic energy. The horizontal line shows the force from an electric field of 5×10^6 V/m. E_c and E_b are the critical and break-even fields. Electrons (positrons) with initial energy greater than ε_{th} run away. From *Dwyer [2004]*.

the tip of streamers and leader to provide seed electrons via thermal runaway *[Moss et al., 2006; Oreshkin et al., 2012]*. During the CRE regime, the total number of runaway electrons which are produced internally increases exponentially for a very short time period *[Babich, 2003]*. Ground-based spectroscopy of X-rays from rocket-triggered lightning have shown a power-law dependence of energy spectrum for these energetic particles with no predictable characteristic energy which depends on many parameters including the geometry and amplitude of electric field at the tip of leader *[Arabshahi et al., 2014]*. CRE mechanism neither requires a large-scale electric field that extends several hundreds of meters, nor external seeds of energetic electrons and could be the dominant means of generating X-rays from lightning leaders and laboratory sparks *[Dwyer and Uman, 2014]*.

1.2.3 Relativistic Runaway Electron Avalanches (RREAs)

In 1992, by including the elastic scattering of runaway electrons with atomic electrons in the air (Møller scattering), *Gurevich et al. [1992]* predicted that additional energetic seed electrons could be produced inside thunderclouds. This process which resulted in an avalanche multiplication of energetic particles is called Relativistic Runaway Electron Avalanche (RREA) mechanism *[Babich et al., 1998]*. In his original idea, Wilson does not seem to have performed any kind of mathematical description of avalanche properties, however he does refer to the collective behavior of electrons as "snowball effect" *[Williams, 2010]*. RREA requires a significantly smaller electric field compared to CRE mechanism, where runaway electron avalanche threshold electric field is shown to be about E_{th} = 2.67$\times 10^5$ V/m$\times$N *[Dwyer, 2003; Babich et al., 2004]*. However, energetic seeds of electrons, which could be provided from cosmic rays or radioactive decays, are necessary to initiate the avalanche. If the runaway electrons were travelling along the electric field lines without being scattered by atomic electrons, the magnitude of E_{th} would have been much closer to break-even field (E_b). In the RREA mechanism, a cosmic ray collides with an air molecule or atom and knocks out free electrons. If the electric field is above the E_{th}, free electrons will run away, ionize the air and produce more seed electrons. For initial seeds of electrons with energies above the ε_{th} (F_0), the total flux of runaway electrons (F_{RREA}) at the end of avalanche region increases exponentially given by Equation 1.1.

$$F_{RREA} = F_0 exp(\xi),\ where\ \xi = \int_0^L \frac{dz}{\lambda} \tag{1.1}$$

Here, λ is the avalanche e-folding length, and ξ is the number of e-folding length which is equal to L/λ for a uniform electric field. *Dwyer [2003]* performed an accurate Monte Carlo simulation to find the dependency of the avalanche length on the applied electric field when 300 kV/m $\leq E \leq$ 2500 kV/m, which is given by Equation 1.2.

$$\lambda = \frac{7.3\ MeV}{(eE - F_d)} \tag{1.2}$$

Here F_d = 0.260 MeV/m$\times$N is the average energy loss rate experienced by the minimum ionizing electrons along the avalanche direction *Coleman and Dwyer [2006]* and N is the density of the air relative to that at sea level.

The energy spectrum of runaway electrons reaches a steady state after a few avalanche lengths, so the total number of runaway electrons per unit energy can be approximated as $f_{re}(\varepsilon) \times exp(t/\tau)$, where τ is the avalanche e-folding time. The average kinetic energy gained by a runaway electron that moves a distance of z is equal to $\varepsilon = z(eE - F_d)$. Similar to Equation 1.1, we can write the number of runaway electrons travelling between z and $z + dz$ as $N_0 \times exp((L - z)/\lambda)dz/\lambda$. By substituting the Equation 1.2 and changing the variable from z to ε, the energy spectrum of the runaway electrons can be written as following given by Equation 1.3.

$$f_{re} = \frac{F_{RREA}}{7.3\ MeV} \times exp(\frac{-\varepsilon}{7.3\ MeV}) \tag{1.3}$$

This equation is valid for electrons with kinetic energies of hundreds of keV to several tens of MeV and the exponential behavior is almost independent of energy and flux of initial seed electrons. The average energy of runaway electrons is about 7.3 MeV which is also roughly independent of the background electric field for the fields well above E_{th}.

1.2.4 Relativistic Feedback Mechanism

Dwyer [2003] proposed a new mechanism for the production of runaway electrons by taking into account the positive feedback from energetic photons and positrons. In this mechanism shown in Figure 1.5, runaway electrons emit X-rays via bremsstrahlung interaction which can either Compton backscatter or pair-produce. The backscattered photons can initiate a secondary avalanche by propagating to the beginning of primary avalanche region and producing additional runaway electrons via either Compton scattering or photoelectric absorption *[Babich et al., 2007]*. This is called the X-ray feedback mechanism. In addition, the positrons generated via pair-production can accelerate and propagate along the electric field lines and in the opposite direction of runaway electrons. Given that the cross section of positron annihilation decreases

with the energy and positrons can accelerate to tens of MeV, they can travel distances on order of kilometer before being annihilated *[Dwyer et al., 2012]*. By reaching the beginning of primary avalanche region, positrons can produce additional runaway electrons via Bhabha scattering (hard elastic scattering with atomic electrons in the air) which can lead to the initiation a secondary avalanche as well. This is called positron feedback mechanism. X-ray feedback requires a shorter avalanche length to develop compared to positron feedback because of shorter attenuation length, however it is the dominant process at large electric fields (e.g., E > 750 kV/m×N) with positron feedback being more important at lower field strengths.

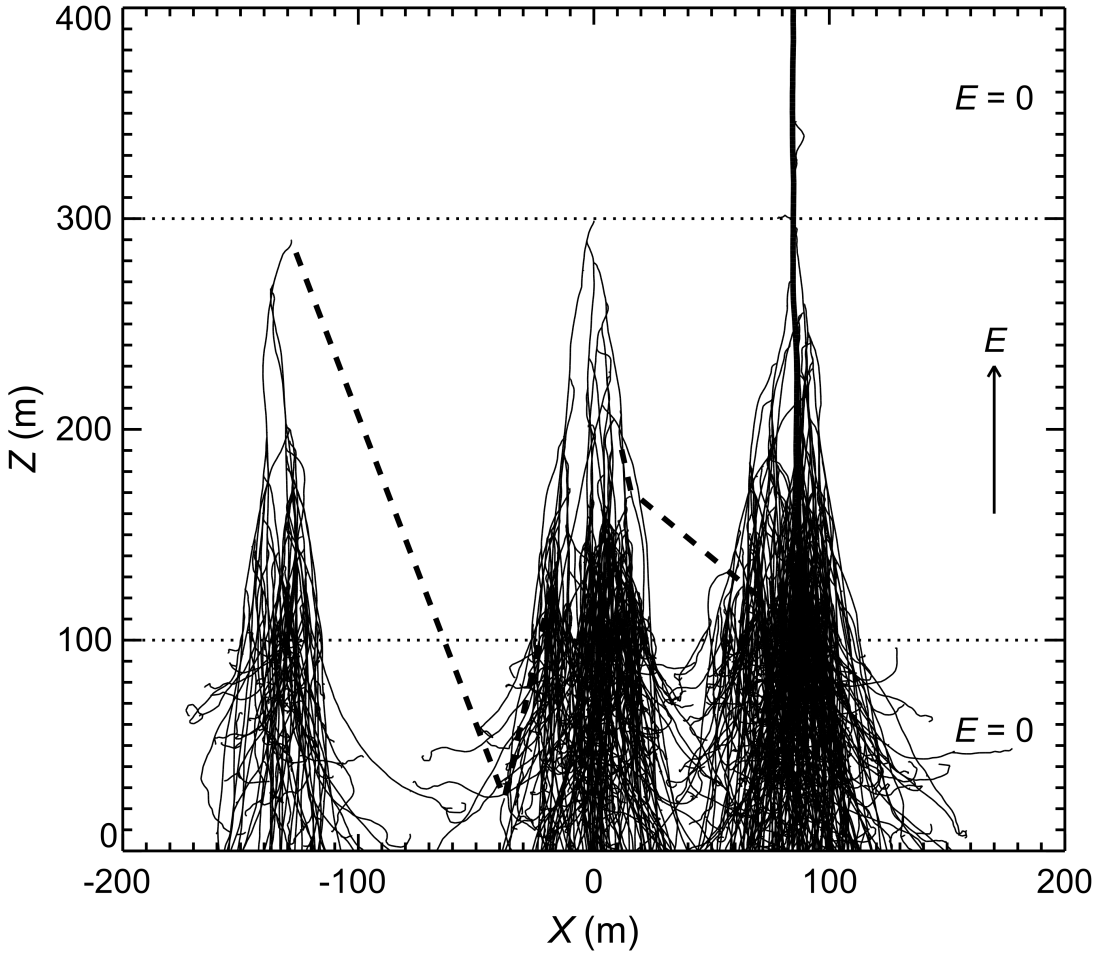

Figure 1.5: The illustration of relativistic feedback mechanism from REAM Monte Carlo simulation. The solid lines are runaway electrons, the dashed lines are backscattered X-rays and thick dark line is the positrons. The middle avalanche is the primary avalanche, the one on the right and left represent the positron and X-ray feedback respectively. From *Dwyer [2003]*.

Dwyer [2007] has reported the detailed calculation of runaway electrons produced from the relativistic feedback mechanism. F_{RF}, the flux of runaway electrons at time t, is the sum of all feedback avalanches up until that time which could be written in form of Equation 1.4.

$$F_{RF} = \Sigma_{n=0}^{t/\tau} F_n(t) \tag{1.4}$$

τ or the feedback time, is the time required for electrons or backward propagating positrons and X-rays to complete one round trip inside the avalanche region and $F_n(t)$ is the flux of $(n+1)^{th}$ generation of runaway electrons given by Equation 1.5.

$$F_{n+1} = \gamma \int_0^t D(t-t')F_n(t')dt' \tag{1.5}$$

where $D(t-t')$ is the normalized distribution of the next generation of particles entering the midplane and is assumed to be equal to the Dirac delta function, $\delta(t-\tau-t')$, for simplicity; γ is the feedback factor which is the number of $(N+1)^{th}$ generation of runaway electrons passing through the midplane from divided by the number of N^{th} generation of runaway electrons passing through the midplane, and F_0 is the flux of primary avalanche from RREA mechanism. Equation 1.5 can be approximated as:

$$F_n = \gamma^n S_0 exp(\xi)\theta(t-n\tau) \tag{1.6}$$

With θ as the step function. By plugging F_n from Equation 1.6 into Equation 1.4, we have:

$$F_{RF} = S_0 exp(\xi)\Sigma_{n=0}^{t/\tau}\gamma^n \tag{1.7}$$

In the case of $t \gg \tau$, the flux of runaway electrons from relativistic feedback is given by Equation 1.8, where $\tau' = \tau/ln(\gamma)$ is the e-folding time to increase the flux of runaway electrons due to feedback (if γ > 1).

$$F_{RF} = \begin{cases} S_0 exp(\xi) exp(t/\tau')/(\gamma - 1), & \gamma > 1 \\ S_0 (t/\tau) exp(\xi), & \gamma = 1 \\ S_0 exp(\xi)/(1 - \gamma), & \gamma < 1. \end{cases} \tag{1.8}$$

The feedback factor γ represents the fractional increase or decrease in the number of runaway electrons during each feedback time. When γ < 1, the number of runaway electrons is being enhanced by a factor of $(1 - \gamma)^{-1}$, where this enhancement factor is increasing significantly when γ approaches to 1 and makes the relativistic feedback mechanism dominate the seeds from external sources. The discharge currents produced by these runaway electrons may temporarily balance the charging currents and create an approximately steady-state electric field inside the thundercloud. This scenario could explain the long-lasting gamma-ray glows which will be discussed later. This scenario could explain the long-lasting gamma-ray glows which will be discussed later.

If the electric field grows rapidly enough, γ could go above 1 before the discharge currents would respond. This case could happen by large scale charging of thunderclouds, charge motion during lightning or currents from RREA mechanism *[Dwyer, 2005]* and makes the relativistic feedback the dominant mechanism for the production of seed electrons momentarily. In such a case, the number of runaway electrons from feedback mechanism is given by Equation 1.9, where the discharge becomes self-sustaining and increases exponentially with time.

$$F_{RF} = F_{RREA} exp(t/\tau')/(\gamma - 1) \tag{1.9}$$

Given that the number of X-rays is proportional to the number of seed electrons, similar equation could be used to describe the flux of X-rays and gamma rays. In fact, the relativistic feedback can explain the large fluxes of gamma rays and short time-scale of TGFs *[Dwyer, 2008]*. The feedback process continues until the background electric field collapses due to the large amount of ionization from runaway electrons.

1.3 High-Energy Radiation from Thunderstorms

1.3.1 Terrestrial Gamma-ray Flashes (TGFs)

Terrestrial Gamma-ray Flashes (TGFs) were first discovered in 1994 by the Large Area Detectors (LAD) instrument of the Burst and Transient Source Experiment (BATSE) onboard the Compton Gamma-Ray Observatory (CGRO) *[Fishman et al., 1994]*. BATSE was intended to search for cosmic Gamma-Ray Bursts (GRBs), but it also detected intense flashes of gamma rays originating from the Earth's atmosphere. Figure 1.6 shows the measured number of counts per 100 μs bins for twelve of these TGF events. Since then, four other major space missions have been launched to observe TGFs including the Reuven Ramaty High Energy Solar Spectroscopic

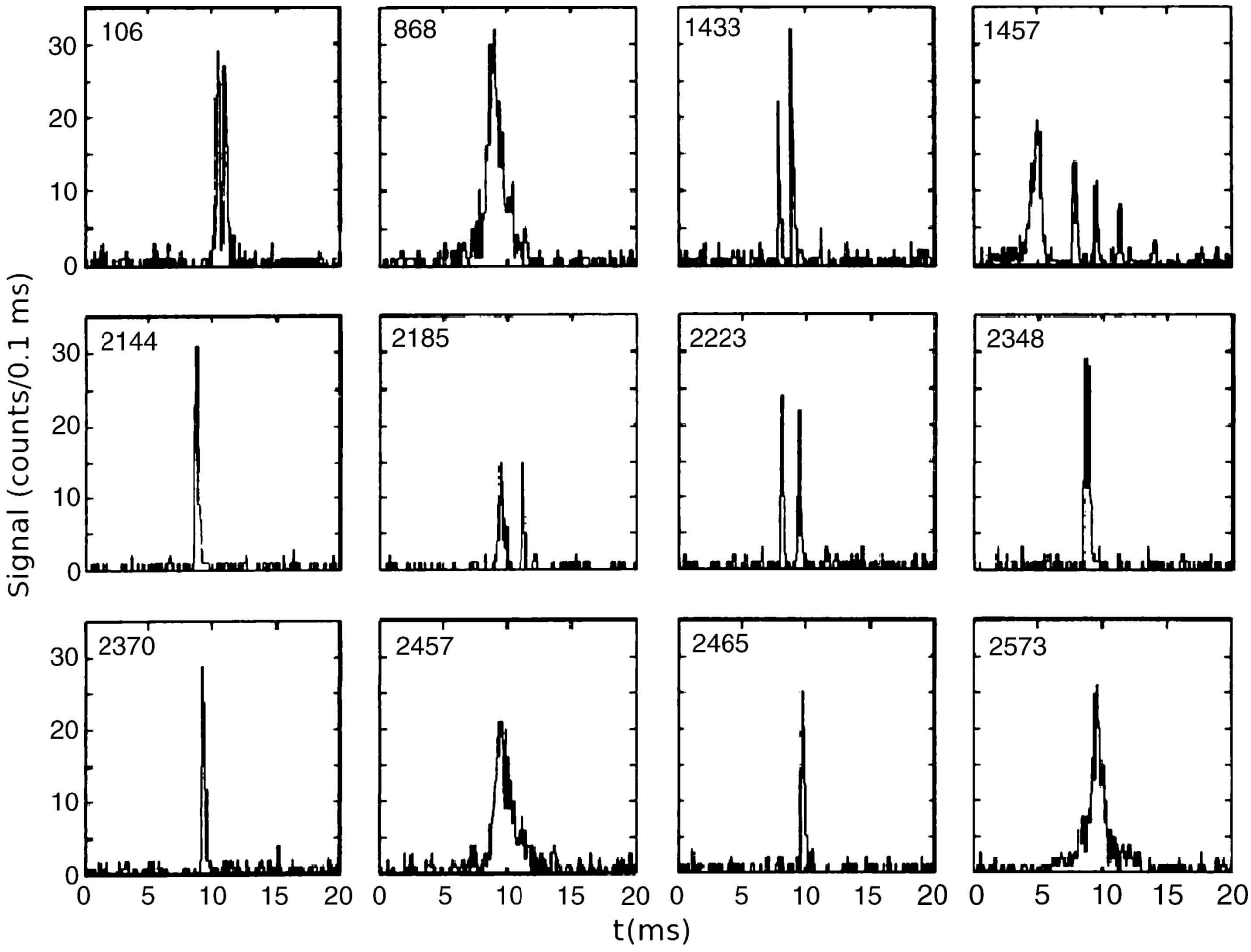

Figure 1.6: The time profile of twelve Terrestrial Gamma-ray Flash events observed by BATSE. The time resolution of plot is 100 μs per bin. From *Fishman et al. [1994]*.

Imager (RHESSI) *[Smith et al., 2005]*, the Astrorivelatore Gamma a Immagini Leggero (AGILE) *[Marisaldi et al., 2010; Tavani et al., 2011]*, the Gamma-ray Burst Monitor (GBM) onboard Fermi Gamma-ray Space Telescope *[Briggs et al., 2010; Connaughton et al., 2010]*, and The Modular X- and Gamma-ray Sensor (MXGS) onboard Atmosphere-Space Interactions Monitor (ASIM) *[Neubert et al., 2019; Ostgaard et al., 2019]*.

Although it was known that TGFs detected from low-Earth orbit had originated from the atmosphere below, the source altitude of TGFs remained uncertain for many years. For over a decade, it was assumed that TGFs were associated with sprites, high altitude discharges that had been discovered a few years earlier. However, in 2003 a TGF was measured on the ground in association with rocket-triggered lightning *[Dwyer, 2003]*. This event had a similar duration and energy spectrum to TGFs recorded in space. *Dwyer [2004]* suggested that similar upward directed thundercloud events could explain TGFs. *Dwyer and Smith [2005]* compared the energy spectrum of TGFs detected by the RHESSI up to 20 MeV and Monte Carlo simulation of RREAs at E = 400 kV/m$\times$N and four different atmospheric depths which is plotted in Figure 1.7. The spectra from source altitude below 21 km had the closest fit to the RHESSI measured spectrum which revealed that the source altitude of TGFs should be between 15 to 21 km and ruled out the idea of TGF's association with sprites. By measuring the VLF radio emissions during 26 RHESSI TGFs, *Cummer et al. [2005]* found that 50% of the TGFs occurred within several milliseconds of detectable positive polarity, and charge moment was too small to be considered as the source of RREA related processes. *Cummer et al. [2015]* used radio emission (sferics) measurements associated with TGFs and found the source of TGFs to be about 12.5 km. Since then, it has been established that most TGFs are produced inside thunderclouds and are associated with the early stages of positive intra-cloud lightning *[Stanley et al., 2006; Shao et al., 2010; Dwyer et al., 2012]*

The data of LAD instrument onboard BATSE was suffering from significant dead-time due to large number of photons for each TGF event, and those events were actually much brighter than previously reported *[Grefenstette et al., 2008]*. The dead-time is the required time for the detector to recover from last event, while during which is not capable of recording another event. Dead-

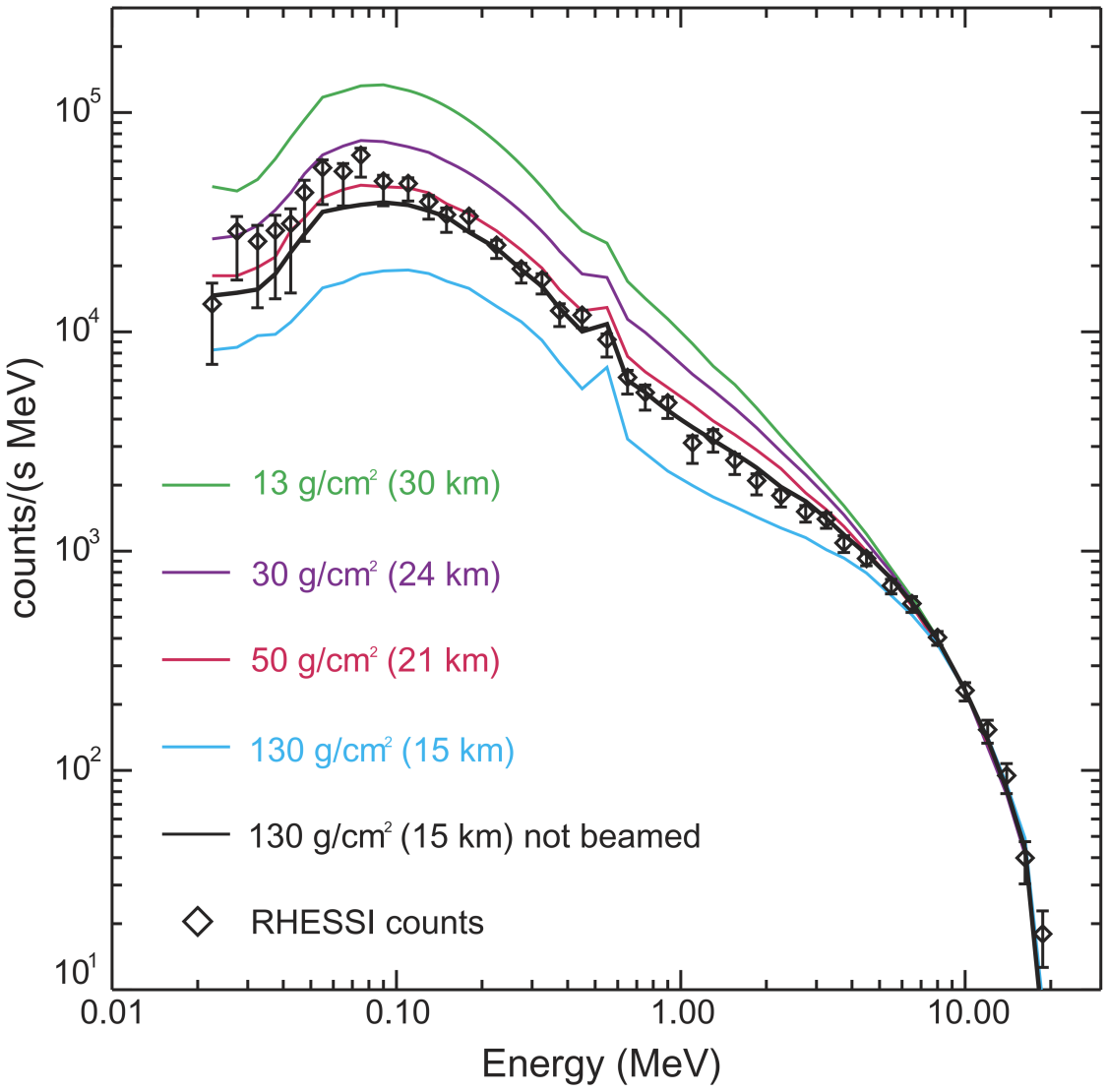

Figure 1.7: The energy spectrum of TGFs observed by RHESSI compared to the Monte Carlo simulation of runaway breakdown at four different atmospheric depths. Note that the source altitude of 21 km had closest correlation with RHESSI data. From *Dwyer and Smith [2005]*.

time effect along with the pulse pile-up (happens when pulses arrives closer in time than the pulse resolution time for the detector) and Compton scattering were increasing the duration of TGFs on BATSE which was also softening the energy spectrum of TGFs. *Fishman et al. [2011]* studied the temporal distribution of TGFs using the Gamma-ray Burst Monitor (GBM) onboard Fermi and reported a pulse duration of 50 μs to 700 μs with a median of 100 μs.

Since the discovery of TGFs, several theoretical models have tried to explain the production of TGFs including significant charge transfers associated with positive CG lightning discharges and subsequent large electric fields *[Lehtinen et al., 1999]* and electromagnetic pulses *[Pasko et al., 1998]*. However, there are currently two widely accepted models (Relativistic Feedback and Lightning Leaders) suggested to explain the mechanism of TGFs production. Relativistic Feedback, as explained in Section 1.2.4, is based on the production of energetic positrons and backscattered X-rays and is capable of explaining the observed pulse structure, time-intensity profile, fluence and beam distribution of gamma rays. The second model is based the formation of streamer from hydrometers and very high electric fields at the tip of leader *[Gurevich, 1961; Moss et al., 2006; Dwyer, 2008]* which can potentially produce of a large number of runaway electrons on a timescale of tens of nanoseconds *[Celestin and Pasko, 2012]*.

1.3.2 Gamma-Ray Glows

Gamma-ray glows from thunderstorms are emissions of gamma rays usually lasting from seconds to minutes *[Dwyer et al., 2012]*. They were initially observed over 30 years ago using aircraft *[Parks et al., 1981; McCarthy and Parks, 1985]* and have since been measured using balloons, aircraft and from the ground. Gamma-ray glows were the first confirmation that runaway electrons are generated by thunderstorm electric fields, a mechanism originally proposed by C. T. R. Wilson in 1925 *[Wilson, 1925]*. Using a NASA F-106 jet carrying NaI scintillators, *Parks et al. [1981]* and *McCarthy and Parks [1985]* demonstrated that active thunderstorms produce gamma rays that lasted tens of seconds with energies greater than 110 keV. They found that the gamma-ray emissions were generally terminated, rather than caused, by lightning. Figure 1.8 shows both the gradual nature of the glows while they are active and their sudden termination due to lightning.

In a series of pioneering balloon flights, *Eack et al. [1996*a,b*, 2000]* flew scintillators and electric field sensors through and above active thunderstorms, measuring gamma-ray glows. Because of the mass limitations of balloon payloads, thin scintillators were flown, allowing energies up to only 120 keV to be measured. In one sounding, they found that the gamma-ray emissions occurred

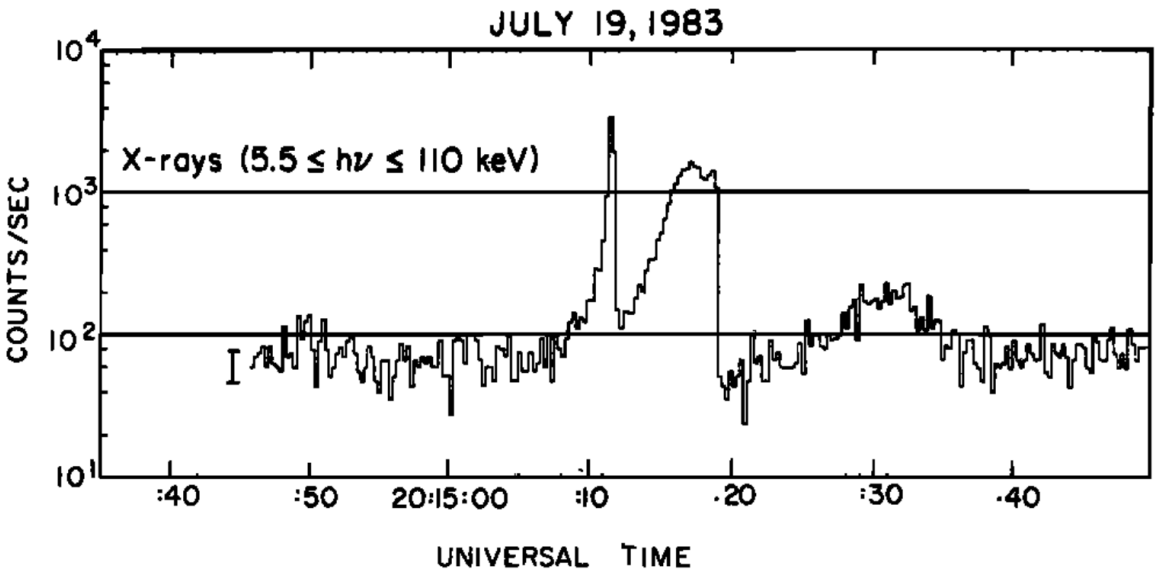

Figure 1.8: Three X-ray emissions detected by the NaI scintillators onboard a NASA F-106 jet in 1983. The first two enhancements are suddenly terminated by a nearby lightning flash; however the third event ends gradually possibly due to plane leaving the enhancement region. From *McCarthy and Parks [1985].*

at an altitude of 4 km where the electric field was highest. The emission persisted while the balloon passed through the strong electric field region within the storm, except that it terminated and then restarted following two lightning flashes (see Figure 1.9). Other balloon soundings recorded similar high gamma-ray fluxes in an anvil at 14 km and above the thundercloud at 15 km altitude.

More recently, in 2009, the Airborne Detector for Energetic Lightning Emissions (ADELE) flew on the NSF/NCAR Gulfstream V jet over and next to thunderstorm cells in Florida *[Smith et al., 2011*a,b*].* ADELE, which included several plastic and NaI scintillators, observed 12 separate gamma-ray glows that lasted tens of seconds to more than a minute during passes over or near the tops of active thunderstorms *Dwyer et al. [2012].* Figure 1.10 shows two gamma-ray glows seen by ADELE. It is possible that the durations of the gamma-ray glows were limited by the time that the aircraft was near the thunderstorms, and so the gamma-ray glows might have lasted longer than observed. On one flight, the aircraft inadvertently penetrated a thunderstorm and directly entered the runaway electron source region of a very bright glow in addition to recording two intervals with enhanced 511 keV (positron annihilation line) emissions *[Dwyer et al., 2015].* It seems reasonable

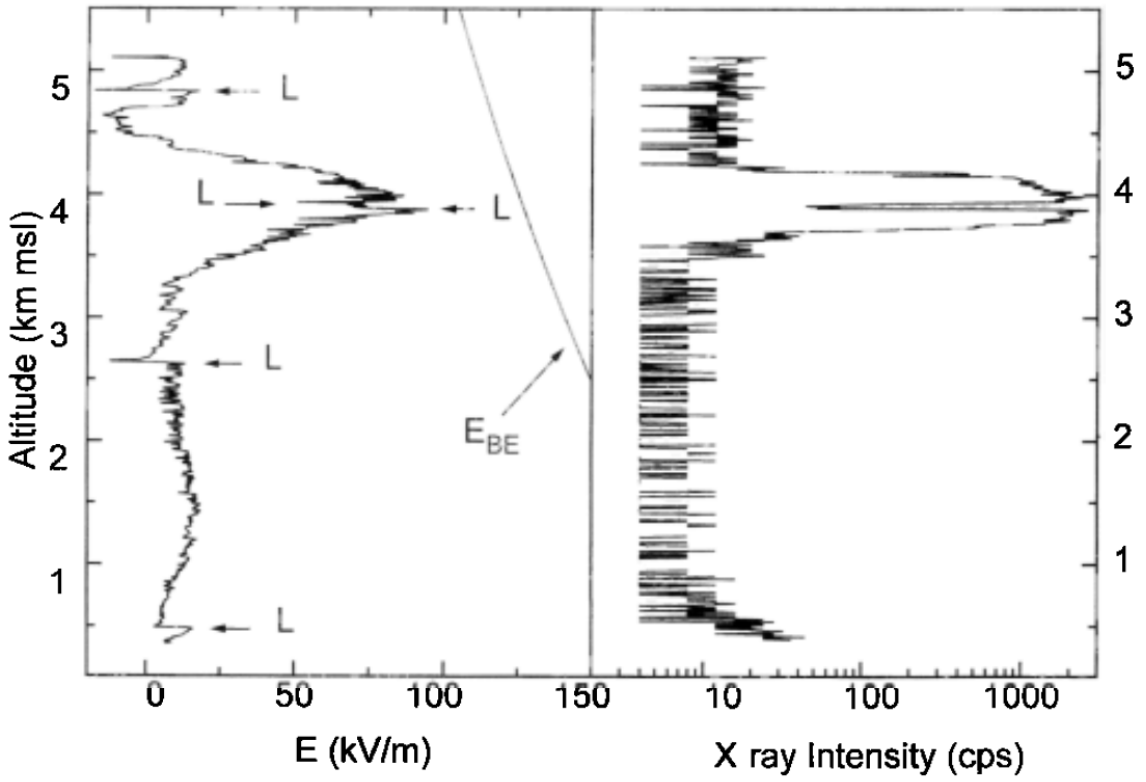

Figure 1.9: Electric field measurement (left) and count rate of X-rays with energies between 30 to 120 keV (right) during a balloon sounding through a mesoscale convective system (MCS). In the left panel, electric field transients due to lightning are marked with "L" and breakeven field strength (E_{BE}) are also plotted. From *Eack et al. [1996*a*]*.

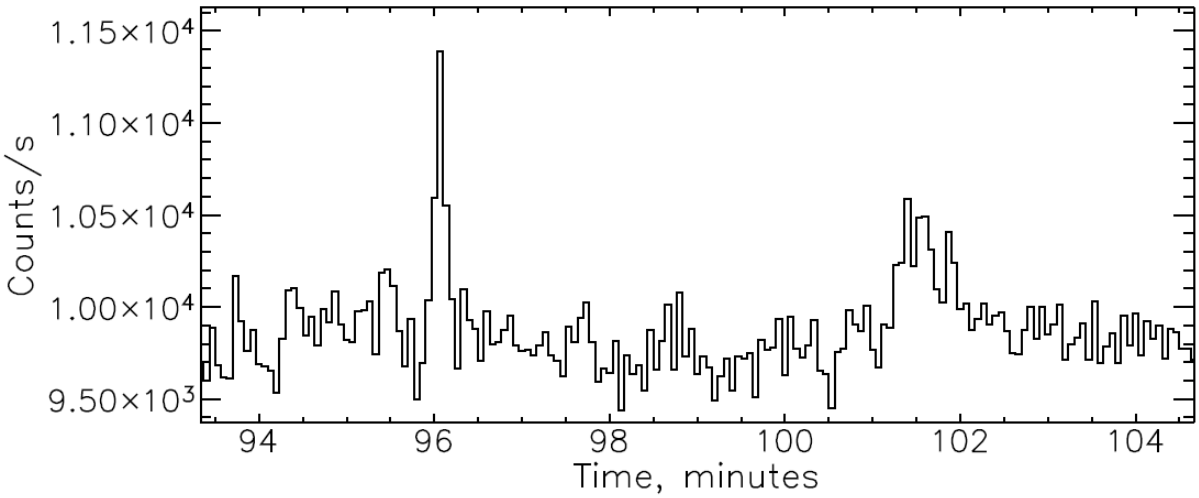

Figure 1.10: Gamma-ray count rate for two glows observed by the ADELE instrument flying above two different active cells. The longer duration of the second event implies a greater spatial extent of the source. From *Dwyer et al. [2012]*.

that gamma-ray glows are produced by RREA emissions when the thunderstorms are in a highly charged state between lightning flashes. Given that the discharge currents from ionization of the air by runaway electrons might be significant, the gamma-ray glows might occur during a steady state when the charging of thunderstorm is temporarily balanced by the runaway electron emission *[Dwyer and Uman, 2014]*.

Gamma-ray glows have also been recorded on high mountains *[Alexeenko et al., 2002; Brunetti et al., 2000; Chilingarian et al., 2012; Chubenko et al., 2000; Torii et al., 2009; Tsuchiya et al., 2009]* and in regions of Japan from thunderclouds with low charge centers *[Torii et al., 2011; Tsuchiya et al., 2011]*. For example, *Chilingarian et al. [2010]* reported that energetic particle count rates at Mount Aragats more than doubled when a thundercloud was 100-200 m above the detector, and *Torii et al. [2002]* measured gamma-ray enhancements up to 70 times the local background level at the Monju nuclear reactor in Japan during a winter thunderstorm. A review of earlier observations may also be found in *Suszcynsky et al. [1996]*. From these previous observations, it is apparent that gamma-ray glows are frequently produced by thunderstorms and are readily measured whenever instruments are placed near the thunderclouds. However, exactly how common they are and where and when they are produced remain to be determined.

1.3.3 X-Ray Emissions from Lightning

Detection of energetic emissions associated with the stepped leader phase of natural CG lightning were first reported in 2001 on the mountains of New Mexico *[Moore et al., 2001]* and confirmed later during rocket-triggered lightning events in 2002, where discrete energetic bursts were detected during the dart leader and dart-stepped leader phases *[Dwyer, 2003]*. Figure 1.11 shows an example of X-ray observations from rocket-triggered lightning along with the response of the NaI(Tl)/photomultiplier tube (PMT) detector to the 662 keV gamma-ray photons from Cs-137 radioactive source. The X-rays were observed to be emitted before return stroke with duration less than 1 μs and energies extending up to 250 keV. *Dwyer [2004]* showed that X-ray emissions orig-

inated from the bottom of the leader channel and the source propagated downward with the leader as it was approaching the ground.

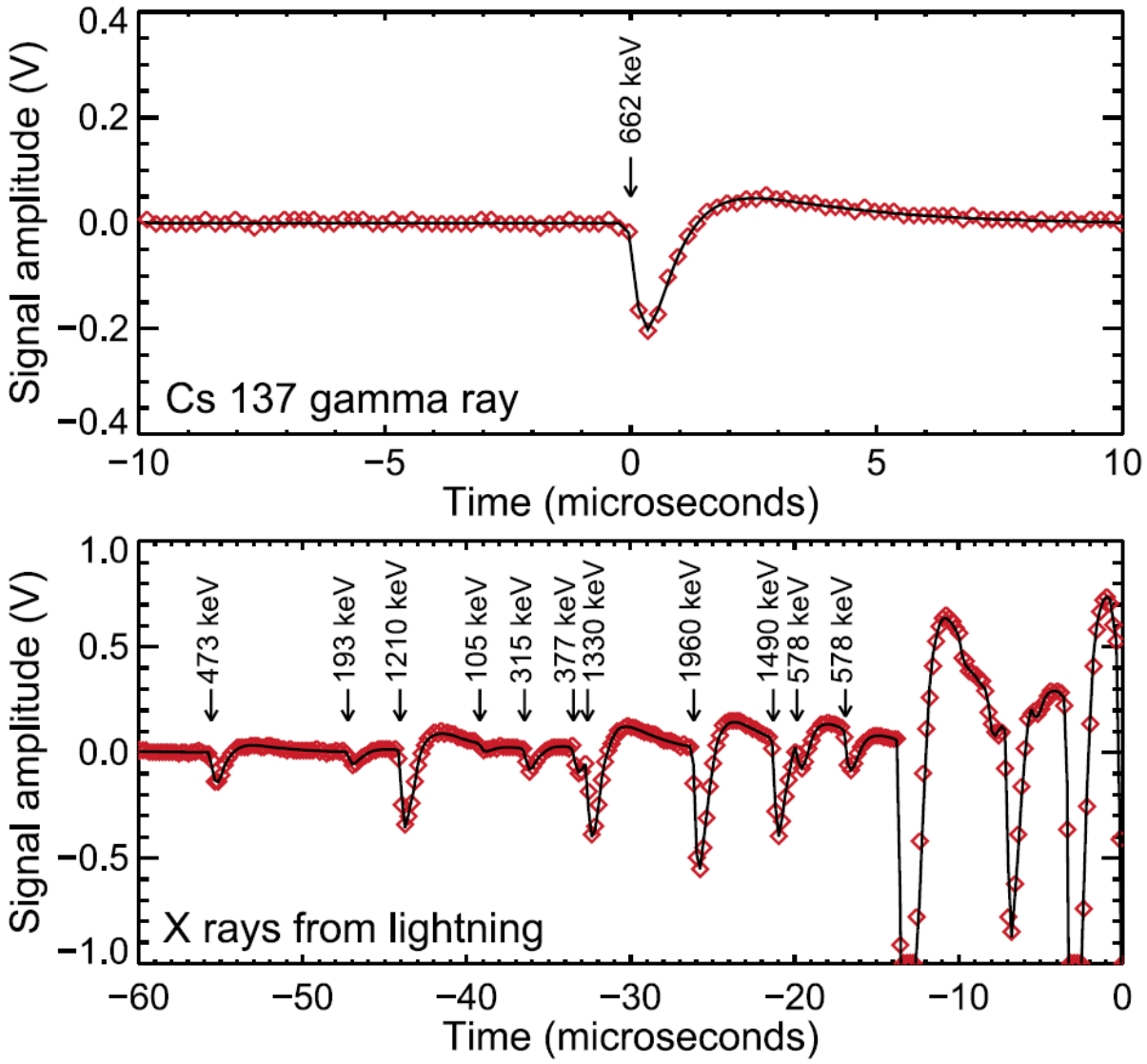

Figure 1.11: The response of NaI(Tl)/PMT detector to the 662 keV from Cs-137 radioactive source (top) and waveform for 60 ms prior to a return stroke during the rocket-triggered lightning (bottom). The arrows show the time and deposited energy of X-rays. From *Dwyer [2004]*.

Since the energy spectra and fluence of these X-rays were not consistent with the RREA mechanism, the Cold (thermal) Runaway Electron (CRE) mechanism was suggested to be responsible for their production. Later, modeling confirmed that propagating streamers can produce significant fluxes of thermal runaway electrons *[Moss et al., 2006]*. As explained in Section 1.2.2, CRE does

not require an external energetic seed of particles or a large-scale electric field, but it does require localized electric fields about 10 times the conventional breakdown field in air. Subsequent observations of rocket-triggered lightning with the Thunderstorm Energetic Radiation Array (TERA) at ICLRT provided information about the X-ray luminosity (about 10^{16} electrons/s near the ground), where emissions of X-rays occurred during dart-stepped leader phase of return stroke and were detected out to 500 m from the lightning channel *[Saleh et al., 2009].* REAM simulation showed that the energetic electrons that emit such X-rays isotopically from the leader have characteristic energies up to about 1 MeV. Later, *Schaal et al. [2012]* investigated the angular and energy distribution of X-ray emissions from both natural and rocket-triggered lightning, where they found that electron luminosity increased exponentially with return stroke current up to about 10 kA with a maximum of 10^{17} electrons/s. *Arabshahi et al. [2014]* performed ground-based high-energy spectroscopy of emission from lightning leader and found that energy spectra has a power law dependence on energy of the photons with a power index, λ, between 2.5 and 3.5 and had no characteristic energy. In addition, *Dwyer et al. [2011]* used pinhole-type cameras to record the 2D high-time-resolution images of X-ray emissions from triggered lightning, where they observed two chaotic dart leaders from two lightning flashes. They reported a downward speed of 4.5×10^7 m/s for one the events which agreed with dE/dt time-of-arrival measurements, indicating the leader front as the source of X-ray emission. These findings confirmed the CRE as a viable candidate for production of X-rays from runaway electrons at the tip of lightning leader.

1.4 Runaway Electron Avalanche Model (REAM)

Over the last two decades, several Monte Carlo simulation codes have been developed to model the properties of runaway electrons in the air. *Lehtinen et al. [1999]* was the first work to accurately simulate the propagation of runaway electrons inside electric and magnetic fields by taking into account the energy losses from ionization and atomic excitation, Møller scattering and angular diffusion, however the energy loss from bremsstrahlung emission was not included. Later, *Babich*

et al. [2001, 2004, 2005] developed the ELIZA code by including the bremsstrahlung emission of relativistic electrons and positrons, Compton scattering, Rayleigh scattering, photo absorption and pair production. Other Monte Carlo simulation codes developed so far includes the *Roussel-Dupre et al. [2008]* and *Celestin and Pasko [2010]*, where the later work did not take into account the energy losses from bremsstrahlung emission.

Dwyer [2003] developed the Runaway Electron Avalanche Model (REAM) to study the interaction and propagation of relativistic runaway electron avalanches and subsequent energetic radiations for both spatially and time-varying electric and magnetic fields. REAM fully models the development and propagation of RREAs in any gaseous mediums such as terrestrial or planetary atmospheres (e.g. *[Dwyer, 2003; Dwyer and Smith, 2005; Dwyer et al., 2006]*). The Bethe equation, as given by Equation 1.10, is used to consider energy losses of electrons due to ionization and atomic excitation for kinetic energies above a few hundred eV.

$$f_d = \frac{2\pi N Z r_e^2 mc^2}{\beta^2} \times [ln(\frac{m^2c^4(\gamma^2-1)(\gamma-1)}{I^2}) - (1+\frac{2}{\gamma}-\frac{1}{\gamma^2})ln2 + \frac{1}{\gamma^2} + \frac{(\gamma-1)^2}{8\gamma^2} - \delta(\gamma)] \quad (1.10)$$

where N is the number density of the gas atoms and Z is the average atomic number of the gas atoms; r_e is the classical electron radius, mc^2 is the rest mass energy of an electron, $\beta = v/c$ and γ is the Lorentz factor of the energetic electron, I is the effective ionization potential (for the air, I = 85.7 eV), and δ is a correction due to the density effect *[Dwyer, 2007]*. These energy losses create an effective drag force against the electron's velocity, which is called dynamical friction. By setting the electric force equal to the drag force, the threshold kinetic energy K_{th} for the electrons to run away is calculated. Results showed that it is extremely unlikely for electrons to run away with kinetic energies lower than K_{th}. In addition to the dynamical friction, during the propagation of runaway electrons and positrons in the electric field region, there are four major interactions: Møller (Bhabha) scattering of electrons (positrons), positron annihilation, Coulomb scattering and bremsstrahlung radiation, which affect the production and propagation of runaway electrons and positrons. *Dwyer [2007]* has fully explained the details of each interaction in his paper about relativistic breakdown in the planetary atmospheres, so we just briefly review them here.

Firstly, Møller scattering of runaway electrons (and Bhabha scattering for runaway positrons) with atomic or free electrons produces secondary electrons that might also have enough kinetic energy to run away. The cross section of Møller scattering is given by Equation 1.11.

$$\frac{d\sigma_{Moller}}{dK} = \frac{2\pi r_e^2 mc^2}{\beta^2}[\frac{(\gamma^2-1)m^2c^4}{K^2(mc^2(\gamma-1)-K)^2} - \frac{(2\gamma^2+2\gamma-1)}{K(mc^2(\gamma-1)-K)\gamma^2}] + \frac{1}{m^2c^4\gamma^2} \quad (1.11)$$

where K is the kinetic energy of the scattered atomic electron. Given that energy losses from Møller scattering are directly modeled in the simulation, these losses are subtracted from Bethe equation, when the effective drag force is calculated. Since secondary electrons produced by Møller scattering could be energetic as well, total number of runaway electrons increases exponentially for electric field above the runaway threshold. Secondly, the pair production of positrons occurs for photon energies above about 1 MeV and once created, the positrons may also run away. The total cross section for two-photon annihilation with a stationary electron is given by Equation 1.12.

$$\sigma_{annihilation} = \frac{\pi r_e^2}{\gamma+1}[\frac{(\gamma^2+4\gamma+1)}{(\gamma^2-1)} \times ln(\gamma+\sqrt{\gamma^2-1}) - \frac{\gamma+3}{\sqrt{\gamma^2-1}}] \quad (1.12)$$

The average path length of positrons is in the order of a kilometer before they annihilate, so they could travel back to the beginning of avalanche region, where they may seed additional avalanches by producing two 511-keV gamma rays that are then propagated by the simulation and allowed to interact. These 511-keV gamma rays can also produce energetic electrons that run away via Compton scattering or by photoelectric absorption after they Compton scatter down in energy. Thirdly, when these runaway electrons and positrons are traveling through a medium, their elastic scattering with atomic nuclei and electrons tend to deflect them off the field lines, so a greater electric field will be required to overcome the drag force. We have used a Shielded-Coulomb potential, given by Equation 1.13 and valid for both electrons and positrons, which takes into account the charge distribution of both nucleus and atomic electrons to describe Coulomb scattering. By including the nucleus and atomic electrons scattering, a higher threshold field and longer avalanche length will be needed for runaway electrons to develop *[Dwyer, 2007]*.

$$\frac{d\sigma_{Coul}}{d\Omega} = \frac{1}{4}(\frac{Zr_e}{\beta^2\gamma})^2 \frac{(1-\beta^2 sin^2(\theta/2))}{(sin^2(\theta/2)+\frac{\hbar^2}{4p^2a^2})^2} \tag{1.13}$$

Finally, the bremsstrahlung radiation plays an important role in describing the runaway electron propagation in any gaseous medium. The bremsstrahlung cross section is given by Equation 1.14.

$$d\sigma_{brem} = \frac{Z^2 r_e^2 dE_k d\Omega_k d\Omega_p}{4\pi^2 137 E_k p_0} \frac{m^2c^2}{q^4} |F(q)|^2 \{ \frac{p_f^2 sin^2\theta_f (4E_0^2 - q^2c^2)}{(E_f - p_f c\, cos\theta_f)^2} + \frac{p_0^2 sin^2\theta_0 (4E_f^2 - q^2c^2)}{(E_0 - p_0 c\, cos\theta_0)^2} - \frac{2p_f p_0 sin\theta_f sin\theta_0 cos\phi (4E_f E_0 - q^2c^2) + 2E_k^2 (p_f^2 sin^2\theta_f + p_0^2 sin^2\theta_0 - 2p_f p_0 sin\theta_f sin\theta_0 cos\phi)}{(E_f - p_f c\, cos\theta_f)(E_0 - p_0 c\, cos\theta_0)} \tag{1.14}$$

Where

$$q^2 = p_f^2 + p_0^2 + \frac{E_k^2}{c^2} - 2p_0 \frac{E_k}{c} cos\theta_0 + 2p_f \frac{E_k}{c} cos\theta_f - 2p_f p_0 (cos\theta_f cos\theta_0 + sin\theta_f sin\theta_0 cos\phi) \tag{1.15}$$

Here E_k is the energy of the emitted photon, p_0 and p_f are the initial and final momenta of the electron, E_0 and E_f are the initial and final total energies of the electron, θ_0 and θ_f are the angles of the electron's momentum vectors with respect to the photon momentum vector $\vec{k}$, and ϕ is the angle between the planes ($\vec{p_0}$, $\vec{k}$) and ($\vec{p_0}$, $\vec{k}$). Electrons and positrons emit X-rays via bremsstrahlung radiation, which will propagate through the medium and generate secondary electrons as well by Compton scattering, photoelectric absorption, Rayleigh scattering and pair production. Overall, the cross section of Møller (Bhabha) scattering and positron annihilation are proportional to the average atomic number of gas atoms in the medium (Z), while the Coulomb scattering and bremsstrahlung radiation cross sections are proportional to the averaged square atomic number of gas atoms (Z^2).

The REAM code is developed in the Interactive Data Language (IDL) environment and has been used to study gamma-ray and X-ray emissions from lightning. During the REAM Monte Carlo simulation, seeds of runaway electrons with an exponential energy distribution, as described by Equation 1.3, are injected into a volume of air where they accelerate inside a constant ambient

electric field. In our work, the size of avalanche region is chosen to be about 5λ, where λ is the characteristic avalanche length calculated by Equation 1.2. Runaway electrons will be collected at the end of avalanche region, and their position, energy and velocity are stored. Recorded runaway electrons and gamma rays will be then propagated at a specific source altitude and the resulting particles will be recorded at several different detection planes.

CHAPTER 2

GAMMA-RAY FLASHES FROM VENUS

2.1 Composition of Venus' Atmosphere

Venus and Earth are sometimes called twin planets due to their similar properties such as mass, size and structure, but they are also different in many aspects. The presence of an intrinsic magnetic field and large amount of water on the Earth and the dense and acidic atmosphere of Venus are some of the properties that distinguish them. Earth has a surface temperature of 300 K and pressure of 1 bar, while Venus' surface has a temperature of 700 K and a pressure of 100 bar. In contrast, Venus middle clouds have almost the same temperature, pressure and atomic density as at Earth's surface *[Moroz, 1981; Bengtsson et al., 2013].* About 80 percent of Earth's atmosphere is nitrogen, while Venus is covered by a dense gaseous layer of carbon dioxide. Carbon dioxide ($\sim$ 96.5%) and nitrogen ($\sim$ 3.5%) are the main constituents of the Venus atmosphere, but there are also tiny amounts of water vapor, sulfuric acid (H_2SO_4), carbon monoxide (CO), sulfur dioxide (SO_2), carbonyl sulfide (OCS) and Halides (HCL and HF) which have been reported during previous missions *[Bezard and de Bergh, 2007; de Bergh et al., 2006; Mills and Allen, 2007; Svedhem et al., 2007; Krasnopolsky, 2011].* The sulfur cycle in Venus has made its clouds acidic as they contain sulfuric acid particles with an average concentration of 85%. In this work, we have only considered the main constituents, since these small amounts of other species do not have a significant effect on the properties of the energetic electrons and photons.

There have been several efforts to investigate and understand the chemical compositions and environmental properties of Venus' atmosphere, including orbiting satellites and ground-based observations, but less work has been done to address lightning discharges and possible production of high-energy radiation, such as occurs in Earth's atmosphere. *Moroz [1981]* used Pioneer Venus

and a series of Venera spacecrafts (V8, V9, V10, V11 and V12) measurements to present an empirical model of the profile of Venus' atmosphere, which is shown in Figure 2.1. Near the surface, a very thick and dense layer of CO_2 exists up to 30 km. At this region, since the density is so high, the thresholds for runaway electron production and conventional discharges are both much larger (approximately 3000 kV/m) than the maximum electric field that is expected to be produced by charge separation ($\sim$ 5 kV/m) *[Tzur and Levin, 1982]*, so we do not expect to see any discharges here. Venus clouds are divided into three regions: lower, middle and upper clouds. Lower clouds have an approximate temperature of 400 K and pressure of 4 bar, while upper clouds have a temperature of 250 K and pressure of 0.05 bar. Middle clouds of Venus have the most similar conditions (pressure, temperature and atomic density) to those at Earth's surface, which makes

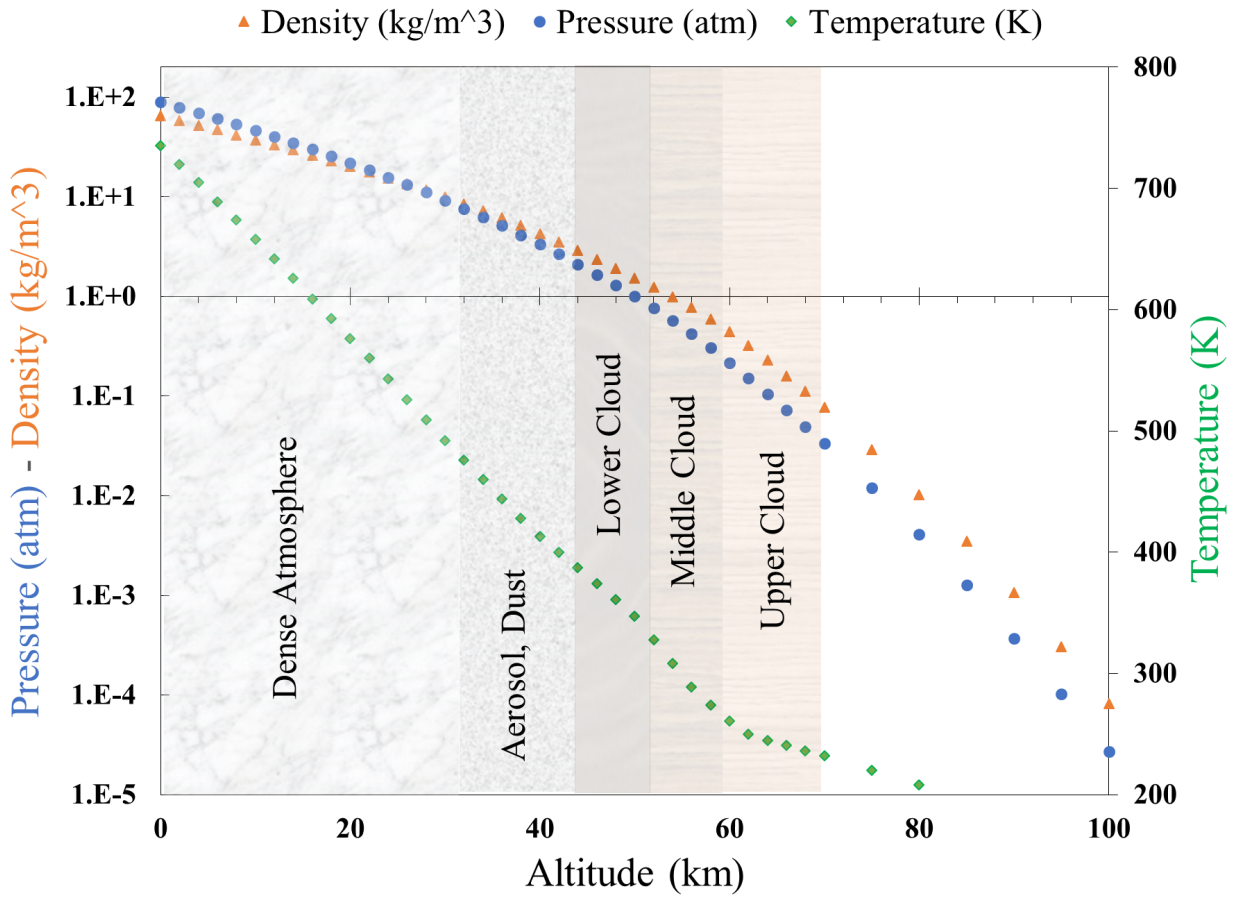

Figure 2.1: Pressure, temperature and density profile of Venus atmosphere from surface up to 100 km. Note that Venus' clouds start from 45 km altitude and extend up to 70 km.

the discharge properties similar in both planets. We have used this region's properties to simulate runaway electron and gamma-ray production and propagation.

2.2 Lightning Observations at Venus

Since 1962, when the first successful in situ observations were done on Venus by Mariner 2, there have been many searches for lightning activity, including radio frequency, spectroscopic and optical measurements. Recent observations by Venus Express (VEX), using a fluxgate magnetometer at ELF frequencies, and Pioneer Venus (PV), using an electric antenna at ELF and VLF frequencies, have recorded signals attributed to lightning discharges in the Venus clouds *[Singh and Russell, 1986; Russell et al., 2011]*. Specifically, Pioneer Venus recorded electric signals over 4 different frequency channels (0.1, 0.73, 5.4 and 30 kHz), of which the 0.1 kHz channel had the strongest signals. Russel et al. considered these signals to be the propagation of whistler mode waves through the Venus atmosphere *[Scarf and Russell, 1983; Russell et al., 2006]*. Data from the magnetometer onboard Venus Express measured the magnetic components of the whistler modes observed by PV at 128 Hz *[Russell et al., 2007]*. In addition, *Levine et al. [1982]* have done laboratory discharge experiments inside a simulated Venus atmosphere to investigate the nitric oxide production rate. They suggested that at the lower and middle parts of the clouds, where the solar UV radiation cannot penetrate, dissociation of carbon dioxide by lightning discharges releases oxygen atoms that could lead to the production of nitric oxide, which would be a significant loss mechanism of atmospheric molecular nitrogen. High-resolution spectroscopic observation of Venus at the NO band at 5.3 μm have revealed three NO lines, with two of them showing the existence of nitric oxide in the lower atmosphere of Venus. It is suggested that lightning is the only source of NO production and if we have similar energy deposition by lightning at Venus and Earth ($\sim 10^{19}$J), the global flashing rate is predicted to be 87 s^{-1} or 6 $km^{-2}y^{-1}$ which agrees with optical observations detected by Venera 9 and 10 spectrometers *[Krasnopolsky, 2006]*.

Borucki et al. [1981] did optical searches at the bandwidth of 500 – 900 nm for lightning at Venus clouds using the star sensor in the PV orbiter and did not see signs of lightning activity. Simulations have revealed that Venusian lightning is expected to radiate strongly in the 600 – 900 nm range, so the failure of the star sensor of PV to detect lightning was suggested to be due to either a low flash rate or low intensity of Venusian lightning *[Moroz, 1981]*. On the other hand, ground-based optical observations of lightning on the night side of Venus captured several potential lightning flashes at the wavelength of 777.4 nm associated with the emission line due to excitation of neutral oxygen, which had optical energies ranging from 10^8 to 2×10^9J *[Hansell et al., 1995]*. Although, the measured flashing rate was 10^{-3} times smaller than that of Earth, all of the six flashes were significantly more energetic than typical lightning flashes at Earth. The Japanese spacecraft, Venus Climate Orbiter (VCO) or Akatsuki, is the most recent mission designed to search for lightning signals at Venus *[Takahashi et al., 2008]*. It carries the Lightning and Airglow Camera (LAC) that observes the oxygen lines spectrum emitted by airglow. Unfortunately, the first attempt to inject the spacecraft into the Venus orbit failed, but the second attempt was successfully done on December 7, 2015. Hopefully this mission could expand our knowledge about lightning activities on the planet Venus. Altogether, observations suggest that lightning discharges may be occurring in the Venus clouds, although, as discussed next, no plausible charging mechanism has been proposed yet.

2.3 Electrification at Venus' Atmosphere

Results from Mariner 10 have revealed the existence of a cloud deck, 50 km above the Venus surface, with a peak liquid content of 1 g/m^3 and an updraft velocity of 1 m/s *[Kliore et al., 1979]*, which are comparable to those at the Earth's clouds with liquid content of 0.3 to 3.0 g/m^3 and updraft of 0.1 to 2.0 m/s. *Cimino and Elachi [1979]* have shown that precipitation on the middle clouds of Venus is likely, making the precipitation-powered charging mechanism applicable in the Venus clouds. Possible charging mechanisms include the Elster-Geitel mechanism involving drop

rebound due to friction between sulfuric acid droplets in the clouds *[Delitsky and Baines, 2015]*. In this mechanism, when a falling particle gets polarized by the ambient electric field and collides with a cloud particle, it loses some charge from its bottom part to the cloud particle. Once the cloud particle rebounds, it will carry away the charge it has gained and leave behind an excess of the sign of charge that is on the top of the particles *[MacGorman and Rust, 1998]*. Then the gravity acting on the droplets and convection will separate the charges over the large-scale regions. The probability of drop rebound has an inverse relation with the surface tension and since the surface tension of sulfuric acid is about 75% of water, this mechanism is more efficient in Venus than Earth [Williams et al., 1983]. The primary issue with the Elster-Geitel mechanism is that only a tiny fraction of collisions leads to rebound, so it might not be strong enough to electrify the clouds exclusively.

The ice crystal-graupel collision is the main electrification mechanism in thunderstorms on Earth, but since the temperature in the Venus clouds is mostly above freezing point, any charging mechanism is suggested to be a warm cloud electrification *[Williams et al., 1983]. Michael et al. [2009]* have investigated charge accumulation on the particles of Venus' clouds due to charge transfer of ions and attachment of electrons in the atmosphere. The ratio of positive to negative charges accumulated on cloud particles suggests that the middle and upper clouds contain more negatively charged particles than the lower cloud region, although they have reported that the charging current ($\sim 10^{-14}$A/m^2) is too small compared with the leakage current (10^{-8} to 10^{-7}A/m^2) to be able to generate the electric field necessary for a lightning discharge. Violent rupture of water drops is another possible charging mechanism, but the resulting charge separation is at least 2 orders of magnitude too small to be considered as the primary thunderstorm electrification on Venus.

Since a large electric field magnitude is required for lightning, the high altitude of Venus' clouds would prevent discharges to the ground and any possible discharge would be intercloud or intracloud *[Williams et al., 1983; Russell et al., 2006; Yair et al., 2008]*. Most of these discharges are suggested to be upward going, which means the branching and propagation starts from lower clouds towards middle and upper clouds. Even if we assume that lightning happens inside the

clouds, there are some substantial debates about charging mechanism, which needs further studies.

2.4 High-Energy Gamma Rays' Detection at Venus

The Orbiter Gamma Burst Detector (OGBD) instrument onboard Pioneer Venus was designed to detect and identify cosmic gamma-ray bursts (GRBs) spatial distribution and energy spectrum *[Evans et al., 1979]*. It had a pair of similar CsI scintillation photon counters mounted oppositely on the spacecraft platform and was sensitive to energy range of 100 keV to 2.0 MeV (divided into four energy channels). After only 3 hours of its operation, it detected the first cosmic gamma-ray burst (GRB) while it was still close to Earth. Between 1978 and 1992, it detected more than 200 GRBs and at least half of them are verified by other spacecrafts and the statistical analysis have shown a uniform spatial distribution for the bursts source population *[Chuang et al., 1992]*. Since this instrument was not intended to investigate Venus, the collected data were not analyzed or published widely. Recently, *Lorenz and Lawrence [2015]* reinvestigated those data to consider the possibility of gamma-ray generation and propagation out of Venus clouds. They used 15-min averaged count rates data of OGBD in the Venus orbit over an 11-year period of 1979-1989. The observed large-scale count rate structure correlated very well with the cosmic ray muon flux measured at Thule, Greenland over those years, suggesting that the observed events did not originate from Venus atmosphere and those enhancements are associated with solar cycle activities. The count rate behavior in three different energy bins (100 – 200 keV, 1000 – 2000 keV and 100 – 2000 keV) were almost similar during individual events. Although the overall behavior of count rate shows a significant increase in number of detected photons, the time resolution of data is probably too low (15 minutes) to detect any possible Venusian gamma-ray flashes. If TGFs from Earth were measured with such a low time resolution, they would not be detected because of their short time durations. Moreover, by modeling gamma-ray propagation through Venus atmosphere using MCNPX (Monte Carlo Neutral Particle eXtended), they reported that if the gamma-ray source altitude would be at the top of clouds ($\sim$ 75 km), its amplitude will be attenuated by only a factor

of a few, but if it originates in middle clouds ($\sim$ 60 km), the attenuation rate would be about two orders of magnitude. In this , we expand upon these calculations and investigate the generation and transport of runaway electrons and high-energy gamma rays and the possibility of detection of those gamma rays at low-Venus orbit.

2.5 Results and Discussion

2.5.1 Relativistic Runaway Electron Avalanche Properties at Venus

To describe the RREA mechanism in the clouds of Earth and Venus, we have calculated and plotted the required characteristic length for an avalanche to develop versus ambient electric field magnitude, along with empirical formula given by Equation 1.2. This empirical formula could also be written in form of Equation 2.1, where Γ is the fitting constant and E_{th} is the runaway electric field threshold.

$$\lambda = \frac{\Gamma}{(E - E_{th}) \times n} \tag{2.1}$$

For each point we have injected 10 seed of energetic electrons (N_0 = 10) with the steady state energy spectrum at the beginning of avalanche region. Such seed particles could be provided by solar and galactic cosmic rays which is reasonable, given that the ionization rate is maximum at an altitude of 63 km above the Venus surface *[Nordheim et al., 2015]*. These injected energetic electrons are accelerated in the uniform electric field and their number increases exponentially due to scattering with atoms in the medium. By collecting runaway electrons at the end of region and using $N_{re} = N_0 exp(z/\lambda)$, the characteristic length of the avalanche is found for that electric field value. These results are plotted for electric field magnitudes of 300 – 3000 kV/m in Figure 2.2.

Fitting the avalanche length leads to the empirical formula given by Equation 2.1, and leads to the Γ and E_{th} for the Earth to be equal to 7.12$\pm$0.16 MeV and 276$\pm$1.3 kV/m, which agrees with reported threshold field by *Dwyer [2003]* and *Babich et al. [2004]*, while those for Venus are equal to 7.15$\pm$0.13 MeV and 276.2$\pm$1.5 kV/m. These results are valid for the electric field magnitudes greater than 350 kV/m. The value of E_{th} from the empirical fit is close to the RREA

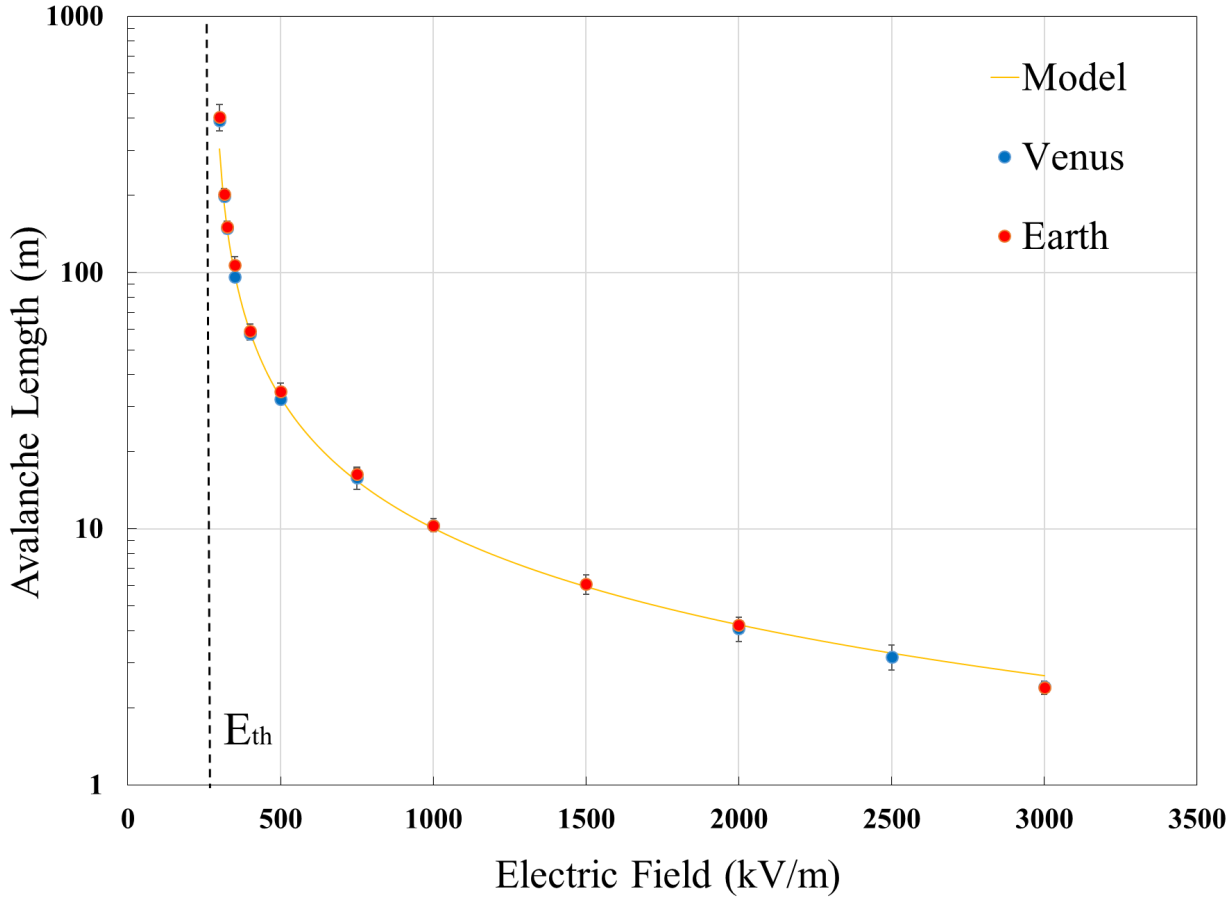

Figure 2.2: Characteristic avalanche length of runaway electrons of Earth and Venus for electric fields between 300 kV/m and 3000 kV/m. The solid curve shows the empirical formula in Equation 2.1 for the Γ = 7.3 MeV and E_{th} = 276 kV/m.

threshold values of 286.1 kV/m for Earth and 286.3 kV/m found here for Venus. The conventional breakdown field for a pure CO_2 atmosphere is reported to about %95 of the air, so assuming that E_{th} for both atmospheres is the same, the ratio of E_k/E_{th} would be still around 10. Since the charging mechanism on Venus is not known, we might expect different discharge properties such as threshold electric field and energy spectrum, but if we look at the cross section of each interaction individually, they are proportional to the average atomic number of gas atoms in the medium. The effective drag force (Bethe equation) and the cross section of Møller (Bhabha) scattering and positron annihilation depend on the average atomic number of medium (Z), while the cross section of coulomb and bremsstrahlung scatterings is a function of averaged square atomic number

(Z^2). Based on the atomic number and mean excitation energy of the Earth (7.26 C and 85.7 eV) and Venus (7.32 C and 88.45 eV) atmospheres given in Table 2.1, the difference is less than 3%, which might not cause any significant change in the cross sections and subsequently the discharge properties of runaway electrons, so these similarities are not unexpected.

Planet	**Averaged atomic number of gas atoms (Z)**	**Averaged square atomic number of gas atoms (Z^2)**	**Atomic density (m^{-3})**	**Mean excitation energy (eV)**
Earth	7.26	53.45	5.38×10^{25}	85.7
Venus	7.32	54.46	5.38×10^{25}	88.45

Table 2.1: A comparison of averaged atomic number of gas atoms, atomic density, and mean excitation energy of the Earth and Venus atmosphere.

Roussel-Dupre et al. [2008] used kinetic theory solutions to calculate scaled runaway threshold electric field for both Earth and Venus, which are reported to be 215 kV/m and 320 kV/m. Their value of runaway threshold for Earth is lower than other estimates found by *Dwyer [2003]* and *Babich et al. [2004]* ($\sim$ 284 kV/m), while we have found similar threshold electric field and avalanche characteristic length for the Venus and Earth. This latter discrepancy may be explained by the fact that Venus atmosphere's (mostly carbon dioxide) molecules have 3 atoms per molecule and Earth's atmosphere contains diatomic molecules, this 2/3 ratio of threshold fields in their results is probably due to considering the same molecular densities (not atomic densities) for the both atmospheres which leads to a 1.5 times larger atomic density at Venus. This means that if we compare threshold fields for the same atomic densities, the result would be almost similar, but it still could not explain the low value of threshold they have reported for Earth. Since the threshold electric field depends on atomic density of the medium, for the upper (lower) clouds of Venus we expect a lower (higher) threshold field. Although there is no direct measurement of electric field magnitude inside Venus clouds yet, RREA production in Venus needs nearly the same electric field strength as Earth. If the electric fields on Venus are strong enough to make lightning, then it seems plausible that they are also strong enough to generate RREAs, similar to Earth.

The energy spectra of runaway electrons (number of runaway electrons per unit energy) is an exponential function of the electron's energy, as described by Equation 1.3. This formula along

with Monte Carlo simulation for the Venus middle clouds and Earth are plotted in Figure 2.3. The model is valid for energies above a few hundred keV. The energy spectrum given by Equation 1.3 is independent of the electric field and the density of the medium, which leads to an average energy of 7.3 MeV for runaway electrons at both planets. The calculated average energy of runaway electrons at Earth agrees with the results of *Babich et al. [2004]* and *Roussel-Dupre et al. [2008]*. The similarities between the cross section of interactions for Earth and Venus leads to similar energy distributions for runaway electrons. If the runaway electrons stay in the high field region for long distances, they will accelerate to many tens of MeV in energies, but the relativistic feedback mechanism may limit the maximum possible energy they can gain. Therefore, it is expected that

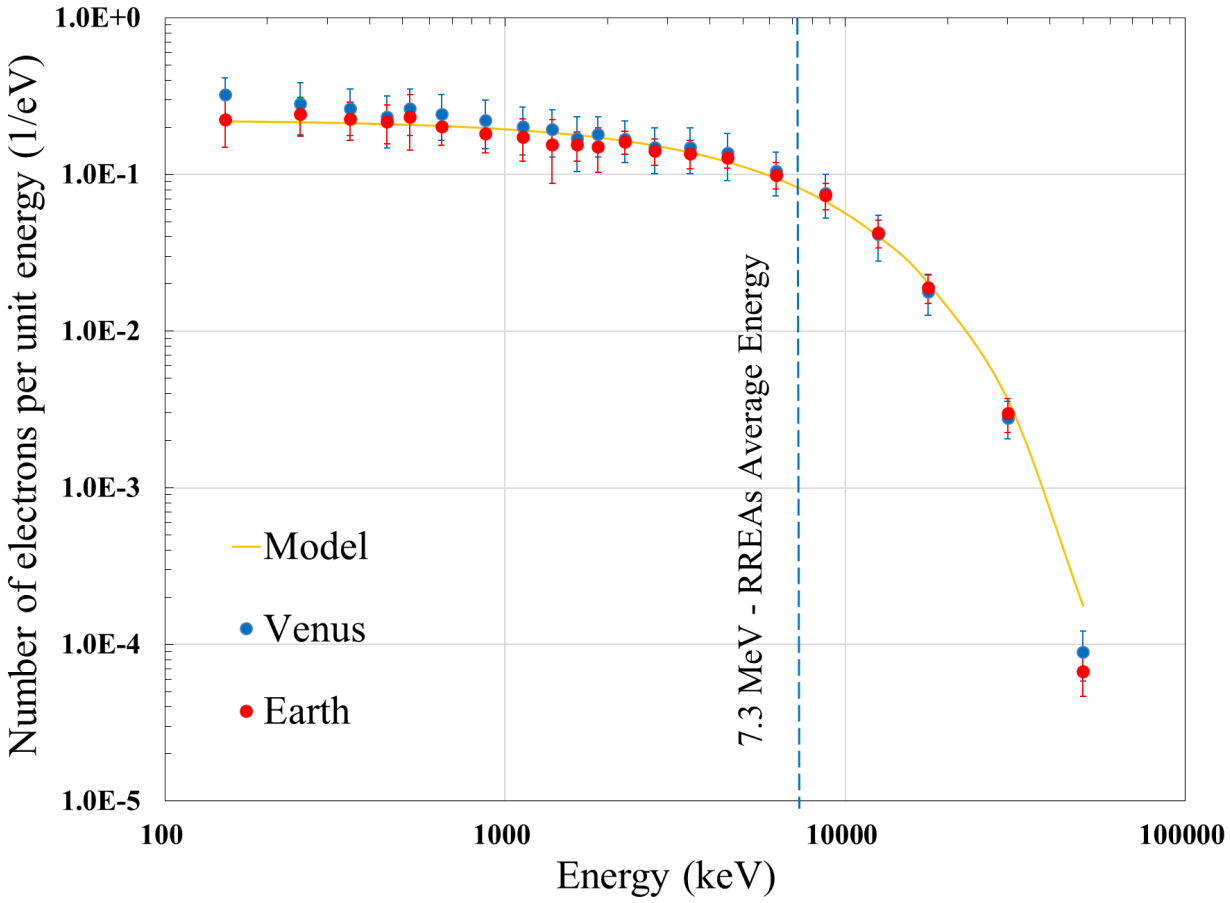

Figure 2.3: Runaway Electrons energy spectra produced by RREAs on the Earth and Venus. The solid curve shows the analytical model which is exponentially for energies above hundred keV. The dashed line shows the average energy of runaway electrons.

the bremsstrahlung spectrum at the source, produced by the runaway electrons, will be similar for both planets.

2.5.2 Gamma rays' Detection at Low-Venus Orbit

The propagation of runaway electrons in Venus clouds leads to bremsstrahlung emission (X-rays generation), which is due to interaction with carbon, oxygen and nitrogen atoms. These photons can travel long distances up to the low-Venus orbit, but their fluence is dependent on the total column depth of the atmosphere along their path. An empirical model of mass density *[Moroz, 1981]* is used to calculate the total mass in a column of atmosphere above each altitude, which is plotted in Figure 2.4. This plot shows how much mass is located along the path of a photon between the specific altitude and 550 km above surface. Since most of Venus' atmosphere is made of CO_2 and N_2, small amounts of other species, including cloud particles, do not have significant effects on the column depth and transport of gamma rays in this work. Naturally, a greater column depth means that the possibility that a photon could escape out of the atmosphere is less. The average column depth at the Earth upper clouds' altitude ($\sim$ 20 km above surface) is about 50 g/cm^2, which is almost equal to its value at top of Venus' clouds, so gamma rays generated in the middle and upper clouds have a similar chance to escape out of its atmosphere compared with those from the Earth's clouds. To study the upward propagation of gamma rays through the Venus atmosphere correctly, the modified scaleheight at middle clouds altitude was needed. *Roos et al. [1993]* have used infrared data of NIMS instrument at the time of the Galileo flyby of Venus to report a 5.2 km scaleheight at upper clouds (65 – 75 km) of Venus, but since there is a variable temperature over clouds, we used density profile between altitudes of 52 and 100 km to calculate the exact scaleheight in the middle clouds which was about 7.7 km.

To calculate photons fluence at low-Venus orbit, we have initiated the recorded photon output of runaway electrons which were accelerated in the electric field of 400 (kV/m$\times$n) at the source altitudes of 55 km to 70 km and calculated the fluence of photons at 550 km above the Venus surface which is shown in Figure 2.5. A TGF usually generates about 10^{17} gamma-ray photons

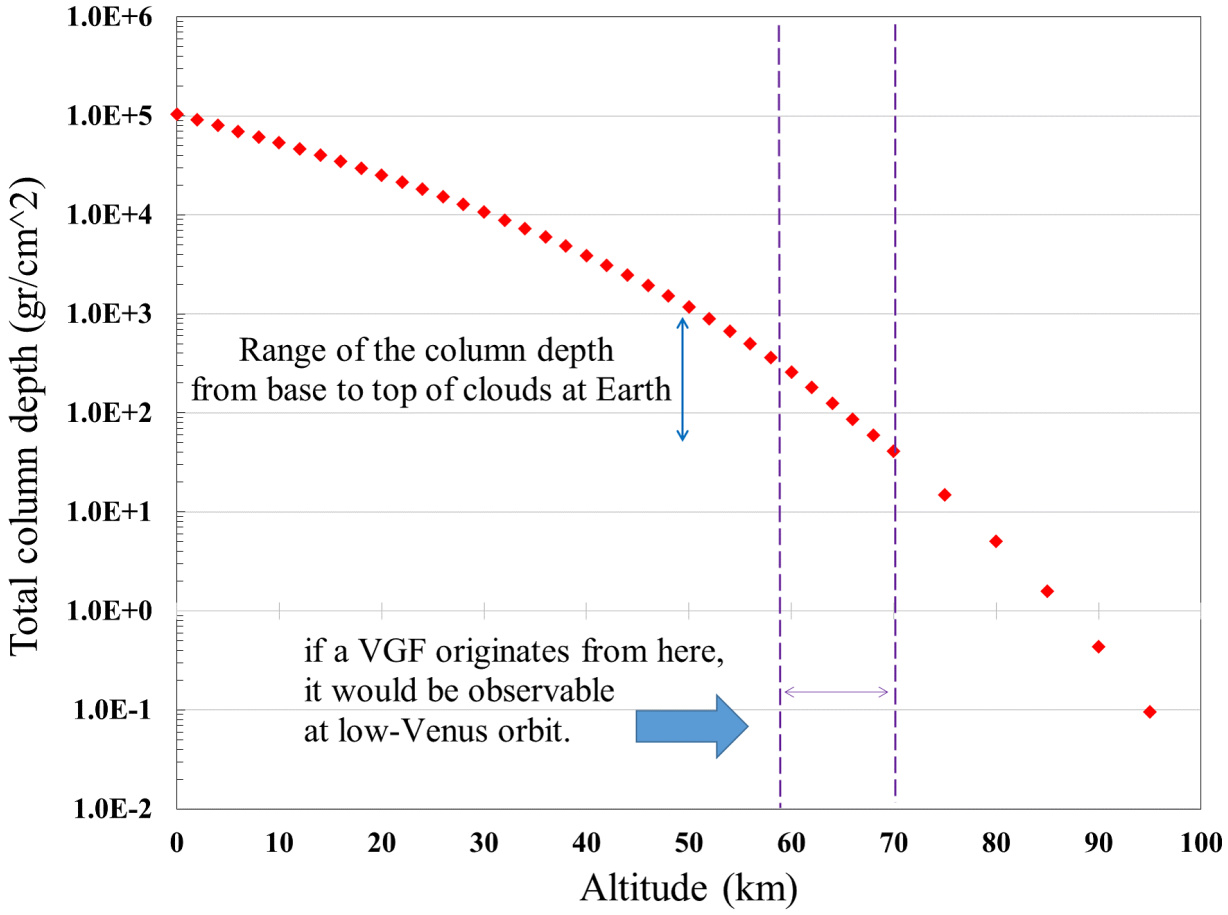

Figure 2.4: Total column depth of atmosphere above each point versus its altitude-Note that larger column depth means that gamma rays have a lower chance to escape out of atmosphere.

on Earth with energy range of 100 keV to 20 MeV *[Dwyer and Smith, 2005; Ostgaard et al., 2008]*. This number of photons may depend on the characteristics of lightning discharges on other atmospheres (such as chemistry, electric potential and etc.), but assuming that TGFs on Earth and gamma-ray flashes on Venus act similar, the reported fluence represents the number of escaped photons with respect to the initial photons *Smith et al. [2011*b*]*. If these photons are being generated at the lower clouds of Venus (less than 50 km), they would not have a chance to escape due to large column depth above them, but if a gamma-ray flash occurs in the middle clouds ($\sim$ 58 km), the measured fluence of gamma rays would be in order of 10^{-3} photons/cm^2 and if it happens in the upper clouds of Venus ($\sim$ 70 km), the measured fluence would be around 4 photons/cm^2. Therefore, if the Venusian Gamma-ray Flashes originate from the top of the clouds (65 – 70 km),

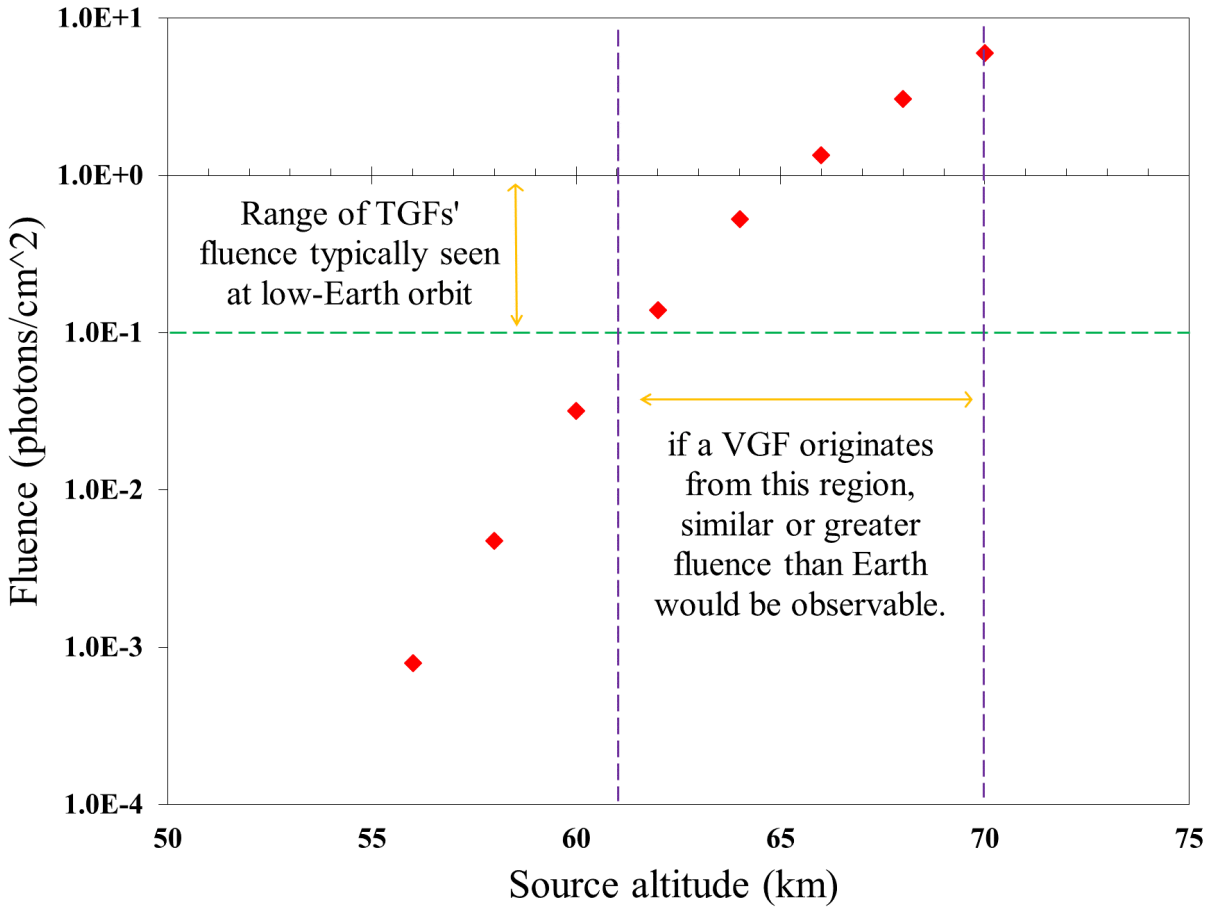

Figure 2.5: Gamma rays fluence at 550 km above Venus surface versus source altitude, assuming similar number of gamma rays produced at source as TGFs on Earth.

their fluence in the low-Venus orbit would be about 4 times greater than TGFs fluence detected on the low-Earth orbit. Based on this, the gamma-ray fluence would be attenuated by at least 3 orders of magnitude, if the source moves from the top of the clouds to the middle clouds. These numbers are in good agreement with the *Lorenz and Lawrence [2015]* results who have reported 2 – 3 orders of magnitude attenuation rate for gamma rays' amplitude, when the source altitude moves from top of cloud ($\sim$ 75 km) to the middle clouds ($\sim$ 65 km). Although they have reported the normalized current of gamma rays at Venus orbit with discrete incident energies from 0.2 to 9.0 MeV, a more realistic result would be a weighted average of those calculations (e.g. gamma-ray fluence for an energy distribution, not a single energy value), such as we have reported in this work. The typical fluence of gamma rays for a TGF seen at low-Earth orbit is reported to be between 0.1

photons/cm^2 (dashed line) and 1 photons/cm^2 (solid horizontal line) *[Briggs et al., 2010; Ostgaard et al., 2012]*. It seems that similar atmospheric conditions at the clouds of Earth and Venus could cause analogues discharges at both planets leading to the similar gamma-ray fluences at the low orbit of these planets.

2.6 Conclusion

We used the Runaway Electrons Avalanche Model (REAM) to simulate the generation and propagation of runaway electrons and gamma-ray flashes through Venus middle and upper clouds. We assumed that the suggested charging mechanisms for Venus clouds are strong enough to produce RREAs. Results from avalanche length and energy spectrum of runaway electrons showed that Venus middle clouds and Earth sea level have almost the same runaway electron properties, which leaded to the same threshold electric field (286 kV/m)$\times$n. The average energy of runaway electrons was estimated to be about 7 MeV which was in agreement with recent works. Since the average atomic number of gas atoms and mean excitation energy on both planets were so close, such similarities were not unexpected. We also studied the propagation of generated gamma rays by bremsstrahlung emission through Venus clouds and calculated their fluence at the low-Venus orbit. For the source altitude between 58 and 70 km, we calculated the fluence to be between 10^{-3} and 4 photons/cm^2. It seems if electrification occurs in the clouds of Venus, and the gamma-ray flashes initiate in the middle and upper clouds are similar to that on the Earth, they should be detectable by spacecrafts at low-Venus orbit. We propose calling these events Venusian Gamma-ray Flashes (VGFs).

CHAPTER 3

POLARIZATION OF TGFS AND X-RAYS FROM LIGHTNING

3.1 Introduction

Polarimetry of hard X-rays and gamma-ray bursts has been an interesting subject in astrophysics over the last few decades. The degree of linear polarization may provide a better understanding of the source geometry, acceleration mechanism and transport of gamma rays. There have been numerous studies using both experimental and analytical methods to understand the polarization of cosmic gamma-ray bursts (solar flares X-rays, etc.). Experimental polarimetry of hard X-rays and gamma rays includes both space-based (e.g., CGRO *[Lei et al., 1996]*, RHESSI *[Lin et al., 2002]*, INTEGRAL *[Winkler et al., 2003]*, POET *[Hill et al., 2008]*, GAP *[Yonetoku et al., 2011]* and NuSTAR *[Lotti et al., 2012]*) and balloon measurements (e.g., GRAPE *[Bloser et al., 2005]*, GRIPS *[Greiner et al., 2012]* and PoGOLite *[Chauvin et al., 2016]*). As an example, RHESSI has provided useful information about linear polarization and morphology details of solar flares in the chromospheric and coronal X-ray sources *[Suarez-Garcia et al., 2006]*. TGFs are bright bursts of gamma rays produced by thunderstorms, typically observed by spacecraft in the low-Earth orbit. Unfortunately, it has been difficult to disentangle the source altitude and the width and direction of the gamma-ray beam using single point spacecraft measurements, which has hampered attempts to constrain TGF models. To this date, no detailed study of polarization of TGFs have been done. To better understand the source mechanisms of TGFs and X-rays, we address the following question: Do TGFs and X-rays from lightning have observable polarization, and if so, what would this polarization tell us about their source? In this chapter, the REAM Monte Carlo code, which has been used to model TGFs for many years *[Dwyer and Smith, 2005; Dwyer, 2007; Bagheri and Dwyer, 2016]*, has been modified to record the linear polarization of X-rays and gamma rays as a function

of source altitude and beam geometry.

3.2 Polarization

The gamma rays produced by bremsstrahlung emissions of energetic runaway electrons interact with the air via photoelectric absorption, Compton scattering and pair production, as they propagate up and out of the atmosphere. Secondary electrons and positrons, created during these interactions, may subsequently emit more bremsstrahlung photons or, for the positrons, annihilation photons. Bremsstrahlung emission, Compton scattering, pair production and pair annihilation all produce some degree of linear polarization of the gamma rays *[May, 1951; Gluckstern and Hull, 1953; Motz, 1956; Olsen and Maximon, 1959]*. These processes are modeled in detail by the Monte Carlo simulation, and the resulting linear polarization states are recorded for each photon. The results showed that polarization from pair annihilation is negligible, so we have ignored it here. Also, the runaway electrons (positrons) produced in pair production undergo Møller scattering and bremsstrahlung emission (photons annihilation), so the polarization information will be lost due to multiple interactions, so the focus of this work will be on the first two interactions. In this simulation, the electron and positron spin states are assumed to be unpolarized. This is justified, since a clear majority of bremsstrahlung emission is produced by runaway electrons generated by the RREA process, which are inherently unpolarized. In the subsections below, details are given about the separate polarization calculations and total polarization matrices.

3.2.1 Polarization from Bremsstrahlung

The bremsstrahlung process used by the Monte Carlo simulation is described in *Dwyer [2007]*. For a given initial electron energy and momentum, the photon energy and momentum and the final energy and momentum of the electron are found. With this information, the degree of linear polarization of the photons is then found as given by Equation 3.1:

$$P = \frac{d\sigma_{III} - d\sigma_{II}}{d\sigma_{III} + d\sigma_{II}} \tag{3.1}$$

where $d\sigma_{III}$ is the differential cross section for the polarization vector perpendicular to the scattering plane and given by Equation 3.2, containing the vectors $\vec{p_0}$ (initial momentum of the electron) and $\vec{k}$ (momentum of the photon), i.e., $\hat{e}_{III} = \frac{\vec{p_0}\times\vec{k}}{|\vec{p_0}\times\vec{k}|}$. $d\sigma_{II}$ is the differential cross section for the polarization vector in the scattering plane and given by Equation 3.3, containing the vectors $\vec{p_0}$ and $\vec{k}$, i.e., $\hat{e}_{II} = \frac{\vec{k}\times\hat{e}_{III}}{|\vec{k}\times\hat{e}_{III}|}$ *[May, 1951]*. In this work, although shielding is included in the calculation to find whether or not photon emission occurs and to calculate the photon energy and emission angle, for simplicity, shielding is not included in the cross sections for the separate polarization directions. Following *Gluckstern and Hull [1953]*, including their notation:

$$\begin{aligned} d\sigma_{III} &= (Z^2e^6/8\pi)(dk/k)(p/p_0)d\Omega_0 \times \{-(5E_0^2+2EE_0+m^2)/(p_0^2\Delta_0^2) \\ &-(p_0^2-k^2)/(T^2\Delta_0^2) - 2k/(p_0^2\Delta_0) + (L/pp_0)[(2E_0^2(E_0^2+E^2) \\ &-m^2(5E_0^2-2EE_0+E^2))/(p_0^2\Delta_0^2) + k(E_0^2+EE_0-2m^2)/(p_0^2\Delta_0)] \\ &+(\varepsilon^T/pT)[k/\Delta_0 - k(p_0^2-k^2)/(T^2\Delta_0)+4] - (1/p_0^2 sin^2\theta_0)(2L/pp_0) \\ &\times(2E_0^2 - EE_0 - m^2 - (m^2k/\Delta_0)) \times 4\varepsilon^T(\Delta_0-E)^2/(pT) - 2\varepsilon(\Delta_0-E)/p]\} \end{aligned} \tag{3.2}$$

$$\begin{aligned} d\sigma_{II} &= (Z^2e^6/8\pi)(dk/k)(p/p_0)d\Omega_0 \times \{8m^2 sin^2\theta_0(2E_0^2+m^2)/(p_0^2\Delta_0^4) \\ &-(5E_0^2+2EE_0+5m^2)/(p_0^2\Delta_0^2) - (p_0^2-k^2)/(T^2\Delta_0^2) + 2(E+E_0)/(p_0^2\Delta_0) \\ &+(L/pp_0)[4E_0m^2 sin^2\theta_0(3km^2-p_0^2E)/(p_0^2\Delta_0^4) + (2E_0^2(E_0^2+E^2) \\ &-m^2(9E_0^2-4EE_0+E^2)+2m^4)/(p_0^2\Delta_0^2) + k(E0^2+EE_0)/(p_0^2\Delta_0)] \\ &+(\varepsilon^T/pT)[4m^2/\Delta_0^2 - 7k/\Delta_0 - k(p_0^2-k^2)/(T^2\Delta_0) - 4] - 4\varepsilon/(p\Delta_0) \\ &+(1+p_0^2 sin^2\theta_0)\times[(2L/pp_0)(2E_0^2 - EE_0 - m^2 - (m^2k/\Delta_0)) \\ &-4\varepsilon^T(\Delta_0-E)^2/(pT) - 2\varepsilon(\Delta_0-E)/p]\} \end{aligned} \tag{3.3}$$

where $\vec{p}$ is the final momentum of the electron; E_0 and E are the initial and final total energy of the electron; θ_0 is the angle of $\vec{p_0}$ with respect to $\vec{k}$; $d\Omega_0$ is the element of solid angle in the direction of, taken with respect to $\vec{k}$; m is the mass of the electron; $T = |\vec{p_0} - \vec{k}|$; $L = ln[(EE_0 -$

$m^2 + pp_0)/(EE_0 - m^2 - pp_0)]$; $\varepsilon = ln[(E+p)/(E-p)]$; $\varepsilon^T = ln[(T+p)/(T-p)]$; and $\Delta_0 = E_0 - p_0 cos\theta_0$. The constant $\hbar$ and c are taken to be 1, and all the other symbols have their usual meaning. For the emitted photon, the polarization direction is randomly chosen with the probabilities for the parallel and perpendicular direction given by $\frac{d\sigma_{III}}{d\sigma_{III}+d\sigma_{II}}$ and $\frac{d\sigma_{II}}{d\sigma_{III}+d\sigma_{II}}$, respectively, thus resulting in the correct degree of polarization. Because the spin of the incident electron is assumed to be unpolarized, there is no preferred azimuthal direction with respect to the direction of the incident electron. Thus, the azimuthal direction is chosen randomly. Once found, the polarization direction is stored by the Monte Carlo simulation along with the photon's position, momentum and energy. The polarization is used when calculating the Compton scattering direction and polarization state.

3.2.2 Polarization from Compton Scattering

The dominant cause of polarization in most cases is Compton scattering. For an incident photon with a given energy, momentum and polarization vector, the probability of Compton scattering, the scattering direction, polarization and final energy are found from the Klein-Nishina formula *[Berestetskii et al., 1982]*, along with conservation of energy and momentum. For a photon initially moving in the $+z$ direction with angular frequency ω, and polarization vector in the $+x$ direction, the differential cross-sections for Compton scattering for the two polarization directions are given by Equation 3.4 and 3.5 as follows:

$$\frac{d\sigma_{III}}{d\Omega} = \frac{r_0^2}{2}(\frac{\omega'}{\omega})(\frac{\omega'}{\omega} + \frac{\omega}{\omega'} - 2 + 4sin^2\varphi) \tag{3.4}$$

and

$$\frac{d\sigma_{II}}{d\Omega} = \frac{r_0^2}{2}(\frac{\omega'}{\omega})(\frac{\omega'}{\omega} + \frac{\omega}{\omega'} - 2 + 4cos^2\theta cos^2\varphi) \tag{3.5}$$

where ω' is the angular frequency of the scattered photon, θ and φ are the polar and azimuthal angles, respectively, with respect to the z-direction. Following the notation defined earlier, $d\sigma_{III}$ and $d\sigma_{II}$ are the cross-section for the polarization of the scattered photon that is perpendicular and parallel to the scattering plane, respectively. As can be seen, the azimuthal direction of the

scattered photon depends upon the polarization of the incident photon. In the Monte Carlo simulation photons may move in all directions. The directions of the incident, scattered photons and the polarization directions defined in Equations 3.4 and 3.5 are all rotated to match the direction and polarization of the incident photon in the simulation. Then the new polarization direction is stored along with the photon's new momentum and energy.

3.2.3 Polarization Tensor

To quantify the linear polarization magnitude and direction, the polarization tensor $\rho_{\alpha\beta}$ is calculated. The polarization tensor, which is related to the quantum mechanical density matrix, is found as given by Equation 3.6 *[Landau and Lifshitz, 1975]*:

$$\rho_{\alpha\beta} = \overline{\varepsilon_\alpha \varepsilon_\beta} = \frac{1}{N}\sum_{n=1}^{N} \varepsilon_\alpha^n \varepsilon_\beta^n \qquad \alpha, \beta = 1, 2 \tag{3.6}$$

where ε_α^n is the α-component (e.g., the x or y component) of the polarization vector for the n^{th} photon and N is the total number of photons. For each gamma-ray, the local x and y unit vectors (coordinates 1 and 2) are found as given by Equation 3.7.

$$\hat{e}_x = \frac{\hat{e}_z \times \vec{k}}{|\hat{e}_z \times \vec{k}|} \quad and \quad \hat{e}_y = \frac{\vec{k} \times \hat{e}_x}{|\vec{k} \times \hat{e}_x|} \tag{3.7}$$

which forms a right-handed coordinate system with the gamma-ray directed along the z-axis. When there is no circular polarization, the polarization tensor may be written as Equation 3.8.

$$\rho_{\alpha\beta} = \begin{pmatrix} 1 + l cos2\varphi & l sin2\varphi \\ l sin2\varphi & 1 - l cos2\varphi \end{pmatrix} \tag{3.8}$$

where l is the magnitude of the linear polarization, and φ is the angle with respect to the x-axis of the linear polarization direction. Combining Equations 3.6 and 3.8 results to:

$$l = [2\rho_{12}^2 + 2\rho_{21}^2 + (\rho_{11} - \rho_{22})^2]^{\frac{1}{2}} = [2(\overline{\varepsilon_1\varepsilon_2})^2 + 2(\overline{\varepsilon_2\varepsilon_1})^2 + (\overline{\varepsilon_1\varepsilon_1} - \overline{\varepsilon_2\varepsilon_2})^2]^{\frac{1}{2}} \tag{3.9}$$

and

$$tan2\varphi = \frac{\rho_{12} + \rho_{21}}{(\rho_{11} - \rho_{22})} = \frac{\overline{\varepsilon_1\varepsilon_2} + \overline{\varepsilon_2\varepsilon_1}}{\overline{\varepsilon_1\varepsilon_1} - \overline{\varepsilon_2\varepsilon_2}} \tag{3.10}$$

where the over-bar sign shows the averaged value of that term for the total number of photons. The polarization vectors are recorded for all gamma rays in the simulation passing through horizontal planes above the ground. For each gamma-ray recorded at the horizontal planes, the x and y coordinates of its polarization vector are found. The data are separated into annular bins in the horizontal plane, with the origin being directly above or below the TGF source location, depending on the direction of propagation. The gamma rays were separated according to their energies, and only gamma rays with wave vectors within 5 degrees of the spherical radial vector, directed away from the TGF source were accepted. For each annular bin, the elements of the polarization tensor were calculated from the components of the polarization vectors of all accepted gamma rays, and the magnitudes and angles of the polarization and their error bars (see Appendix A) were found.

3.2.4 How Many Counts Are Required for Measuring Polarization?

To have a reliable measurement of linear polarization of gamma rays and X-rays, a certain number of conditions need to be satisfied such as large field-of-view (FOV), high modulation factor (μ), wide energy range, large effective area and low Minimum Detectable Polarization (MDP). Modulation factor depends on the geometry of detector and represents the quality of the polarization signal. The polarization sensitivity of detector is typically measured in terms of the Minimum Detectable Polarization which at 99% confidence level is defined given by Equation 3.11 *[Weisskopf et al., 2010]*.

$$MDP = \frac{4.29}{\mu_{100} \times S}\sqrt{S + B} \tag{3.11}$$

where μ_{100} is the modulation factor for a 100% polarized source, S is the total source counts and B is total background counts. Here we will use the characteristics of the Gamma Ray Polarimeter Experiment (GRAPE) detector to calculate how many photons are needed for a reliable measure-

ment of the polarization of TGFs and X-rays *[McConnell et al., 2018]*. If we assume B = 0 (ideal case), the minimum number of required counts could be written as Equation 3.12.

$$S = (\frac{4.29}{\mu_{100} \times MDP})^2 \tag{3.12}$$

With a modulation factor of 0.5 and minimum detectable polarization equal to 10%, about 7400 counts are needed for an ideal detector with efficiency of 100%. The detector efficiency which is defined as effective area divided by geometrical area is about 8% for GRAPE, so considering the same value here, about 92,000 counts are needed to measure 10% linear polarization. This means that for a typical polarimeter with an effective area of 10 cm^2, an equivalent fluence of about 9200 photons/cm^2 is needed. In the next following sections, we will use such level of fluence as a threshold to validate the possibility of measuring linear polarization of TGFs and X-rays in different scenarios such as in-space, balloon-borne and ground-level measurements.

3.3 Results and Discussion

3.3.1 Polarization of TGFs in the Low-Earth Orbit

TGFs seen in the low-Earth orbit typically originate at thunderstorm altitudes ($\sim$ 12.5 km) *[Cummer et al., 2015]* from bremsstrahlung radiation of energetic runaway electrons that are accelerated in the strong electric fields. Along their path through the atmosphere, these photons might be absorbed via the photoelectric effect or pair production, or have multiple Compton scatterings which alters their polarization. To calculate their linear polarization in space, the photons created during full RREA simulations are propagated upward from source altitudes of 12.5 km (mid-altitude) and 20 km (high-altitude) and collected in the low-Earth orbit ($\sim$ 500 km). We report the linear polarization and fluence of photons versus the radial distance in three energy bands including 60 – 200 keV, 200 – 500 keV and 500 – 1000 keV in Figure 3.1. These energy bands were chosen to match existing polarimeters *[McConnell et al., 2013, 2018]*.

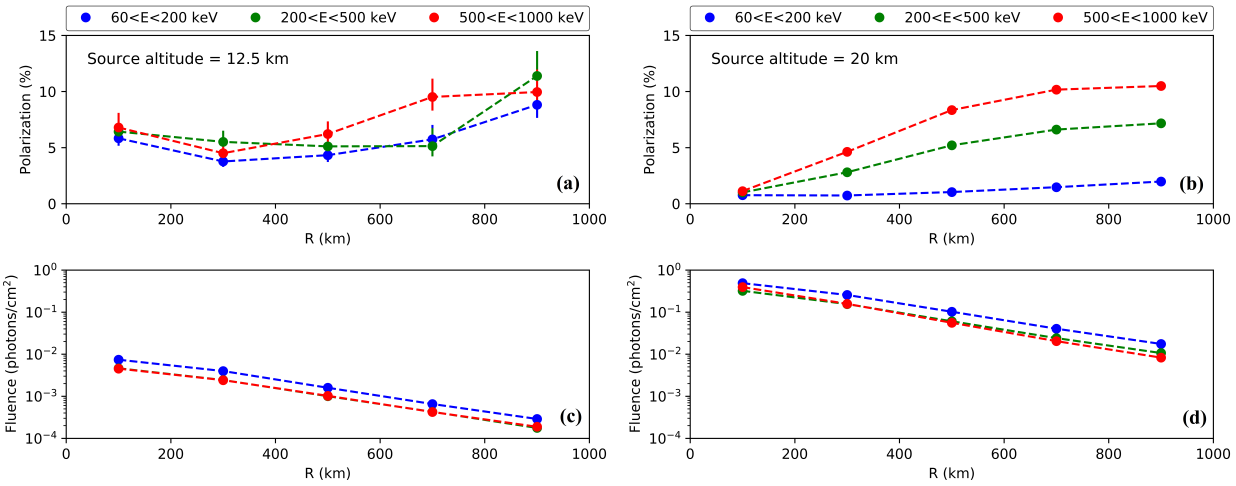

Figure 3.1: Degree of linear polarization (top) and expected fluence of gamma rays (bottom) detected by a polarimeter at low-Earth orbit with source altitude at 12.5 km (left) and 20 km (right). Because only a few tens of counts are typically detected by spacecraft in low-Earth orbit from TGFs, detecting this level of polarization is unlikely.

The column depth, which is the amount of atmosphere between the source altitude and spacecraft altitude, is a key parameter in the propagation of gamma rays which is directly related to the average number of Compton scatters. It has a value of 200.9 and 60.7 g/cm^2 for the source altitudes of 12.5 and 20 km. As gamma rays propagate towards low-Earth orbit and the number of scatters increases, their average energy shifts towards the lower end of the spectra. The average number of Compton scatterings for gamma rays originating from mid-altitude (high-altitude) TGFs ranges from 3 to 8 (1 to 6) for the highest to lowest energy band, respectively. Our analysis of polarization level versus number of Compton scatterings showed that gamma rays with single Compton scattering arriving at low-Earth orbit have the highest degree of polarization (20 – 25%), which are often at highest energy bands. Consequently, gamma rays with multiple Compton scatterings produce a higher level of polarization at lower energy bands.

For a mid-altitude source TGF, a similar value of polarization is observed in all energy bands, with the maximum polarization being about 10% (see Figure 3.1a), however for high-altitude source TGF, a maximum polarization of 10% is observed at the highest energy band and it gradually drops to 1% at the lowest energy band (see Figure 3.1b). This difference is caused by the fact that high-altitude source TGFs are propagating through 3 times less amount of atmosphere, so

the Compton scattered gamma rays are relatively at higher energy bands compared to mid-latitude source TGFs. The linear polarization near the z-axis (R < 200 km) is typically minimum due to cylindrical symmetry and it increases directly with off-axis distance. In principle, even though the TGF is directed upward at the source, the polarized gamma rays could be observed up to 1000 km away in space given a large enough detector.

Assuming that a TGF produces about 10^{17} photons at the source, the typical fluence of gamma rays seen by spacecrafts at low-Earth orbit ranges from 0.1 – 1 photons/cm^2 (based on source altitude) over the full energy range. The fluence right above the source has its maximum value and it decreases with increasing off-axis distance for both source altitudes. For mid-altitude source, a fluence range of 10^{-2} (at nadir point) to 10^{-4} (at R = 900 km) photons/cm^2 is calculated (see Figure 3.1c). Given that in our calculation gamma rays' population is narrowed down to specific energy bands, the actual observed fluence by spacecraft in low-Earth orbit could be up to one order of magnitude larger. Furthermore, gamma rays originating from high-altitude TGFs have an average fluence of 0.5 (nadir point) to 0.01 (at R = 900 km) photons/cm^2 (see Figure 3.1d). Based on these numbers, to measure a significant level of polarization (e.g. 10%), the spacecraft needs to be in the regions with large off-axis distance from the nadir point ($\sim R \geq$ 500 km), where the fluence from TGFs is about 5 to 6 orders of magnitude less than required fluence for polarimetry experiments ($\sim$ 9200 photons/cm^2). Then, to have a reliable measurement of TGFs at space, a very large effective area is required which is not likely to occur for the foreseeable future, so the idea of polarimetry of TGFs by spacecrafts in the low-Earth orbit is not likely to be fruitful.

3.3.2 Polarization of TGFs Near the Ground

3.3.2.1 Polarization of low-altitude TGFs near the ground

Hare et al. [2016] reported a ground measurement of a TGF occurring in coincidence with an altitude-triggered lightning at the International Center for Lightning Research and Testing (ICLRT) in Florida. Observations suggests that the upward positive leader of the triggered lightning flash had induced RREAs when the leader tip reached an altitude of 3.5 km, resulting in the observed

TGF. In this section, we discuss the simulation of a downward TGF beam starting at 3.5 km. There are 4 consecutive horizontal detection planes in the simulation at altitudes of 3 km, 2 km, 1 km and on the ground. The collected photons in each plane are separated in annular bins and categorized in three energy bands to calculate the polarization and expected fluence of gamma rays versus radial distance up to 1 km away (see Figure 3.2).

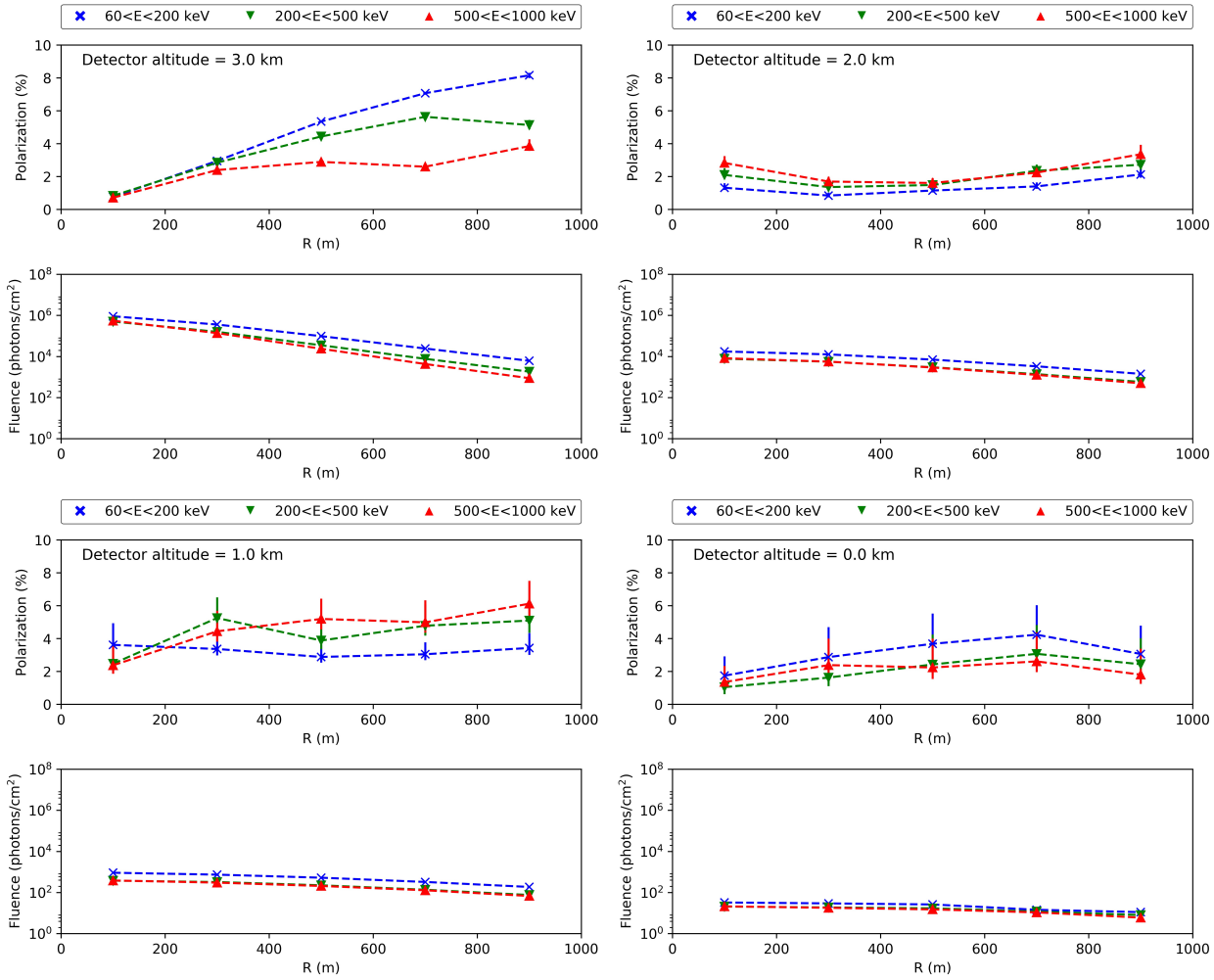

Figure 3.2: Degree of linear polarization and expected fluence of gamma rays propagated downward at 3.5 km and detected at altitudes of a) 3 km, b) 2 km, c) 1 km and d) on the ground. Maximum degree of polarization ($\sim$ 8%) is found near the source region from low-energy band gamma rays. Degree of polarization decreases at lower altitudes and eventually reaches to zero on the ground.

For the detector near the source region (h = 3 km, see Figure 3.2a), a maximum degree of 8% and 3% polarization is calculated at the lowest and highest energy bands. Since the beaming of

TGF was narrow at the source, a significant fluence of gamma rays was not expected at large radial distances in this altitude. So, if any gamma-ray would be detected in this region, it would surely have some degree of polarization due to being produced by bremsstrahlung emission, or Compton scattered at large angles with respect to the electric field lines. With the detector at lower altitudes, the average polarization in all energy bands decreases (see Figure 3.2b,c) and eventually reaches to zero on the ground (see Figure 3.2d). Due to the large column depth between the source and detection planes near the ground, polarization information is nearly completely washed out after multiple Compton scatterings. In addition, gamma rays with multiple scatters and lower energies could be absorbed by photoelectric absorption before they reach to ground. As seen in Figure 3.2, the fluence of gamma rays in all of energy bands drop exponentially with increasing off-axis distance from the source, with most photons located near the z-axis and directed downward. As the detection altitude decreases, a more uniform spatial distribution of photons around the z-axis forms which is due to widening the width of TGF beam and deflection of gamma rays by scattering. Altogether, even though about 8% polarization degree is anticipated for such events at lower energy bands (see Figure 3.2a), measuring such level of polarization requires the detector to be very close to source region (less than 500 m), so the fluence would be near or above the required level for a polarimetry measurement with 99% confidence level. This suggests that measuring the polarization of low-altitude TGFs would be possible from a mountain or using balloon-borne instruments, if the balloon payload gets close enough to source region during the event, otherwise it will not be likely.

3.3.2.2 Source of polarization for low-altitude TGFs near the ground

The bremsstrahlung emission and Compton scattering both produce some degree of polarization. In this section, we have categorized the same population of gamma rays as previous section, without any constraint on energy, based on the number of Compton scatterings they have had. Bremsstrahlung polarization is calculated from the photons that are produced directly from bremsstrahlung emission without any scattering, while Compton polarization is calculated from

photons with the number of Compton scatters greater or equal to 1. The degree of linear polarization and fluence of gamma rays at four detection planes are presented in Figure 3.3.

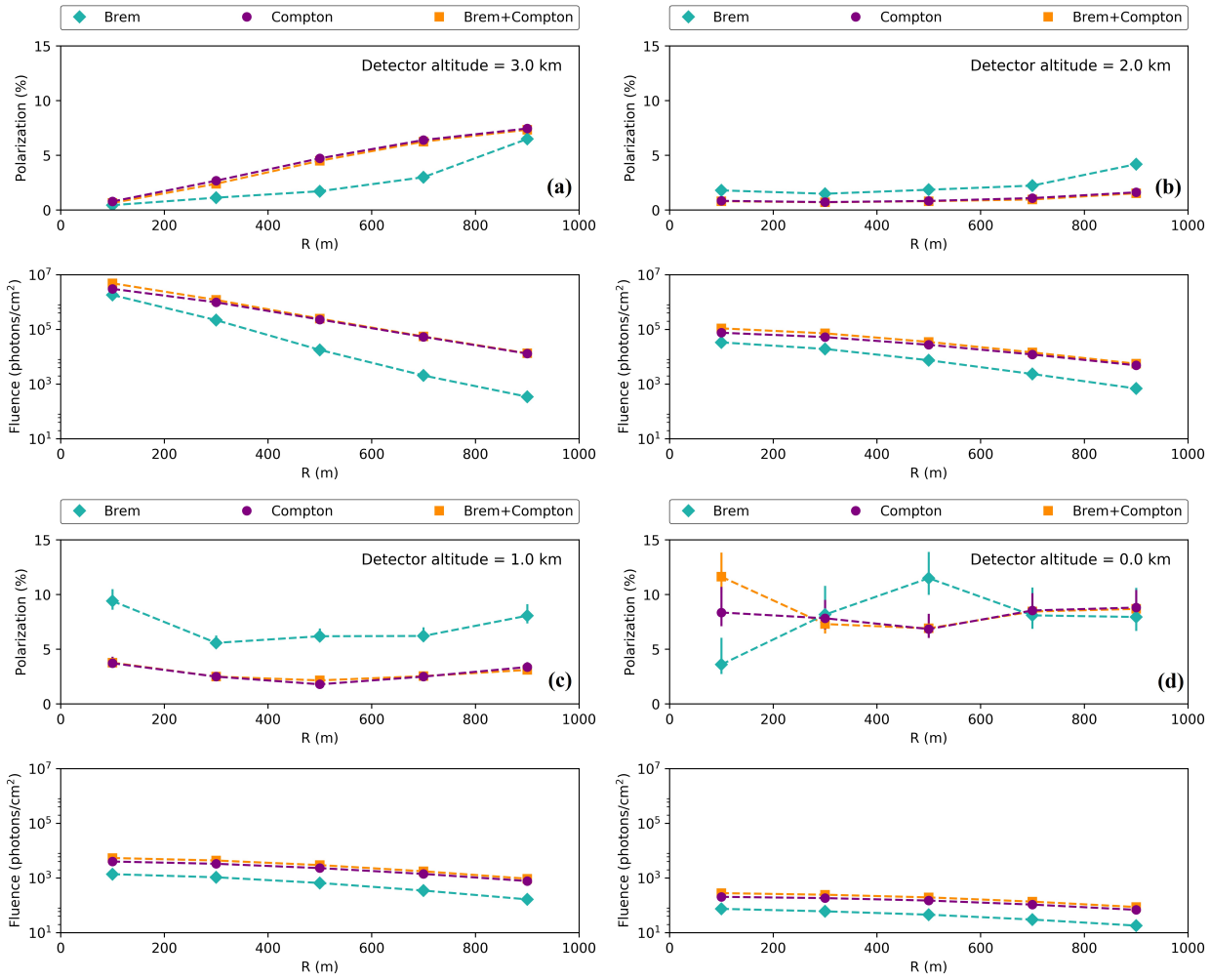

Figure 3.3: Degree of partial linear polarization and expected fluence of gamma rays initiated downward at 3.5 km and detected at altitudes of a) 3 km, b) 2 km, c) 1 km and d) on the ground. "Brem" represents the gamma rays with zero number of Compton scatterings which are directly produced by bremsstrahlung radiation and "Compton" refers to the gamma rays with one or greater number of Compton scattering.

Near the source region (1^{st} detection plane, see Figure 3.3a), polarization from Compton scattering is the dominant process with about 7% polarization. This is comparable with the polarization seen earlier at the lower energy bands (see Figure 3.2a, 60 – 200 keV and 200 – 500 keV bands), which suggests Compton scattering as the dominant polarizing source at these energy levels as well. Bremsstrahlung emission also shows some level of polarization around the z-axis ($\sim$ 4%),

but its fluence drops significantly with off-axis distance. Since these gamma rays are produced by bremsstrahlung emission of runaway electrons, this level of bremsstrahlung polarization may be thought of as the intrinsic polarization of gamma rays at the source. As the detection altitude decreases (2^{nd} and 3^{rd} detection plane, see Figure 3.3b,c), polarization from Compton scattering attenuates which is due to multiple scatters washing out the polarization information. In addition, since the Compton scattered gamma rays lose their energy in a sequence of scatterings, they would be partially absorbed by photoelectric absorption after hundreds of meters, which also reduces the degree of Compton polarization. On the other hand, bremsstrahlung polarization (from gamma rays with no scatter) would be enhanced relatively at all distances with about 7% polarization at 3^{rd} detection plane (see Figure 3.3c). The bremsstrahlung gamma rays that have reached the 3^{rd} detection plane might have one or more Compton scattering along their path towards the ground (between the 3^{rd} and 4^{th} detection plane), so their source of polarization would be counted as Compton scattering. This could be seen from the 4^{th} detection plane result (see Figure 3.3d, on the ground), where the bremsstrahlung and Compton scattering are the source of polarization simultaneously.

The fluence of bremsstrahlung gamma rays is relatively small in comparison to Compton scattered gamma rays, so even if there are some level of bremsstrahlung polarization, that would not have a significant effect on the total polarization (Brem + Compton) calculated at detection planes. As discussed in Section 3.3.2, the polarization level from low-altitude TGFs seen on the ground is almost zero for energies between 60 keV to 1 MeV (see Figure 3.2d), so the average 10% polarization from Compton scattering or bremsstrahlung seen in Figure 3.3d is associated with gamma rays with energies above 1 MeV. These are the gamma rays that have travelled all the way from the source to the ground with minimum number of Compton scatterings and come from the upper end of energy spectrum. Energetic radiations produced during a TGF event have energies from hundreds of keV up to tens of MeV. The Hardness Ratio (HR), which is an approximate measure of the spectral shape based on the count rates at low and high energies, is given by Equation 3.13.

$$Hardness\ Ratio = \frac{number\ of\ photons\ with\ (1\ MeV < E < 100\ MeV)}{number\ of\ photons\ with\ (100\ keV < E < 1\ MeV)} \tag{3.13}$$

The hardness ratio of gamma rays passing through 7 detection planes, each separated by 0.5 km from each other, versus radial distance is shown in Figure 3.4. Below the source at the 1^{st} detection plane (h = 3 km, R = 100 m), hardness ratio has a maximum of 1.7, dropping exponentially to 0.2 at R = 900 m. As the detector altitude decreases, its value increases to a maximum of 3.9 on the ground. This is because energetic gamma rays have a higher chance of traveling through the atmosphere without being scattered or absorbed by photoelectric effect, so as they propagate towards the ground, the relative size of the population of MeV range gamma rays increases. As dis-

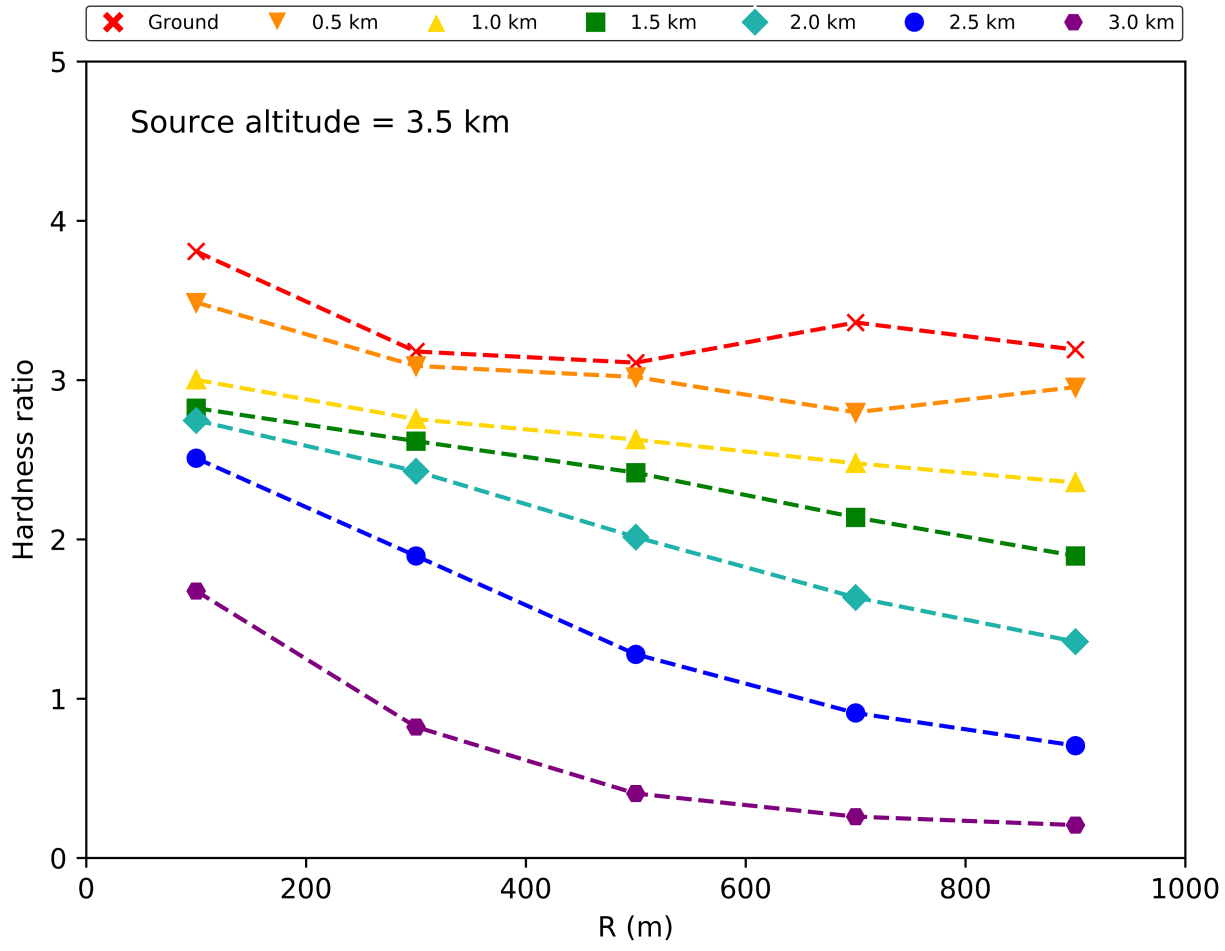

Figure 3.4: Hardness ratio of the gamma rays at 7 consecutive horizontal planes from 3 km to the ground, with source of gamma-ray 3.5 km. Note the increase in the average hardness ratio of gamma rays, as they propagate downward.

cussed earlier, most of these energetic gamma rays are produced directly from the bremsstrahlung radiation of runaway electrons and carry some degree of intrinsic polarization with themselves (see Figure 3.3c,d), so as their relative population increases (larger HR), they would have more contribution in the polarization calculation. This means that the primary source of polarization for low-altitude TGFs near the ground could be both energetic gamma rays from bremsstrahlung and Compton scattered gamma rays with lowest number of scatterings.

3.3.3 Polarization of Ground-Level TGFs and X-Rays

The degree of linear polarization is a helpful parameter that can be used to have a better understanding of the source geometry. There remains uncertainty about the width of the angular distribution of TGFs and X-rays at the source. This uncertainty affects the estimates of global frequency of TGFs since narrow beams of photons are less likely to be detected by spacecrafts and need a higher global frequency to be consistent with its current rate of detection *[Carlson et al., 2011]*. The beaming of the TGF also provides information about the source region, since the divergence of TGF beam is related to the spatial structure of electric field *[Carlson et al., 2009; Collier et al., 2011]*. Depending on the beaming of TGFs at the source, different degrees of polarization could be expected at spacecraft altitudes, however as mentioned earlier, measuring such level of polarization could be challenging due to the low fluence of polarized gamma rays in space. Since several ground-level measurements of TGFs and X-rays from natural and rocket-triggered lightning have been reported recently, polarimetry of these events seems to be a solution for the mentioned challenges. In the following sections, we will discuss the possibility of measuring the polarization of these events on the ground and try to correlate the beaming of the source to polarization information.

3.3.3.1 Polarization of X-rays from rocket-triggered lightning

In this section, we have simulated the X-ray emission from rocket-triggered lightning and calculated the polarization of the X-rays on the ground. To do so, runaway electrons with differential energy spectrum of $dN_e/dk \propto exp(-k/k_0)$ are propagated through air, where k is the kinetic en-

ergy of electrons and K_0 is set to 1 MeV. The ambient electric field was set to zero and the resulting photons are collected at the end of avalanche region. These photons are propagated downward from 100 m above the ground with beam width (θ) of 0° (vertical), 30°, 60° and 90° (isotropic) degrees with respect to z-axis and collected in the horizontal detection plane on the ground. The linear polarization and fluence of X-rays versus radial distances up to 1 km away are shown in Figure 3.5. The average luminosity of X-rays at the source during rocket-triggered lightning is reported to be about 2×10^{15} photons/second for source altitude of 100 m *[Saleh et al., 2009]*, so for a typical

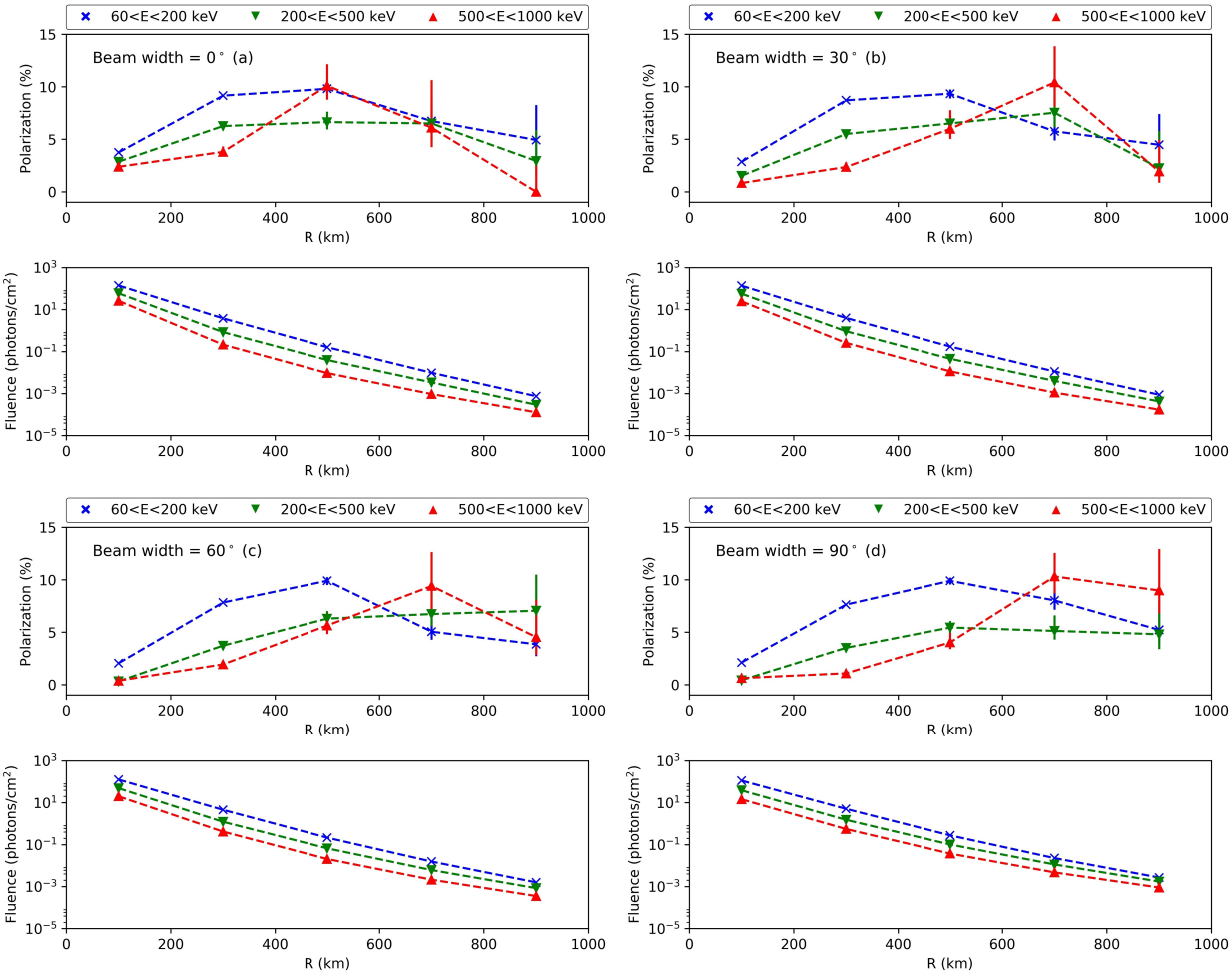

Figure 3.5: Degree of linear polarization and expected fluence of X-rays from rocket-triggered lightning, initiated downward 100 m above the ground and detected on the ground with the beam width of a) 0° (vertical), b) 30°, c) 60°, and d) 90° (isotropic).

X-ray emission with tens of microseconds duration, about 10^{12} X-rays are produced at the source. This number is used here to calculate the fluence of X-rays on the ground.

For narrow beam of X-rays (θ = 0°), an average polarization degree of 5 – 10% is calculated (see Figure 3.5a), where the most of polarization is observed at the low and medium energy bands (60 – 500 keV). This is because the energy spectrum of X-ray bursts from a lightning strike near the ground is much softer than RREA. The X-ray bursts during these events are probably produced from thermal runaway electrons accelerated in the large electric fields from the leader tip. This could also be seen from Figure 3.5, where the fluence of X-rays for low energy photons (60 – 200 keV) is at least one order of magnitude larger than other energy bands. As the width of X-ray beam increases, similar levels of polarization and behavior are observed at wider beams (see Figure 3.5b,c,d), which implies no direct evidence of a relationship between width of X-ray beam and polarization level. Since X-ray emissions from lightning are more likely to be produced from isotropic source rather than a vertically downward beam *[Schaal et al., 2013]*, then polarization result on Figure 3.5d would be closer to any possible measurement of these events. The fluence of X-ray bursts for all energy bands near the z-axis (R < 200 m) is about 10^2 photons/cm^2, and it decreases rapidly by a factor of 10^6 in less than a kilometer. For an isotropic source, the average polarization reaches its maximum at about 500 m from z-axis, where the fluence is about 0.1 photons/cm^2. This is approximately 10^5 orders of magnitude less than required level of fluence, so measuring polarization of X-ray bursts from lightning on the ground does not seem to provide detailed insight into the beam geometry of the source and it does not seem feasible due to low fluence of X-rays.

3.3.3.2 Polarization of very low-altitude ground-level TGFs

So far, there have been five reports of detection of ground-level TGFs associated with natural *[Dwyer et al., 2012; Tran et al., 2015; Enoto et al., 2017]* and rocket-triggered *[Dwyer, 2004; Hare et al., 2016]* lightning. Four of these events have been detected in the state of Florida, United States; and the fifth and most recent one is observed along the coast of the Sea of Japan. Depending

on the source altitude, attenuation by atmosphere can affect the polarization measurement of TGF events significantly. Very low-altitude ground-level TGFs are frequently occurring during winter thunderstorms along the coast of the Sea of Japan, where cold temperature brings the cloud-base down to a few hundreds of meters above the ground *[Enoto et al., 2017]*. Gamma rays from such TGF events tend to have a higher chance reaching the ground, which could potentially make their polarimetry easier to observe. Here, we have simulated the propagation of downward ground-level TGFs from 100 m above the ground with the beam width (θ) of 0° (vertical), 30°, 60° and 90° (isotropic) degrees with respect to z-axis and calculated the polarization on the ground (see Figure 3.6).

The maximum degree of polarization ($\sim 12\%$) is calculated at the lowest energy band for all beam widths, and it decreases to as low as 5% at the highest energy band. Low energy gamma rays ($E <$ 200 keV) seen on the ground could be the result of multiple Compton scatters at small angles or single Compton scatter at large angles. Our analysis showed 8 – 10% and 20 – 25% polarization degree for the former and latter cases, however high energy gamma rays ($E >$ 500 keV) showed a maximum polarization degree of 5% and 10%, respectively. Since the energy spectra of TGFs are described by the RREA mechanism with an average energy of 7.3 MeV *[Dwyer, 2003; Dwyer et al., 2006]* measuring a high degree of polarization would be accompanied by a softer energy spectrum compared to the RREA spectrum. This is because Compton scattering which is the dominant source of polarization reduces the average energy of photons seen by detectors on the ground. For a downward vertical beam ($\theta = 0°$), polarization peaks at about 500 m from the z-axis (see Figure 3.6a), while this distance increases as the beam broadens (see Figure 3.6b,c), in a way that polarization peaks at about 900 m for an isotropic source ($\theta = 90°$, see Figure 3.6d). As a result, the broader the initial beam width of TGF is, the farther from the z-axis the polarization peaks. This could also be another confirmation that Compton scattering is the primary source of polarization for such events.

For a downward vertical beam, the expected fluence ranges from 10^7 photons/cm^2 (near the z-axis) to 10^2 photons/cm^2 (1 km away). At R = 500 m, where the polarization degree is maximum,

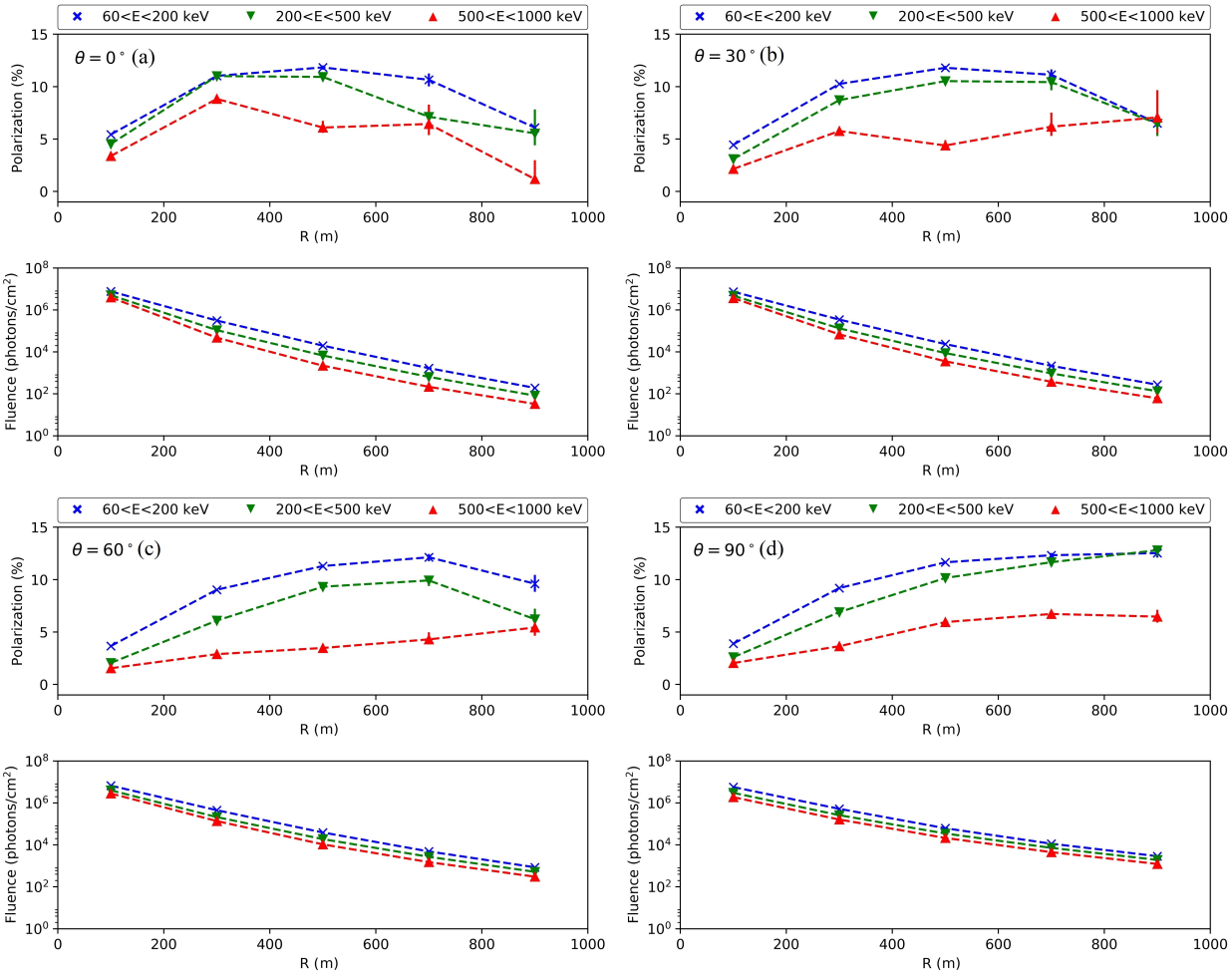

Figure 3.6: Degree of linear polarization and expected fluence of ground-level TGFs, initiated downward 100 m above the ground with the beam width of a) 0° (vertical), b) 30°, c) 60° and d) 90° (isotropic). Note that as the beam width broadens, degree of polarization peaks at farther distances from the z-axis.

fluence is about 10^4 photons/cm^2 which is large enough (compared to 9200 photons/cm^2 threshold) for polarimetry of these ground-level TGFs at 99% confidence level (see Figure 3.6a). As mentioned earlier, location of polarization peak moves further away from z-axis while the beam is broadening, so one might think that polarimetry of wider beams should be more challenging. However, a broader beam is accompanied by a higher fluence at larger distances from z-axis compared to vertical beam situation. This could be seen from Figure 3.6d, where fluence at 1 km away is about 6×10^3 photons/cm^2 which is comparable to required polarimetry fluence. Altogether, it seems that difficulties with the polarimetry of TGFs observed in space due to low fluence would

not be an issue for very low-altitude ground-level TGFs, given that the source of TGF is close to ground. This is because gamma rays can reach the ground with minimum attenuation rate compared to low-altitude TGFs which makes the polarimetry of these very low-altitude ground-level TGFs feasible.

3.4 Conclusion

Terrestrial Gamma-ray Flashes (TGFs) are enormous bursts of energetic radiation produced by relativistic runaway electrons avalanche (RREA) inside or above thunderclouds. Although, these radiations have been investigated widely since their discovery, there has been no study of their polarization so far. We have modified REAM (Runaway Electron Avalanche Model) to calculate the linear polarization of gamma rays for in space and near the ground observations. We found that the gamma rays from mid-altitude (12.5 km) and high-altitude (20 km) TGFs, detected in the low-Earth orbit, could be polarized up to 10%, but too few counts of photons would be observed in most cases, which makes polarimetry of these events non-feasible in the near future. In addition, polarization of low-altitude TGFs, initiated downward at 3.5 km, was calculated at multiple horizontal planes for three energy bands below 1 MeV. The results showed that the polarization reaches its maximum value (8%) near the source region (0.5 km below the source) at the lowest energy band (60 – 200 keV) and eventually drops to zero near the ground. Partial polarization of these events with no constraints on energy band showed that Compton scattering was the dominant process in polarizing the gamma rays near the source region, while MeV range photons produced directly from bremsstrahlung emission had some comparable level of polarization on the ground. Furthermore, very low-altitude ground-level TGFs and X-rays produced during rocket-triggered lightning had a maximum polarization degree of 13% on the ground, where most of it was associated with low-energy bands (60 – 500 keV). Polarimetry of X-rays seemed to be challenging due to low fluence, however very low-altitude ground-level TGFs produced enough number of gamma rays to reach the ground and make their polarimetry feasible. For these events, polarization versus

beam width showed that as the initial beam of gamma rays broadens, the polarization reaches its maximum at larger distances from the z-axis. In overall, it seems polarimetry of very low-altitude ground-level TGFs from lightning is the only scenario that can practically be measured, and such events could be detected during winter thunderstorms along the coast of the Sea of Japan.

CHAPTER 4

TEMPORAL AND SPECTRAL DISTRIBUTION OF TGFS

4.1 Introduction

TGFs are submillisecond bursts of energetic gamma rays produced by bremsstrahlung emission of runaway electrons, often observed by spacecraft in low-Earth orbit. Temporal properties of TGFs can be used to discriminate between models of the origin of TGFs and provide some basic physical properties of the TGF processes *[Fishman et al., 2011]*. These properties have changed significantly over time with improved instruments and enhanced modelings. Currently, there are two well-known models which try to explain the generation of TGFs: Relativistic Feedback Discharge (RFD) *[Dwyer, 2008; Dwyer et al., 2012]* and Lightning Leader theory *[Moss et al., 2006; Celestin and Pasko, 2011]*. RREA-based mechanisms have provided a very good agreement with the observed duration of TGFs in space *[Fitzpatrick et al., 2014]*, while the measured timescale associated with the stepping of lightning leaders are reported to be in order of several tens of nanoseconds *[Howard et al., 2011]*. Then, if TGFs are produced by such mechanisms, it is expected that their duration would be in the same order of magnitude *[Celestin and Pasko, 2012]*. However, measurement of TGFs made by spacecrafts shows durations significantly longer than predicted by the existing lightning leader models which raises this question: what is the actual timescale of TGFs at the source and what processes cause its duration to be prolonged?

In order to properly observe TGFs, gamma-ray detectors need to have fast timing and immunity to deadtime and pulse pileup, and good detection efficiency for the high-energy photons *[Fishman et al., 2011]*. Deadtime occurs when two consecutive photons enter a detector within a time interval shorter than the detector's response time which leads to the rejection of the second event. In addition, deadtime tends to lengthen the duration of each pulse. The total deadtime of a gamma-

ray detector is the aggregate deadtime of scintillator, pulse processing (e.g., pulse shaping and amplifiers) and data acquisition (e.g., ADC or counters) *[Knoll, 2010]*. Given that the brightest part of the TGF is normally the hardest *[Grefenstette et al., 2008]*, deadtime would make the TGF spectrum look like softer than the true spectrum. Pileup occurs when two photons enter the detector very close in time and their energy is summed into one count, resulting in a harder observed spectrum. Overall, deadtime can cause an underestimation of the higher energy part of energy spectrum and pulse pileup results in an overestimation of the higher energy part.

The duration of TGF events is usually calculated based upon two common definitions called t50 and t90. The t50 (t90) value is the duration of the central interval in which 50% (90%) of the counts are accumulated, with 25% (5%) of the counts occurring before and after the interval *[Briggs et al., 2010; Fishman et al., 2011]*. Given that the low number of counts in the leading and trailing 5% of the total counts of many pulses leads to large statistical uncertainties, many TGFs observed in space have unusually high t90 values compared to the t50 values. However, t50 is less susceptible to uncertainties caused by low count rates and background *[Fitzpatrick et al., 2014]*.

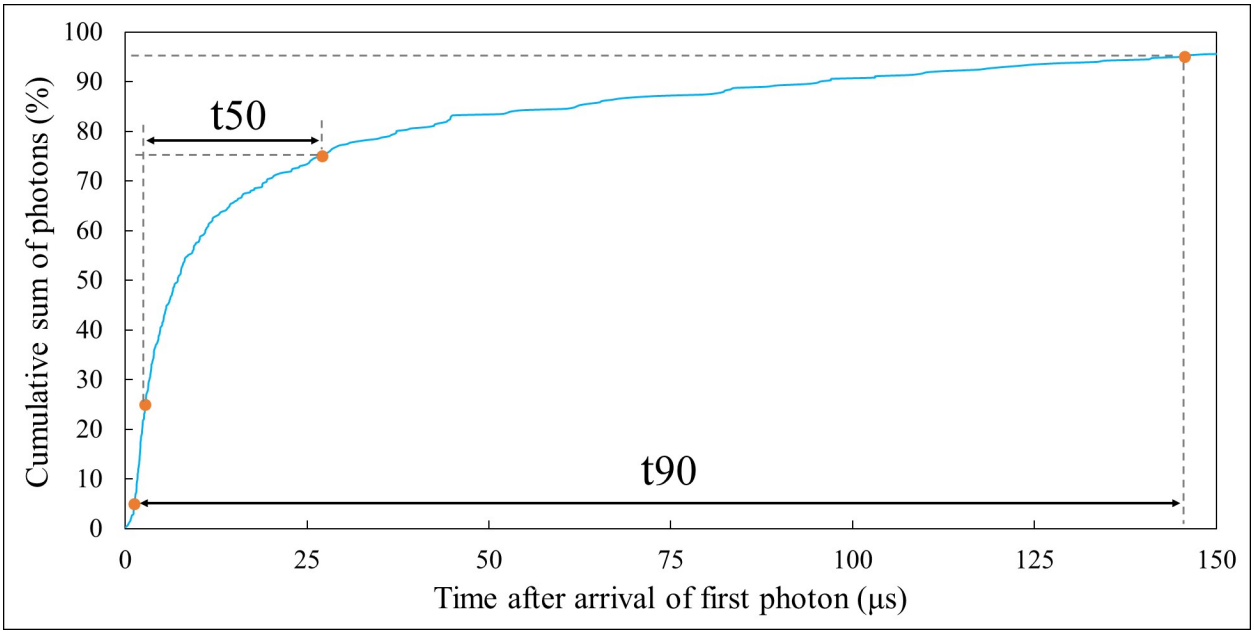

Figure 4.1: Cumulative sum of photons versus time of arrival. The TGF source is at 12.5 km and detector is located at altitude of 500 km with an off-axis distance of 250 km. Note that the orange dots represent the times at which cumulative sum of photons reaches 5%, 25%, 75% and 95%, respectively. Two arrows represent the t50 and t90 values. The source duration was instantaneous.

As an example, Figure 4.1 shows the simulated time evolution of the cumulative sum of photons at 500 km altitude with the TGF source altitude at 12.5 km and detector located at an off-axis distance of 250 km. The calculated t50 and t90 durations are about 24 μs and 145 μs, respectively. It is quite obvious that t90 significantly overestimates the duration of TGFs due to trailing counts. Based upon these evidences, we have used t50 definition to describe the duration of TGFs in this chapter. In general, the total duration of a TGF event could be estimated as twice of the t50 value.

4.2 Recent Temporal Observation of TGFs

The timescale of TGFs was first reported to be in the order of a few milliseconds from BATSE measurements *[Fishman et al., 1994]*. However, it was found later that BATSE data was suffering from significant dead time due to high-intensity flux and long trigger window which caused longer pulses to be over sampled *[Grefenstette et al., 2008; Gjesteland et al., 2010]* and these events were much shorter than thought. One effect of dead time on BATSE data was measuring a significantly softer energy spectrum leading to a higher estimate of TGF source altitude. In addition, an average delay of about 100 μs was observed between the arrival of high energy and low energy photons which was explained by Compton scattering of photons in the atmosphere *[Grefenstette et al., 2008]*. Further measurements performed by the RHESSI spacecraft and corrected for the deadtime revealed that TGFs duration could be as low as several hundreds of microseconds ($\sim$ 300 μs) with a delay of about 28 μs between low and high energy photons *[Smith et al., 2010; Gjesteland et al., 2010]*. However, these findings did not last long, and observations made by Fermi revealed that TGFs pulses could be as brief as 50 μs *[Fishman et al., 2011]*. Note that the primary goal of GBM was the study of Gamma Ray Bursts and was not optimized for the TGFs, so several instrumental factors such as dead time, pulse pileup, and detection efficiency were taken into account later to estimate the true number of counts observed by the detector. The nominal dead time of GBM per detected count has been reported to be 2.6 μs. However, this value increases to 10.4 μs for energetic events registered by BGO detectors *[Meegan et al., 2009]*. So, even measurements made by the

Gamma-ray Burst Monitor (GBM) instrument have been suffering from deadtime and 50 µs may be an overestimated value for the duration of TGFs. A comparison of REAM simulation with GBM data for various source electrons have suggested that the temporal distribution of TGFs observed by GBM vary on timescales of tens of microseconds with an upper limit of 100 μs *[Fitzpatrick et al., 2014]*.

Marisaldi et al. [2015] reported a catalog of 306 TGF events detected by the MCAL instrument onboard AGILE spacecraft with the temporal distribution showing a median of 290 μs and average of 370 μs. This was remarkably larger than Fermi measurements by a factor of 2.6, mostly due to the deadtime induced by the AntiCoincidence (AC) shield. After disabling the AC shield in March 2015, the second TGF catalog of MCAL was reported by *Marisaldi et al. [2015]* containing 270 TGFs with a median of 86 μs, where about one third of events had durations less than 50 μs indicating that enhanced configuration had made the detection of shorter events possible. However, it was found later pileup effects on the MCAL instrument had limited the observation of high fluence, short duration TGFs. Basically, MCAL has not been able to observe TGF events with fluence above 0.1 photons/cm^2 and durations less than 20 μs.

4.3 Simulation Details

Energetic seed electrons are accelerated inside an avalanche region with a sea-level equivalent electric field of 400 kV/m and collected at the end of region. Then, resulting TGFs are propagated upward with an instantaneous electron source, at three source altitudes of 12.5, 15 and 20 km and eight beam geometries including conical beams with half angles of 0°, 30°, 45°, 60°, 90° and tilted beams at 30°, 45° and 60° with respect to z-axis. Note that the polar angle of the tilted beams were set to the desired value, however the azimuthal angle was produced by a uniform random generator. This made the gamma rays distribution at the source a hollow cone which might be slightly different from actual tilted beams, but it was done to make the spatial comparison of durations more symmetrical and less cmplicated. The photon distribution at spacecraft altitude (500 km)

is integrated into concentric annuli of diameter 50 km. Photons reaching each annulus are sorted based on the time of arrival relative to the first photon. Note that the middle of each annulus was chosen as the reference point and the time of arrival of photons reaching around that were adjusted accordingly. Given that gamma rays propagate with speed of light, the adjustment were about 2 order of magnitudes smaller than t50 values.

4.4 Results and Discussion

4.4.1 Spectral Properties of TGFs

Hardness Ratio is an approximate measure of the spectral shape based on the count rates at low and high energies. In this chapter, it is calculated by the number of photons with energy greater than 300 keV divided by the number of photons with energy less than 300 keV. This definition is slightly different from the one we used in the Chapter 3 (Equation 3.13), however it was chosen to make the comparison of our results with *Fitzpatrick et al. [2014]* more reliable. Figure 4.2 shows the hardness ratio calculated for the dataset previously described including various beam geometries and source altitudes. Near the nadir point, a very hard energy spectrum is expected to be seen from vertical beams for all source altitudes. This is because most of the photons reaching this region are coming directly from the source with a minimum number of scatterings which results in a very hard spectrum. As the beam broadens, the energy spectrum becomes softer due to arrival of originally-tilted gamma rays that are Compton scattered towards the nadir point. As the off-axis distance increases, the energy spectrum softens due to increased Compton scattering experienced by the photons as they propagate through a greater integrated density of atmosphere, agreeing with earlier observations *[Fitzpatrick et al., 2014; Hazelton et al., 2009]*. In addition, approximately similar hardness ratios are seen for all beam widths at distances above 200 km. It has been suggested that TGFs with harder spectra could be explained by a higher source altitude in general, as the photons will undergo less Compton scattering due to the reduced column depth *[Fitzpatrick et al., 2014]*, however our results indicate that this statement is not completely true

near the nadir point as shown by Figure 4.2. In fact, the lower the source altitude is, the harder the energy spectrum would be at distances less than 200 km. This is probably because for the lower source altitudes, a larger percentage of low-energy photons ($E < 300$ keV) would be absorbed by the atmosphere, so a very hard spectrum would be expected.

Figure 4.3 (left panel) shows the fluence of gamma rays for the same dataset of TGFs versus off-axis distance. In general, the gamma-ray fluence drops with increasing the off-axis distance and decreasing source altitude. The former is due to the deflection of gamma rays from z-axis by Compton scattering which can reduce the fluence up to almost 2 orders of magnitude at 500 km off-axis distance. This reduction can affect the measurement of temporal properties of TGFs by spacecrafts as it is reported by *Fitzpatrick et al. [2014]*. Their results show a reduction in the duration of TGFs with increasing the off-axis distance. This is particularly due to lack of enough counts at larger distances, since it gets more difficult to distinguish between the background and TGFs which leads to a shorter duration. Then, temporal properties of TGFs should be interpreted very carefully in these cases as there are several factors affecting these measurements. The latter is because the lower the source altitude is, the higher the number of scatterings and photoelectric absorptions would be, which reduces the chance of gamma rays for escaping from the atmosphere. Up to 200 km off-axis distance, vertical beams have the highest fluence for all source altitudes and as the off-axis distance increases, similar level of fluence is observed for conical beam with half angles up to 60°. The tilted beams have relatively lower gamma-ray fluence compared to conical beams, since part of the scattered gamma rays from these beam geometries reach beyond 500 km off-axis distance, as they arrive at the low-earth orbit.

Figure 4.3 (right panel) shows the energy spectrum of the same dataset of TGFs calculated at 250 – 300 km away from the z-axis. This area was chosen since it is believed that most of TGFs detected by Fermi have occurred within 300 km of the spacecraft *[Fitzpatrick et al., 2014]*. Above a few hundred keV, the exponential behavior of spectrum is visible which matches with the RREA spectrum as given by the Equation 1.3. As the source altitude increases, the photon density per unit energy drops faster at higher energies which can lead to a softer energy spectrum. This agrees

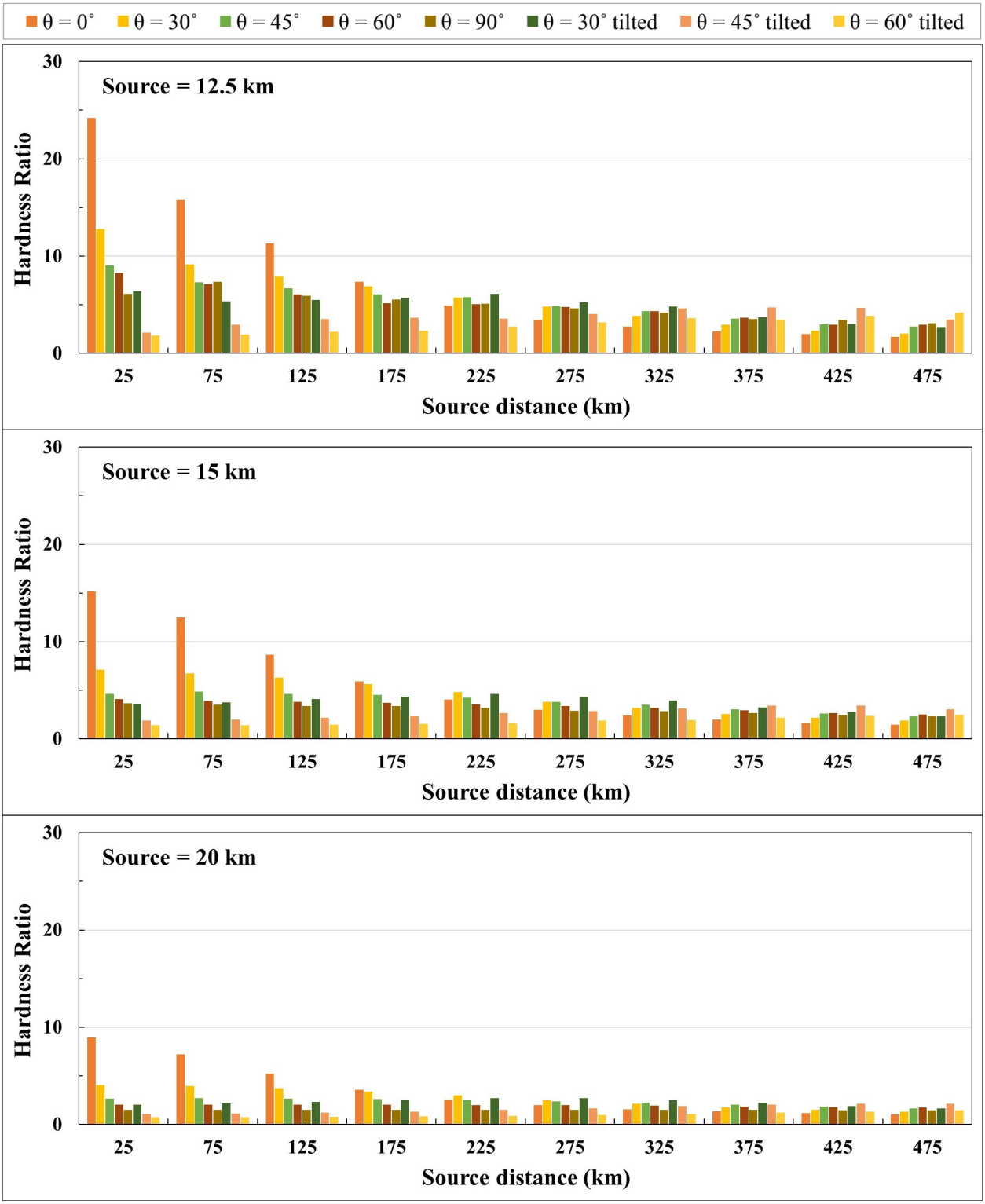

Figure 4.2: Hardness ratio versus distance between the subsatellite point and TGF source for three source altitudes at 12.5 km (top), 15 km (middle) and 20 km (bottom) with a cutoff energy of 300 keV. In total, 8 beam widths are simulated including cones with 0°, 30°, 45°, 60° and 90° uniform distribution and tilted beams with 30°, 45° and 60° direction with respect to z-axis.

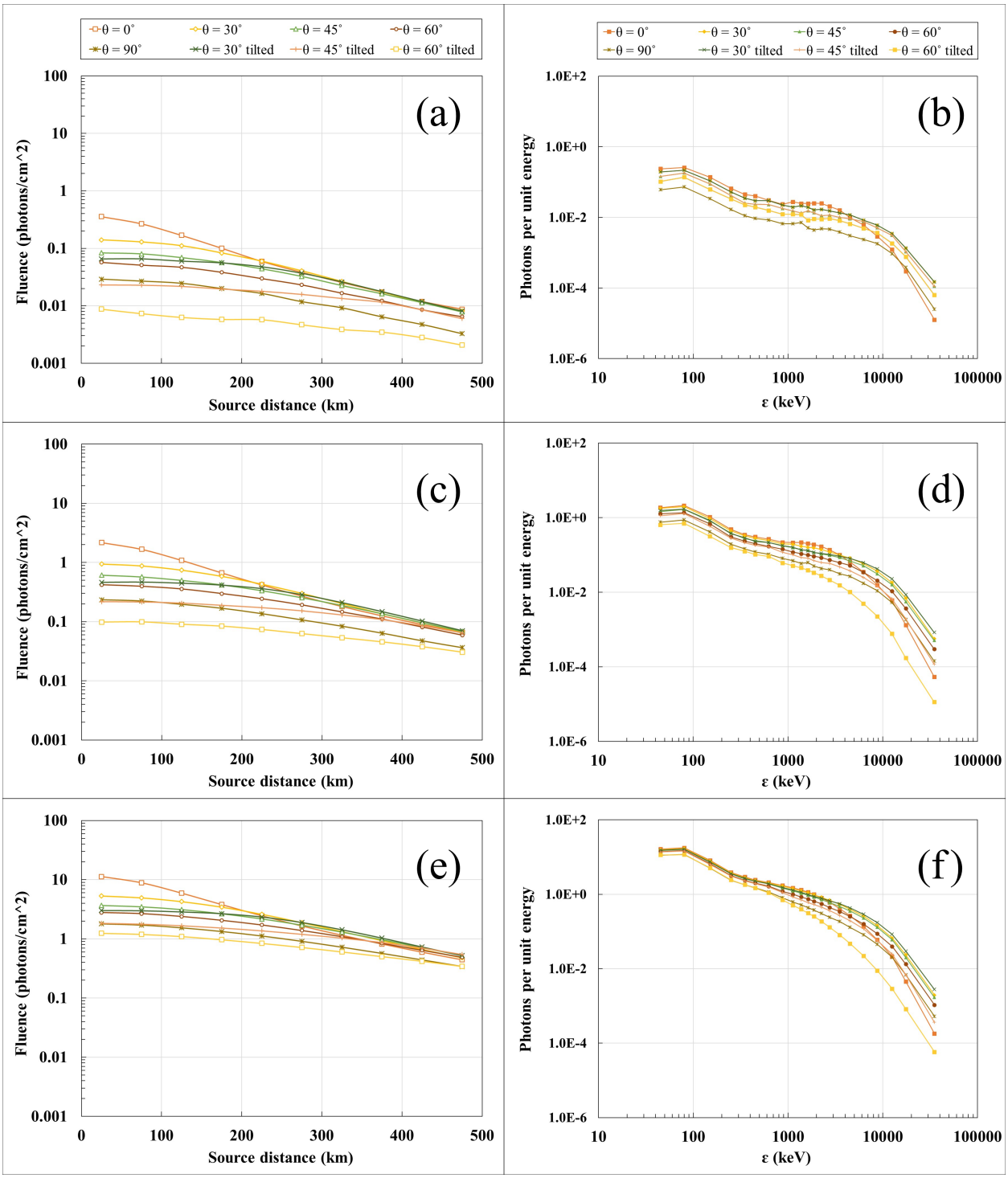

Figure 4.3: Gamma rays fluence versus subsatellite distance (left) and energy spectrum (right) of TGFs initiated at 12.5 km (a, b), 15 km (c, d) and 20 km (e, f). The energy spectrum is calculated at off-axis distance of 250 – 300 km. In total, 8 beam widths are simulated including cones with 0°, 30°, 45°, 60° and 90° uniform distribution and tilted beams with 30°, 45° and 60° direction with respect to z-axis. Note that energy spectrum is hardening as source altitude increases.

with the hardness ratio calculations reported earlier in Figure 4.2. For any source altitude up to a few MeV ($\sim$ 3 – 5 MeV), the photon density per unit energy of vertical beam is higher than other beam geometries. However, above that, wider beams produce more energetic photons. This is because gamma rays from vertical beam should scatter to reach the selected area ($\sim$ 250 km off-axis distance), so their energy spectra fall off very quickly above a few MeV. Tilted beams up to 45° tend to produce almost similar energy spectrum as conical beams, while isotropic beam and 60° tilted beams have the lowest number of photons per unit energy.

4.4.2 Temporal properties of TGFs

The duration of a TGF event at low-Earth orbit depends on many factors including the location of the spacecraft with respect to the TGF source, the source altitude, energy cutoff and geometry of the initial beam. In this section, the t50 parameter is calculated with two energy cutoffs at 30 keV (Figure 4.4) and 300 keV (Figure 4.5) and plotted versus the off-axis distance for the same dataset as previous sections. In general, as the off-axis distance increases, the t50 duration is increasing as well for all conical beam widths, which agrees with earlier reports *Celestin and Pasko [2012]; Fitzpatrick et al. [2014]*. This trend is purely due to Compton scattering which elongates the time of arrival of photons and increases the duration of TGFs seen in space. However, this effect is particularly different for the tilted beams which is due to the difference in geometry and scattering angles. For example, the duration of a 45° tilted beam of TGF initiated from 15 km decreases from 14 μs near the nadir point to about 7 μs at 500 km away with 300 keV cutoff (Figure 4.5, middle). If the gamma rays at the source travel along the 45° angle with respect to the z-axis without any scattering, they reach low-earth orbit at about 500 km off-axis distance. Then the lowest t50 duration for such tilted beams should be expected at that distance. However, since the amount of column depth that they face is clearly higher than vertically traveling along z-axis (due to diagonal path), there will be still some delays in the time of arrival of photons which causes a relatively larger duration compared to vertical beam of TGFs.

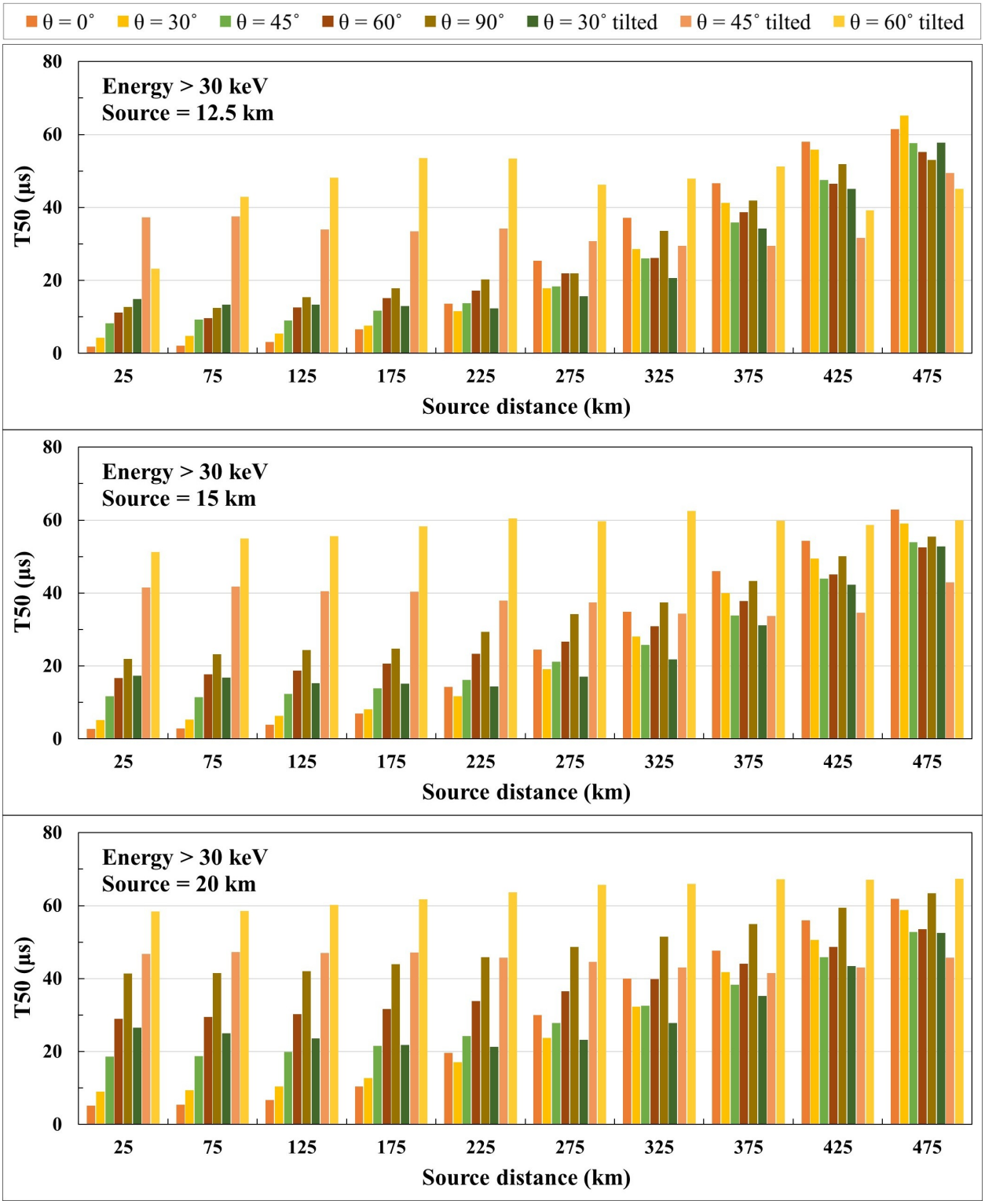

Figure 4.4: $T50$ duration versus distance between the subsatellite point and TGF source for three source altitudes at 12.5 km (top), 15 km (middle) and 20 km (bottom) with a cutoff energy of 30 keV. In total, 8 beam widths are simulated including cones with 0°, 30°, 45°, 60° and 90° uniform distribution and tilted beams with 30°, 45° and 60° direction with respect to z-axis.

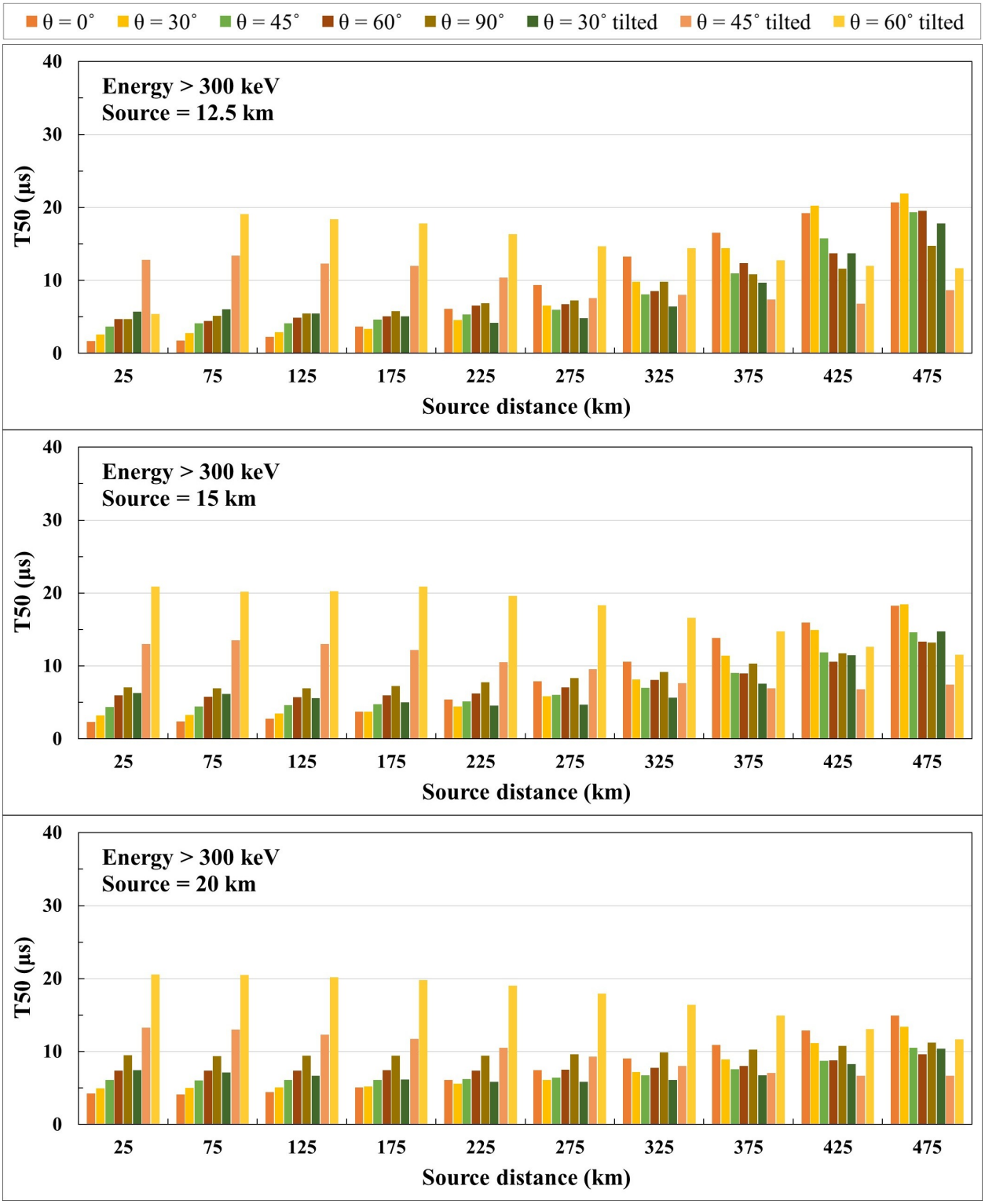

Figure 4.5: $T50$ duration versus distance between the subsatellite point and TGF source for three source altitudes at 12.5 km (top), 15 km (middle) and 20 km (bottom) with a cutoff energy of 300 keV. In total, 8 beam widths are simulated including cones with 0°, 30°, 45°, 60° and 90° uniform distribution and tilted beams with 30°, 45° and 60° direction with respect to z-axis.

Near the nadir point (R $\sim$ 25 km), the TGF duration increases as the width of conical beam broadens. For instance, a 15 km source altitude has a duration of 3 μs for a vertical beam and a duration of 22 μs for an isotropic beam (Figure 4.4, middle). However, as the off-axis distance increases (R > 300 km), this behavior reverses and a longer duration is observed for vertical beam compared to isotropic beam. This is because gamma-ray photons from a vertical beam reach the nadir point with minimum number of scatterings, while for an isotropic distribution some of the photons have undergone multiple Compton scattering which produces a low energy tail and increases the TGF's duration. The same scenario is true for large off-axis distances, but this time photons from vertical beam would undergo Compton scattering to reach that region. A similar trend is observed for other source altitudes. Given that probability of detection of TGFs by satellite is proportional to product of the photon fluence, the characteristic surface of the detector, and the probability of the satellite to be present at an off-axis distance of R, it has been reported that R $\approx$ 200 km corresponds to the maximum detection probability *[Celestin and Pasko, 2012]*. At this distance, an average duration of 10 μs (for 12.5 km source) to 30 μs (for 20 km source) is found for TGFs injected instantaneously in our simulation.

Celestin and Pasko [2012] have simulated an instantaneous 45° conical beam of TGF with the source altitude at 15 km and have shown that Compton scattering alone could be responsible for time dispersions greater than 50 μs at an off-axis distance of 250 km. However, our results show that the time dispersion associated with Compton scattering is much less than 50 μs and depending on the beam width and source altitude could vary from 10 μs to 50 μs at the same distance. This is in agreement with earlier work reported by *Fitzpatrick et al. [2014]*. The low energy cutoff plays an important role in the calculation of t50 parameter. Given that low energy photons arrive later than higher energy ones due to being Compton scattered, having a lower cutoff energy will result to a longer t50 duration. This could be seen by comparing Figure 4.4 and 4.5, where t50 duration for the 30 keV cutoff is almost twice of the 300 keV cutoff. As the source altitude increases this difference signifies which is due to smaller column depth and escaping low energy photons from

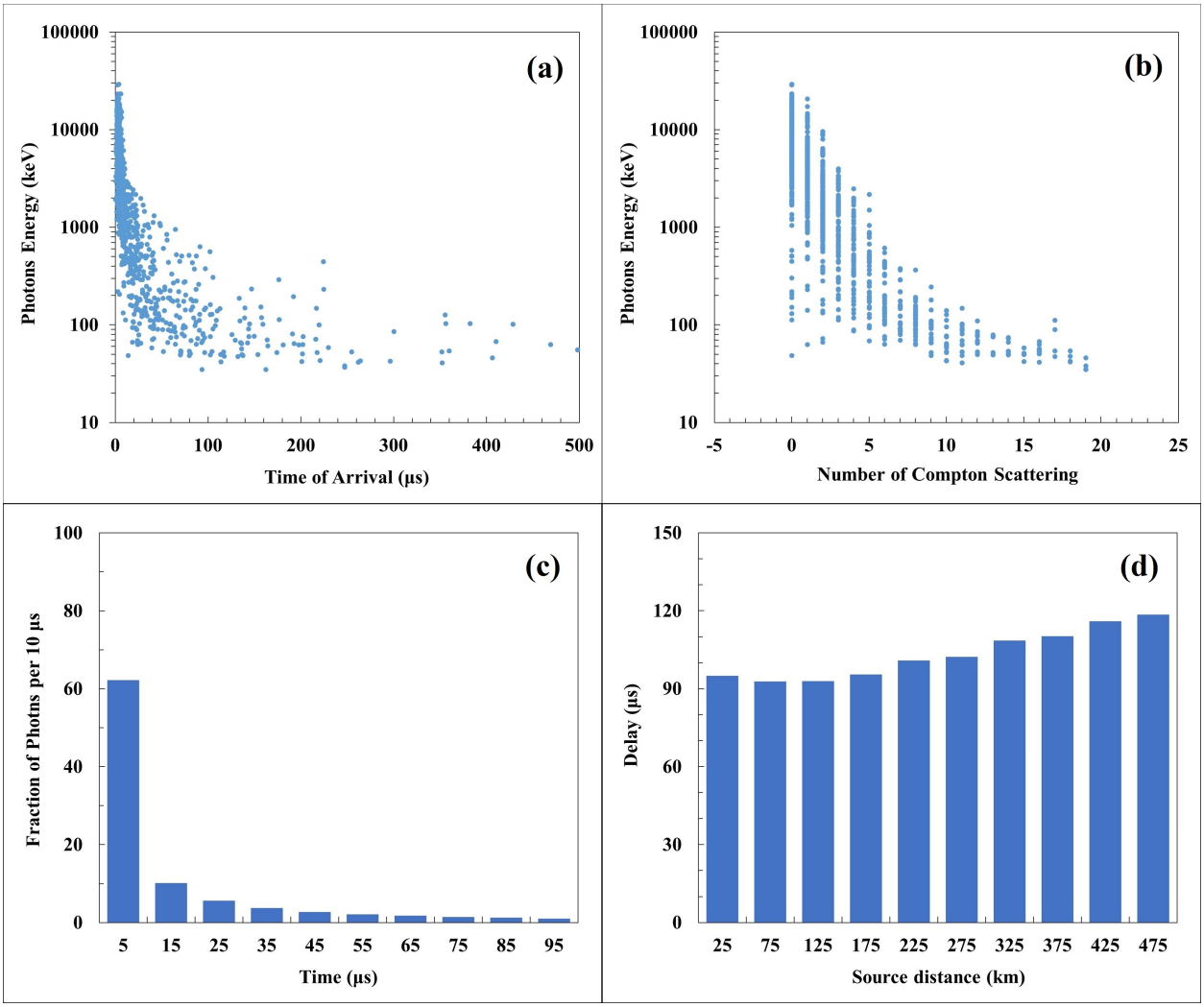

Figure 4.6: Photons energy versus time of arrival (a) and number of Compton scatterings (b) for a 45° conical beam of TGF with source altitude at 15 km. Corresponding light curve in the first 100 μs with 10 μs bins (c) and delay between low energy (E < 300 keV) and high energy photons (E > 300 keV).

the atmosphere. This result agrees with the hardness ratio and energy spectrum results in Figures 4.2 and 4.3, where for a higher source altitude a softer energy spectrum was reported.

4.4.3 Compton Scattering effect on the duration of TGFs

In this section, we have selected the most typical modeled scenario for the TGFs, 15 km source altitude and 45° conical beam *[Dwyer and Smith, 2005; Ostgaard et al., 2008; Fitzpatrick et al., 2014; Celestin and Pasko, 2011; Carlson et al., 2009]*, to study the effect of Compton Scattering

on the duration of TGFs. The detection area for the Figure 4.6 was chosen to be between 250 and 300 km and cut-off energy was set to 30 keV. Figure 4.6a shows the energy of photons versus time of arrival with respect to the first photon. As it can be seen, the majority of the photons arriving in the first 10 μs have energies above 1 MeV and as the time goes towards the next 10 μs, the average energy falls off under 1 MeV and eventually photons with energies around 100 keV reach last. Given that the average energy of runaway electrons associated with the gamma rays produced during RREA processes at the source is about 7 MeV, it seems gamma rays arriving in the first 10 μs period come directly from the source with minimum number of scatterings. This can be seen more clearly in Figure 4.6b, where the photons energy is plotted versus number of Compton scatterings. MeV range photons have reached the detection area with zero or one Compton scattering, while as the number of scatterings increases, the average energy drops to hundreds of keV. This shows that how Compton scattering delays the photons and increases their time of arrival. Note that the importance of cut-off energy in the calculation of t50 parameter is more visible in this plot. If we set the cut-off at 30 keV, all the low energy photons with several number of scatterings would be included in the calculation which result to a large t50 duration. But, by setting the cut-off value to 300 keV, almost no photons with number of scatterings greater than 5 would be included in the calculations.

Figure 4.6c shows the light curve of photons in the first 100 μs which is equivalent of zooming into the first 100 μs of Figure 4.6a. About 60% of the photons arrive in the first 10 μs bin, and about 77% of photons arrive in the first 30 μs. Given that in the calculation of t50, only the first 75% of arriving photons are included, for a wide 15 km TGF with 30 keV cut-off energy, a t50 duration of about 21 μs is calculated (see Figure 4.4, middle panel). With 300 keV cut-off energy, a higher fraction of photons arrives in the first 10 μs bin which drops the t50 duration by a factor of 3 to about 6 μs. Figure 4.6d shows the delay between the soft (E < 300 keV) and hard (E > 300 keV) counts as a function of off-axis distance. Not a significant variation in the delay is observed with increasing the off-axis distance which agrees with the earlier report *[Fitzpatrick et al., 2014]*.

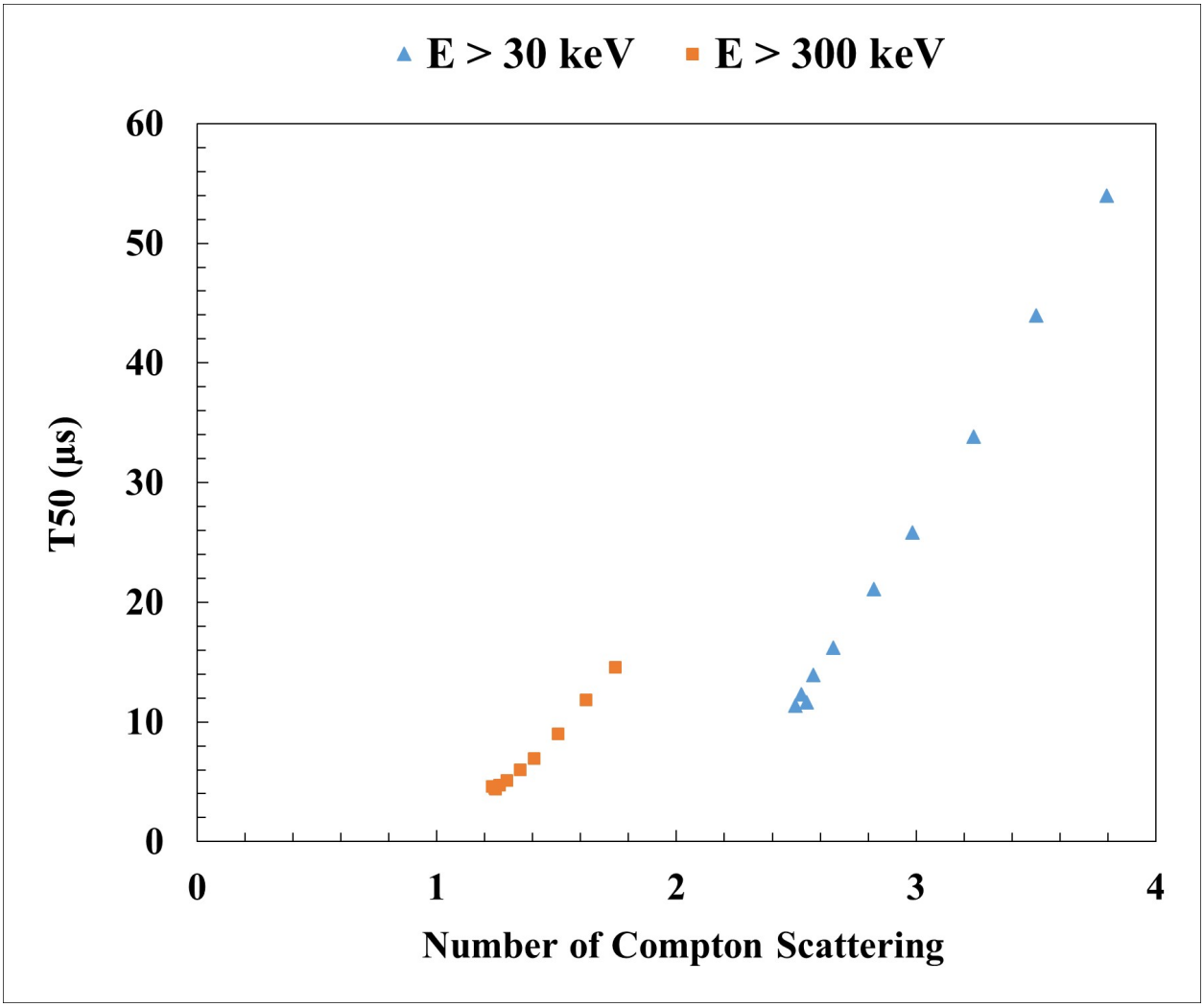

Figure 4.7: $T50$ versus the average number of Compton scatterings for a 45° conical beam of TGF with 15 km source altitude and two energy cut-offs of 30 keV and 300 keV. Note that as the number of scatterings increases, the detection distance increases as well.

Figure 4.7 shows the t50 duration as a function of number of Compton scatterings for two cut-off energies. Each point on this plot represents t50 calculated for the photons in one 50 km wide concentric annuli with the first one on the left closest to nadir point and the farthest on the right at 500 km distance. For 30 keV cut-off, t50 ranges from 12 μs to 54 μs with an average number of scattering from 2.5 to 4. While for 300 keV cut-off, t50 ranges from 4 μs to 15 μs with average number of scattering from 1.2 to 1.8. Note that the number of Compton scattering in this plot in averaged over total photons in the annuli and is particularly different from the x-axis of Figure 4.6b. It is obvious that by increasing the average number of scatterings, the t50 duration increases

as well, where this increase is more significant for the lower cut-off energies. *Celestin and Pasko [2012]* have shown that Compton scattering alone could be responsible for time dispersions of about 50 μs at 300 km distance which agreed with earlier measurements made by Fermi *Fishman et al. [2011]*, however our results shows that the time dispersion caused by Compton scattering should be as high as 20 μs and agrees with *Fitzpatrick et al. [2014]*, which suggests that temporal elongation due to Compton scattering is shorter than previously thought. Part of the difference between our results and *Celestin and Pasko [2012]* work could be due to different cut-off energies (50 keV in their work, and 30 keV and 300 keV in our work), but that would even make the difference larger. In fact, with a 50 keV cut-off at 250 km distance, a duration of about 18 μs should be expected from wide 15 km TGFs in our simulation. Then, if TGFs are produced by instantaneous processes at the sources, their expected t50 duration in space should be much shorter than it is suggested by earlier works.

4.5 Conclusion

In this chapter, we have investigated the spectral and temporal distribution of TGFs for a wide variety of beam geometries and source altitude. Spectral analysis of TGFs showed that energy spectrum is softening at larger off-axis distances and higher source altitudes. In addition, gamma rays fluence is increasing directly with source altitudes, in a way that the vertical beam's fluence was higher than other geometries near the nadir point, while conical beams had slightly higher fluence than vertical at distances above 300 km. The temporal distribution of TGFs have been investigated using t50 parameter. It has been shown that t50 is increasing with off-axis distance and source altitude, while having a higher cut-off energy reduces the duration of TGFs. Furthermore, narrow beam had a shorter t50 duration than wider beams near the nadir point and as the off-axis distance increases, wider beams showed shorter durations than narrow beams. A detailed analysis of Compton scattering effect on the duration of 15 km TGFs with conical angle of 45° showed that photons arriving in the first 10 μs are very energetic (above 1 MeV) and have zero or one Compton

scattering, while the ones arriving in the next 10 μs bins have had multiple scattering with energies around 100 keV. Our results suggest that temporal elongation caused by Compton scattering for instantaneous sources is about 20 μs at 300 km distance which is about 2.5 times smaller than what it was thought before. Then, if TGFs are produced by fast processes such as stepping of lightning leaders, it is possible that their duration would be much shorter than 50 μs proposed by earlier Fermi measurements.

CHAPTER 5

BALLOON-BORNE INSTRUMENTATION OF DETECTION GAMMA-RAY GLOWS

5.1 Scientific Motivation

One of the greatest unsolved problems in the atmospheric sciences is explaining how lightning initiates inside thunderstorms *[Dwyer and Uman, 2014; MacGorman and Rust, 1998]*. Lightning created inside thunderclouds is a kilometer scale electrical discharge. For such an electrical discharge to occur in our atmosphere, the electric field strength must somewhere exceed the conventional breakdown field of $E_k \sim 3{\times}10^6$ V/m$\times$n. The problem is that decades of in situ electric field measurements have failed to find electric fields as large as E_k *[Rakov and Uman, 2003]*. Indeed, it appears that the fields inside thunderstorms rarely, if ever, exceed about $0.3E_k$.

Most theoretical work on lightning initiation hypothesizes that small-scale electric field enhancements near the surfaces of hydrometeors (water and ice particles) may initiate streamers (cold filamentary discharge structures) *[Bazelyn and Raizer, 1998; Liu et al., 2012,?; Peterson et al., 2008]*. Laboratory experiments and numerical calculations have found that the ambient field needed to initiate positive streamers from hydrometeors and allow the streamers to propagate is slightly larger than the runaway electron avalanche threshold. It is not clear how streamers then result in lightning. Somehow, they must create a hot propagating leader channel, but the sequence of events that leads to the creation of such a channel remains a mystery. It has been suggested that the joint action of many streamers may locally enhance the electric field to near E_k, allowing the leader to form *[Griffiths and Phelps, 1976]*. A fundamental difficulty with making progress is that we don't know what electric field conditions are common inside thunderstorms. Nevertheless, even though streamer production may not be a sufficient condition for lightning initiation, it is

likely to be a necessary condition. Thus, electric fields large enough to produce runaway electrons and gamma-ray glows is likely to also be a necessary condition, since the electric field threshold for their production is less than the threshold for streamers to form. Therefore, it is expected that lightning initiation should be preceded by gamma-ray glows, although not all of them will necessarily be detectable.

It is an interesting question whether or not the enhanced flux of energetic electrons and gamma rays plays some role in the lightning initiation process or if the gamma-ray glow is instead just a useful tracer of the strong electric fields required for lightning initiation. It is possible that the ionization created by the runaway electron may locally enhance the electric field. This ionization may also help seed the streamer discharges, since streamers require the presence of initial seed electrons, which may not always be present near the surfaces of the hydrometeors. Conversely, RREA multiplication may also limit the electric field *[Dwyer, 2003; Liu and Dwyer, 2013]*, inhibiting lightning initiation. Experience has shown that it is difficult to put instruments in the high-field regions where lightning initiates. One explanation is that these regions are relatively small and may not last for very long (a hypothesis that will be tested by measuring the durations of the glows). Also, the presence of the balloon, aircraft or rocket used to make the measurements may alter the system, causing lightning to artificially initiate before the field can rise to the point where lightning would initiate naturally. On the other hand, the gamma rays generated in the lightning initiation region travel quite far (e.g., a kilometer or two) through the atmosphere, allowing the presence of the high-field region to be inferred without the need to enter it. Furthermore, combining these observations with modeling and supplementary data, such as Lightning Mapping Array (LMA), radar and other meteorological data, will allow us to infer properties of the high-field region where lightning initiated.

Over the past three years, our group at UNH in collaboration with Florida Tech have developed and tested balloon payloads for measuring gamma-ray glows inside and near thunderstorms. The strategy of the balloon campaign was to develop and test low-cost, potentially expendable payloads, with data that are transmitted to the ground, that could be launched in large numbers into

thunderstorms. This allows us to launch in central Florida, the thunderstorm capital of the United States, even though some flights might potentially be lost in the Ocean. In the following sections, we will describe the details of development and calibration of instruments and the result of test flights during the summers of 2017 and 2018 will be presented.

5.2 Instrumentation

The standard payload consists of three major instruments including two Geiger counters, one gamma-ray scintillation detector and one electric field mill sensor, designed and calibrated to measure both polarity and amplitude of the vertical electric field inside the thunderstorm region. Figure 5.1 shows the block diagram of the detectors and payload electronics. In order to distinguish between charged particles and gamma rays, the scintillator was inserted between the GM tubes. Given that electron/positron beams are attenuated by more than a factor of ten through scintillation crystal and energetic gamma rays can pass through all three units (both GM tubes and crystal), the relative count rate between the tubes and crystal allows us to separate charged particles from gamma rays.

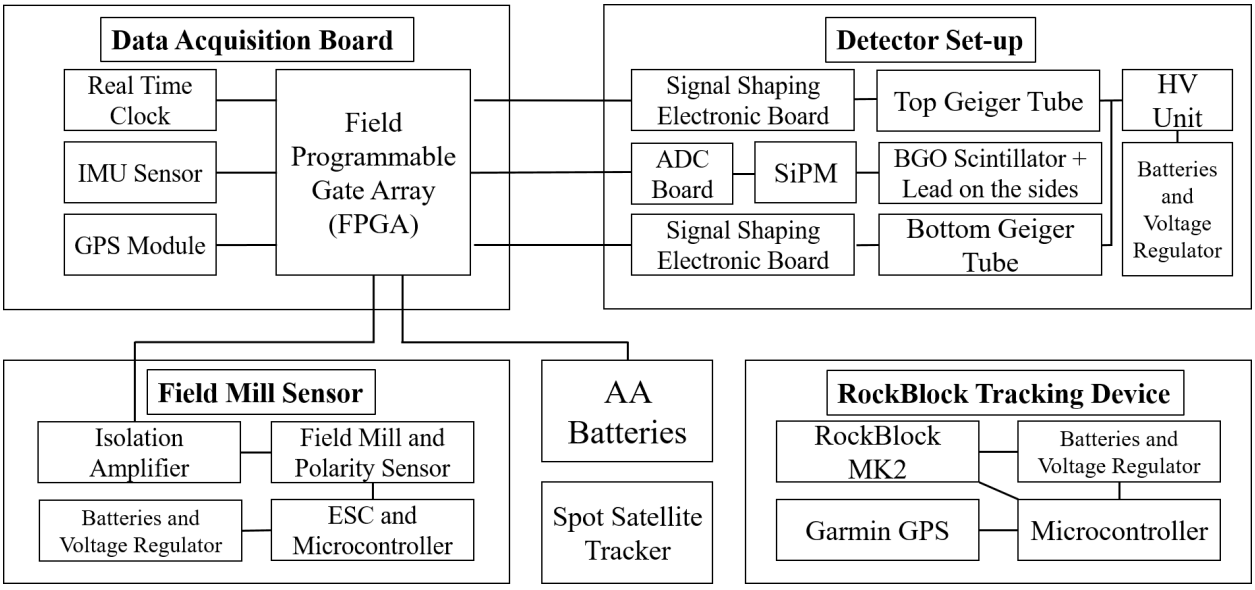

Figure 5.1: Schematic of the lightweight, inexpensive balloon payload for measuring gamma-ray glows from lightning. The detectors and the electronic parts have been developed and tested on multiple balloon flights.

A list of all possible relative count rates for different scenarios is shown in Table 5.1. For example, a downward beam of charged particles triggers an enhancement above the background in the top GM tube and crystal and then would be attenuated significantly and does not reach the bottom GM tube. In addition, if the polarity of the electric field is known through electric field mill sensor, we can differentiate between the positron and electrons, since they are moving in opposite directions. Detecting positron beams, which are predicted by relativistic feedback theory, would be a major discovery.

	Bottom Geiger counter rate	**Scintillator/PMT rate**	**Top Geiger counter rate**
Downward electron/positron beam	Small	Large	Large
Gamma rays from any direction	Small	Large	Small
Upward electron/positron beam	Large	Large	Small
Sideways electron/positron beam	Large	Large	Large

Table 5.1: The list of response of each counter for different beam directions and energetic components. By comparing the responses from the three counters, the directions and composition of energetic radiation could be determined.

5.2.1 Geiger–Müller Counters

Geiger–Müller (GM) counters were chosen because they are inexpensive, rugged, reliable, low power, very lightweight and produce large signals. The high gains and short pulse shaping times of the Geiger counters makes them relatively immune to microphonic noise, and no noise problems were encountered during the test flights or during tests on the ground. Although the Geiger counters have low-efficiency for detecting energetic photons, their efficiency is large enough to make high-quality measurements of the gamma-ray fluxes. In fact, based on the test results, flying a large number of inexpensive Geiger counters has proven to be at least as effective at recording gamma-ray glows as flying few more expensive detectors with higher efficiencies.

In this design, two GM tubes (LND 72118) were connected to a single HV unit (Pico Electronics 12AVR600 – 12 V input and 600 V output). For each counter, signal pulses are sent to the pulse shaping electronics, where they are differentiated to resolve pulses occurring close in time, amplified, discriminated to suppress noise and produce digital pulses. The digital pulses duration and amplitude are set to be about 6 μs and 3.3 V with a square wave shape.

5.2.2 Gamma-ray Scintillation Detector

To measure the energy spectrum of photons produced during gamma-ray glows, we have developed a scintillation detector using BGO (Bismuth Germanate, $Bi_4Ge_3O_{12}$) crystals and Silicon Photomultipliers (SiPM) which will be described here. An image of the assembled gamma-ray detector along with the electronics before the flight is shown in Figure 5.2.

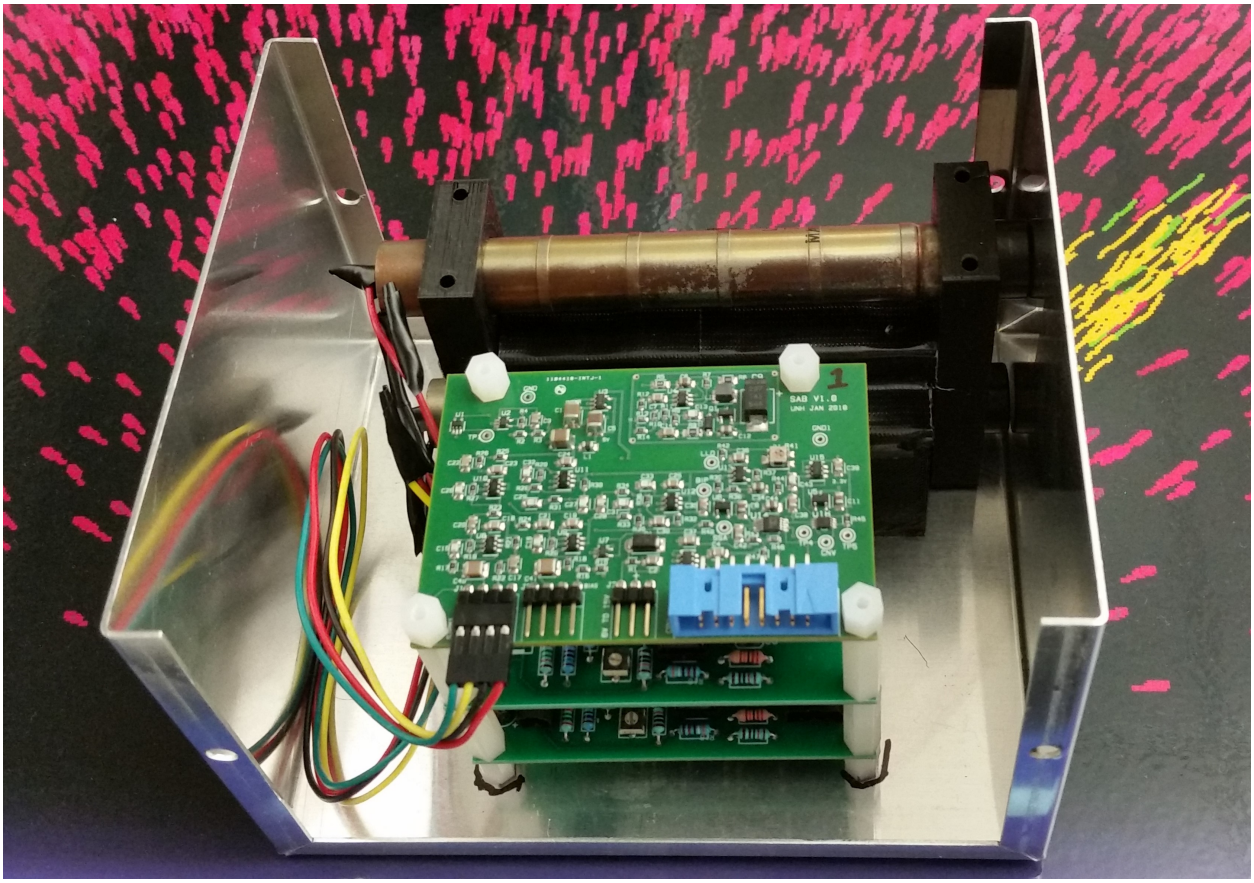

Figure 5.2: Scintillation gamma-ray detector along with the Geiger counters and electronic boards.

5.2.2.1 Scintillation Crystal

Scintillators are materials that convert the energy of ionizing radiation into a flash of light. Gamma rays interact with a scintillator by means of: 1) photoelectric absorption (dominant mechanism below 500 keV), 2) Compton scattering (dominant around 1 MeV and interaction probability proportional to the density), or 3) pair creation (dominant well above the threshold at 1.02 MeV). For efficient detection of energetic gamma rays, a scintillator should contain high atomic number elements (e.g. Ba, La, I, Cs, Pb, Bi) and have a high density. BGO was chosen because it is a high density (7.13 g/cm^3), high Z (83) scintillation material which does not cleave, and it is a relatively hard, rugged and non-hygroscopic. Due to its large atomic number, the photo fraction for gamma ray absorption is high which provides very good peak-to-total ratios. The BGO radiation length, which is 7/9 of the mean free path for high energy photons, is about 1.11 cm. BGO crystal does not show any significant self-absorption of the scintillation light and it can be machined to various shapes and geometries. The crystal housing can be simple since no hermetic sealing is required. The scintillation emission maximum of BGO is about 480 nm which matches very well with the peak sensitivity of chosen Silicon Photomultipliers. The rise time of BGO light output is very fast (tens of nanoseconds) and it has a decay time of about 300 ns which is fast enough for the spectroscopy of events with the rate of several kHz.

BGO crystals were purchased from Proteus company with overall dimensions of 18 mm$\times$18 mm$\times$100 mm. These numbers were chosen based upon the diameter and the length of Geiger-Müller tubes (18 mm$\times$95 mm), in a way that scintillator would be able to block upward or downward beam of charged particles whenever it is placed between the tubes. In addition, two pieces of lead (10 mm$\times$100 mm) were mounted on the sides of crystal to increases the blocking area. In order to maximize the light output of scintillator, BGO crystals were wrapped in a thin reflective material called Vikuiti Enhanced Specular Reflector (ESR). Vikuiti utilizes 3M multi-layer optical film technology to create a highly efficient, specular, reflector. It provides up to 98% reflectance across the visible spectrum. The Vikuiti sheets were cut and wrapped around an aluminum block (with similar dimensions to actual BGO crystal) and placed into an aluminum mold and baked in

the oven for an hour at 120°C to form. The housing of crystal was designed, and 3D printed in our lab with a window on one side (12 mm$\times$12 mm) for the SiPM. The SiPM units were coupled to the BGO crystal using a 3M Optically Clear Adhesive double-sided tape ($\sim$ 50 μm thickness) which provides 99% transmission at visible light. Note that BGO crystal is very sensitive to UV light which can degrade the material, so the assembly process was performed under the red light.

5.2.2.2 Silicon Photomultiplier

Silicon Photomultipliers were chosen because they offer a winning combination of properties compared to other photosensor technologies, such as Avalanche Photodiodes (APDs) and Photomultiplier Tubes (PMTs). These properties include high gain, excellent PDE and fast timing along with the practical advantages associated with solid-state technology: compactness, ruggedness, low bias voltage and insensitivity to magnetic fields. When a photon travels through silicon, it may be absorbed and transfer its energy to a bound electron which moves it from the valence band into the conduction band, creating an electron-hole pair. Applying a reverse bias voltage creates an electric field across the depletion region that will accelerate the charge carriers towards the anode (holes) or cathode (electrons). When this electric field reaches above a minimum level ($\sim$ 5×10^5 V/cm), accelerating charge carrier energizes to a sufficient kinetic energy level that can produce secondary electron-hole pairs through impact ionization. In this way, a single absorbed photon can trigger a self-sustaining ionization avalanche that will spread throughout the silicon volume. Eventually, the silicon will break down and become conductive, effectively amplifying the original electron-hole pair into a macroscopic current flow. This process is similar to the Geiger discharge observed in a Geiger-Müller tubes. Once the current started flowing, it should be stopped or "quenched" by some means. This is achieved by integrating a dense array of small, independent sensors (microcells), each with its own quenching resistor. The quench resistor reduces the bias across the diode to a value below the breakdown, thus quenching the photocurrent and preventing further avalanches from occurring. After quenching is finished, the voltage across the photodiode

recharges to its nominal value. During this process, all other microcells remain active and ready to detect photons.

In this design, we have used a 2×2 array of SensL J-series SiPM with Standard Mode Readout and BGA pinout (Model# 60035-4P-BGA). Each SiPM array has a total active area of 12×12 mm^2 with about 89168 microcells and a fill factor of 75%. The typical breakdown voltage is about 24.5 V with a recommended operating voltage of 27 V. At the recommended voltage, the gain is about 2.8×10^6 with an average dark current rate of 45 kHz/mm^2. The SiPM has a peak PDE wavelength of 420 nm and a temperature coefficient of 21.5 mV/°C.

5.2.2.3 Analog Board

The analog board is designed for use with SensL J-series Silicon Photomultiplier arrays. The arrays are mounted on a small circuit board and are optically mated to the scintillator material. A short 4-pin cable connects the SiPM mount to the analog board. There is an option to use two SiPM units on the scintillator (one on each end of the crystal) for better light collection. The signal is summed to produce a single event pulse. A scintillator light pulse causes a charge pulse out of the SiPM. The charge is integrated to produce a voltage proportional to the energy of the event detected in the scintillator. This design uses shaping times optimized for about a 300 ns light pulse expected from BGO scintillator material. A fast discriminator is used to reject noise below threshold and to provide timing for peak capture. The circuit uses a bipolar shaper with a zero crossing-point that is nearly independent of pulse amplitude. This provides an accurate time reference for peak capture. A slower pulse shaper delays and stretches the peak for more accurate amplitude capture. The peak of the slow shaper occurs at a fixed delay time after the discriminator fires. The peak amplitude is captured and converted to a 16-bit digital value. The event is latched, and any further events are ignored until the digital control reads out the saved peak value. Once the readout completes, the circuit is ready to capture the next event.

The dead-time per event is: 2 μs + CPU response time + SPI readout time. The discriminator has a two-pulse resolution of 5 μs for events near threshold so there is no advantage to using a

dead-time of less than that. A dead-time of up to 10 μs is reasonable since it causes less than 1% rate correction for a maximum event rate of 1 kHz. Longer processing times can be used but dead-time correction would be needed if accurate event rates are desired. If a small event occurs within 100 μs of a large event, the second event may see some amplitude error because the slow shaper waveform has not completely returned to zero. This effect is very small for event rates below 1 kHz but can be significant for a mix of high and low energy events at rates above 5 kHz.

A trim potentiometer on the board allows manual setting of the delay to the peak location. Initial part tolerances can cause a fairly large variation but once it is set, the delay is fixed except for a small temperature variation. Optimal timing gives the best noise and linearity performance, but a small delay error does not have a big effect. The charge amplifier threshold and gain are fixed and provide a dynamic range of about a factor of 260 (between threshold and maximum linear pulse height). The scaling to energy is determined by the scintillator detector light output, light collection efficiency and SiPM gain. The SiPM gain can be adjusted to give the desired energy threshold. Events larger than the max limit do not cause damage but the amplitude will be clipped. The full-scale data range of interest does not have to extend to the max pulse range. The 16-bit ADC has adequate resolution without using its entire range. The nominal SiPM gain (for 27.0 V at 20 C) is 2.8×10^6. The nominal charge threshold is 5 pC which is equivalent to 5 pC/($2.8\times10^6\times1.6\times10^{19}$)=11.2 photo electrons. The SiPM dark noise produces events of a few photo electrons at MHz rates so the threshold will likely need to be higher than 5 pC (gain set lower) to keep the noise event triggers down to a few Hz.

The overall energy to pulse height conversion factor is determined by the SiPM gain. It can be adjusted by a digital potentiometer installed on the board. By sending incremented/decremented pulses between 0 and 64 to the trim, any Bias voltage between 25 V and 30 V is accessible. The SiPM gain at a fixed bias voltage varies with temperature. The gain change can be compensated by varying the bias voltage. The bias temperature coefficient for the J-series SiPM is specified as less than 21.5 mV/°C, however the BGO crystal light output efficiency can increase up to 50% at lower temperature, so the overall temperature compensation was found through thermal calibration of

each unit individually which will be described later. The unit-to-unit variation in SiPM temperature coefficient is significant so the temperature coefficient trim resistor may need to be adjusted to get good gain compensation. This was achieved during thermal calibration of each detector. The temperature sensor is on the analog board so good compensation requires that the SiPM and analog board are operating at close to the same temperature.

The input power connector uses 3 pins with positive power on the center pin. This allows the connector to be flipped without causing any damage, but it is still important to be sure the 3 pins are aligned properly. The power input was designed for operation from an unregulated battery voltage in the range of 6 V to 14 V (Recommended voltage $\sim$ 7.5 V). The board draws about 5 mA with Bias off and about 11 mA in normal operation. It requires a maximum surge of 70 mA for about 10 ms at Bias turn on. The SiPM connectors are not keyed. It is important to be sure they are oriented correctly. There are two connectors to allow the option of mounting two SiPMs to the same scintillator. The signals from the two are summed together. If only one is used the other can be left open.

5.2.2.4 Pulse Height Calibration

Depending on the energy of gamma rays passing through the BGO crystal and the preset gain of SiPM, different pulse heights would be expected from the analog board. After trying several gain values, a gain of 25 out of 64 (digital potentiometer setting) was selected for the final configuration to achieve the best energy resolution with minimized dark current. With the current electronics, a gain of 25 is equivalent to a bias voltage of 26.6 V or SiPM gain of 2.3×10^6. To calibrate the pulse height spectrum of scintillation detector, we have used three radioactive sources including Ba-133 (356 keV), Cs-137 (662 keV) and background radiation of K-40 (1.46 MeV) and calculated the number of counts versus ADC counts which is shown in Figure 5.3. The total duration of exposure to radioactive was about 5 minutes. There is about 0.5 V offset in the input of ADC which moves the baseline to about 8300 in the ADC counts.

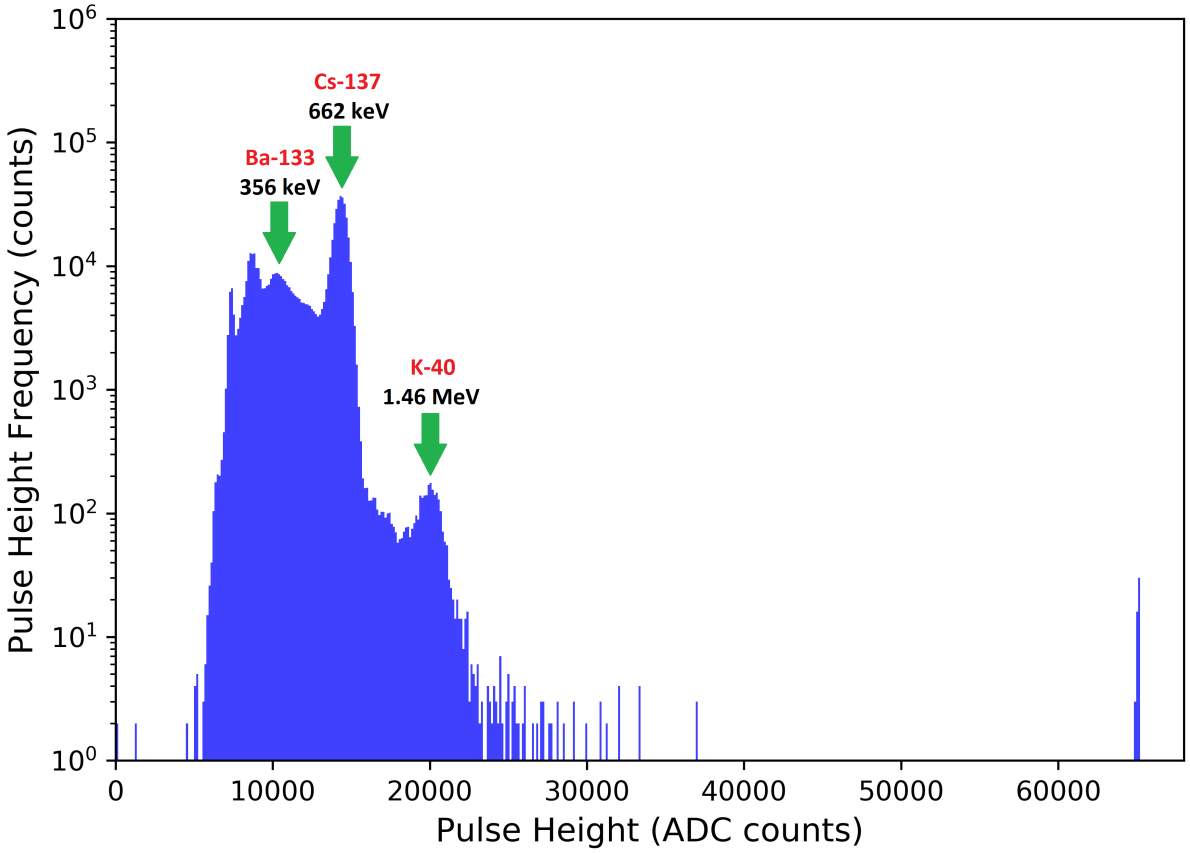

Figure 5.3: Pulse height spectrum of scintillation detector with three radioactive sources. Note that the baseline of 8300 in ADC counts is the zero-energy level.

To find out the detectable energy range, the pulse height versus the energy of photons for three gain values (1.8×10^6, 2.3×10^6 and 2.8×10^6) is plotted in Figure 5.4. These gain values are equivalent to 26.2, 26.6 and 27 V Bias voltage at room temperature respectively. With a 16-bit ADC, the maximum number of ADC counts is equal to 2^{16}=64536. By plugging this number into the fitted equation (green equation in Figure 5.4), the maximum detectable energy is calculated to be about 5.8 MeV at gain of 2.3×10^6. As the preset gain increases, the slope of the fitted line increases which reduces the maximum detectable energy. Given that MeV range gamma ray would probably have one or two interaction with the 18 mm thick BGO crystal before exiting the scintillator, the 5.8 MeV energy range seems adequate. Each SiPM unit has its own breakdown voltage, so a preset gain on the software might cause a slight change in the pulse height for different detectors. To

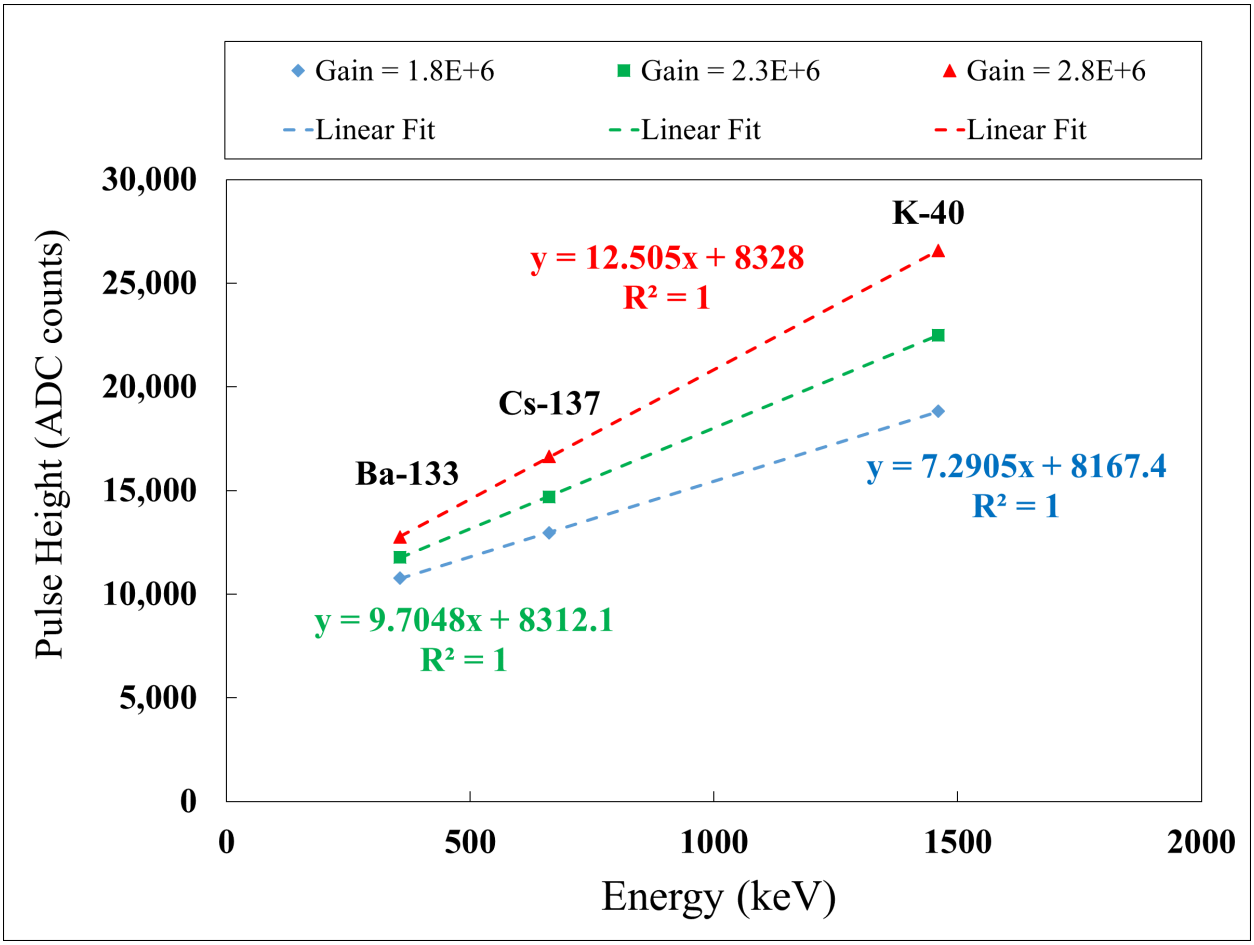

Figure 5.4: Pulse height versus energy of the photons three radioactive sources for three different gain values. The green line gain was chosen for the final flight configuration.

accurately record the pulse height, the temperature and Bias voltage are being monitored as well during the flight.

5.2.2.5 Thermal Calibration

Ambient temperature change affects the SiPM breakdown voltage and the dark count rate. The SensL SiPM has a temperature coefficient of 21.5 mV/°C and if large temperature fluctuations are experienced, it will change the effective overvoltage and affects many of the SiPMs performance characteristics. For stable operation during the balloon flight, a bias compensation was included which automatically adjusts the overvoltage based on the temperature. With this compensation, most of SiPM parameters such as gain, Photon Detection Efficiency (PDE) and timing will remain

the same as at room temperature. However, the dark current significantly reduces at lower temperature due to a change in the generation rate of thermal electrons. We have performed thermal calibration on each detector between ambient temperatures of -20°C and 40°C and recorded the pulse height of Cs-137 for three gain values which is plotted in Figure 5.5. Originally, we set the temperature coefficient to 21.5 mV/°C, however due to the dependency of BGO light output on the temperature, we had to run several thermal tests to find the optimum value for the overall temperature coefficient. Our calibration showed that an average of 31 mV/°C temperature compensation is required to keep the Cs-137 pulse height constant. This means that for every 10°C drop in the temperature the bias voltage needs to be reduced by 0.31 V. Figure 5.6 shows the bias voltage

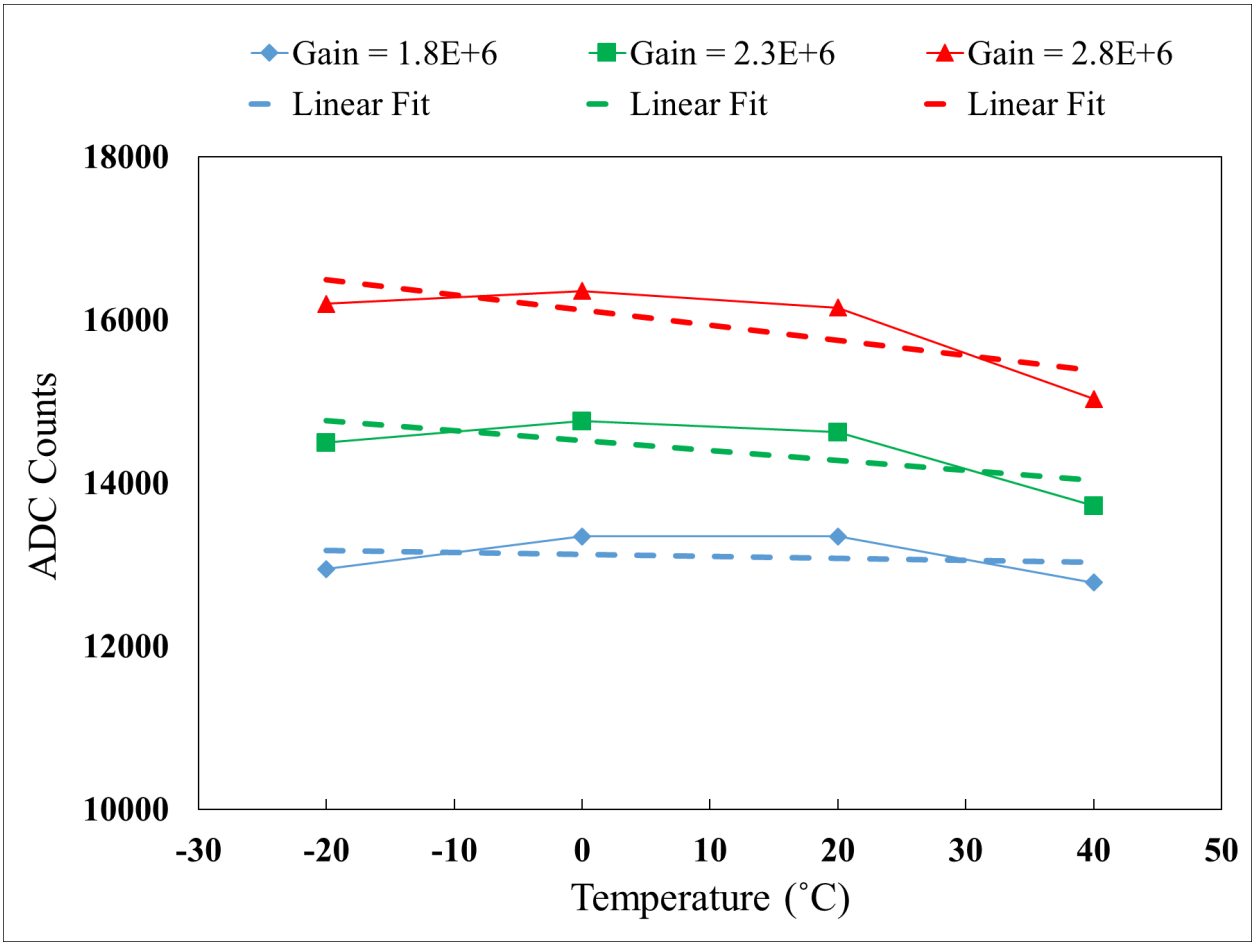

Figure 5.5: Thermal calibration of scintillation detector with Cs-137 source. Note that with a 31 mV/°C temperature compensation coefficient, Cs-137 peak almost stays constant between operating temperatures of -20°C and 40°C.

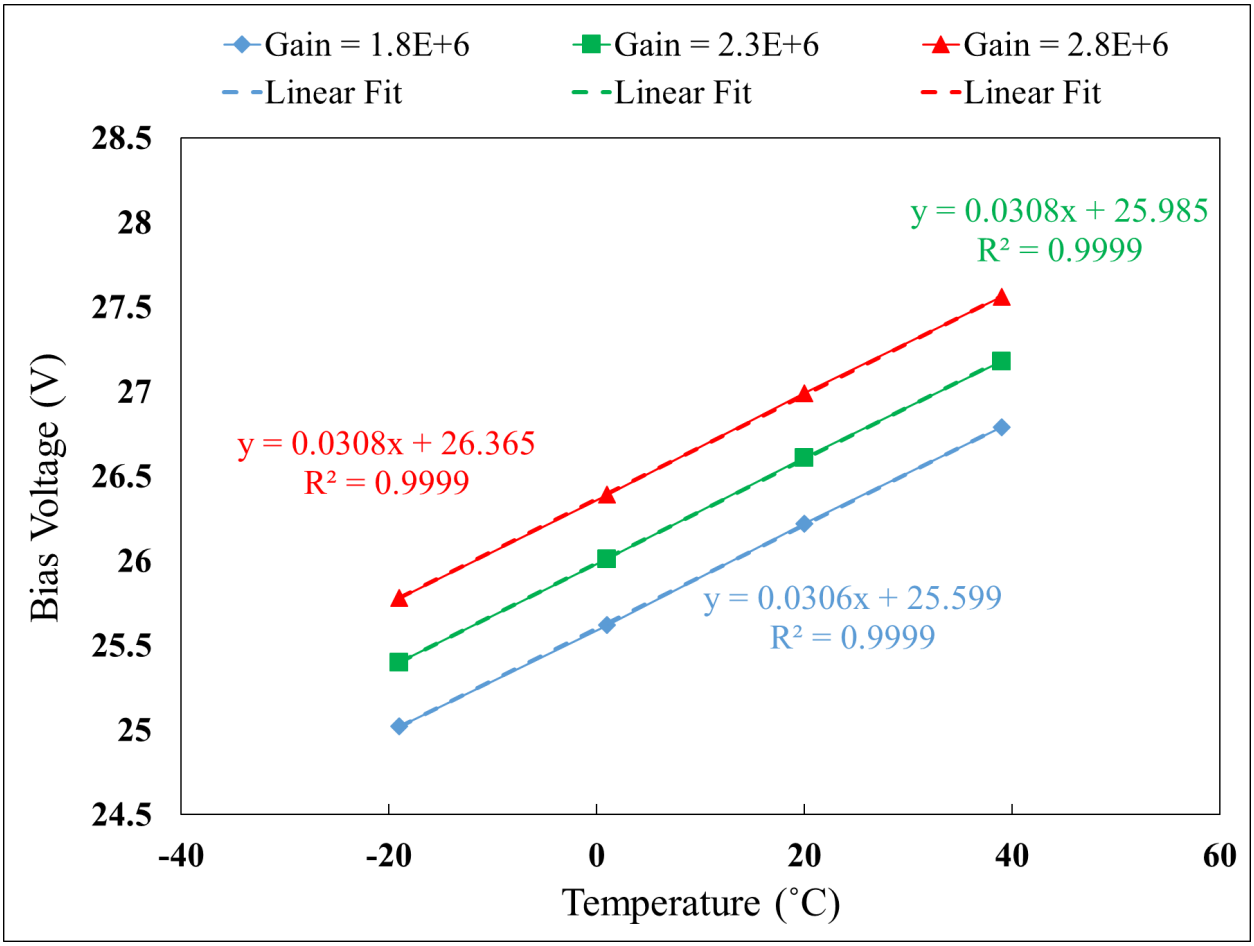

Figure 5.6: The applied bias voltage on SiPM versus ambient temperatures of -20°C and 40°C for three gain values. As the ambient temperature increases, a higher bias voltage is required.

versus the temperature for three gains values. The acquired temperature coefficient is independent of the SiPM gain and only depends on the value of trim resistor (R13) on the analog board.

5.2.3 Electric Field Mill Sensor

We have designed and developed a light-weight low-power electric field mill sensor to measure the magnitude and polarity of electric fields inside thunderstorms. A field mill detects a static or slowly varying external electric field by means of a mechanical modulator that produces a time-varying induced electrical charge signal *[Bateman et al., 2007]*. The main components of the field mill sensor are: (1) a sensor plate, (2) a lightweight 3D printed platform on which the sensor plate is mounted, (3) a shutter plate (rotating shield electrode), and (4) a brushless motor to rotate the

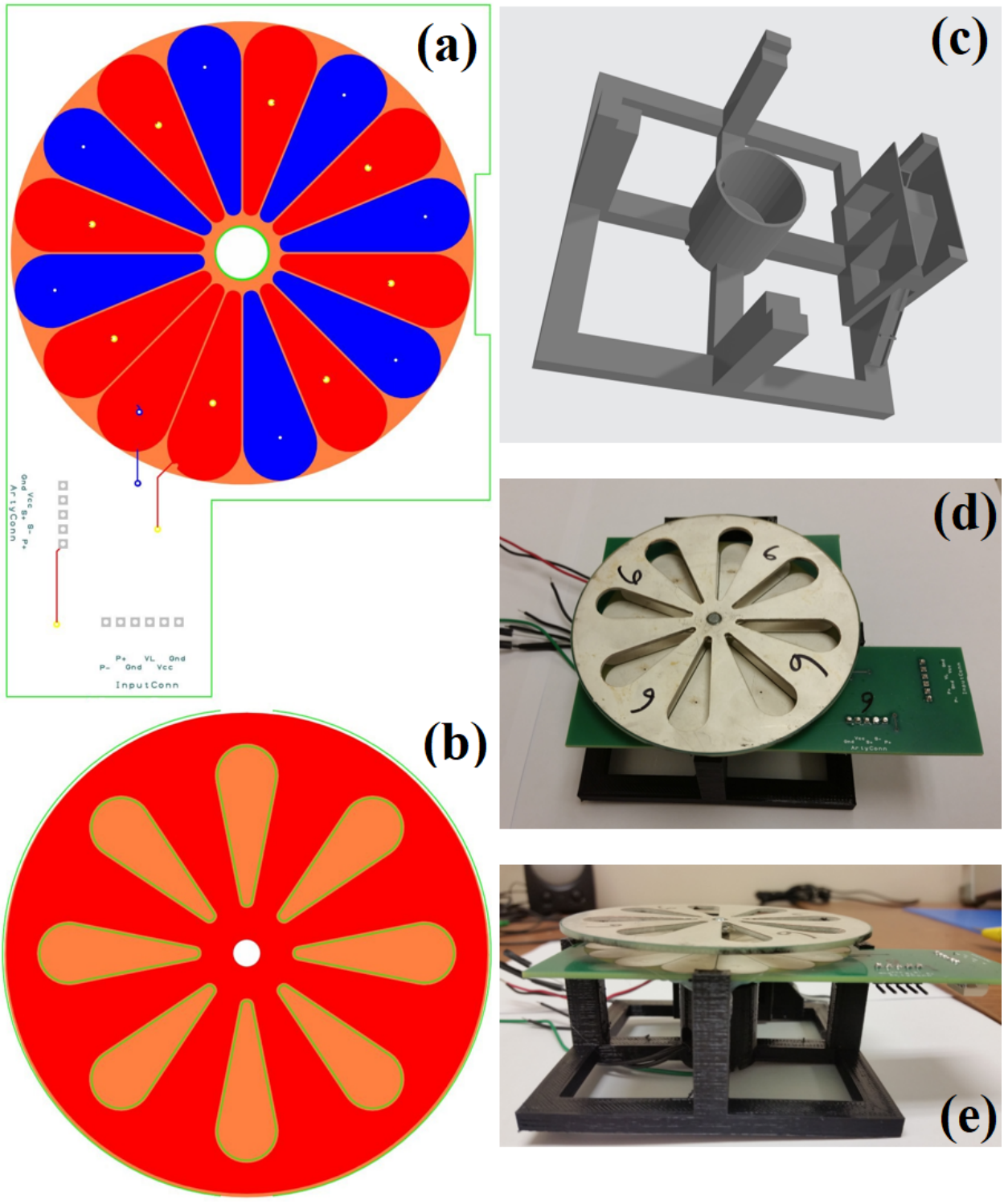

Figure 5.7: Schematic of the field mill sensor and shutter plates (a, b), the platform design (c), and the image of final assembled version of the device (d, e).

shutter plate. Figure 5.7 shows the schematic of the field mill along with the final assembly of the device. The pattern of the plates were designed in SolidWorks and then imported into PCB Artist Software to map into PCB design and include the electronic components. Both plates are made from PCB covered with a thick layer of Silver on top which has the highest conductivity between metals at room temperature (σ=6.3$\times$10^7) and improves the sensitivity of the device significantly. The Silver layers on the sensor plate are divided into two independent patterns (shown as blue and red pieces in the Figure 5.7a), where each colored pattern represents one end of the differential signal. The blue (red) pieces are connected in series on the back. The platform on which the sensor plate is mounted (see Figure 5.7c) is designed and 3D printed with PLA material in the lightning lab of UNH with an overall dimension of 10 cm$\times$10 cm. The brushless motor used here (DYS SE1407 3600KV) can produce a massive 450 g of thrust with a shaft diameter of 3 mm. Brushless motors were used to avoid the high level of wideband noise associated with the arcing of brushes in conventional DC motors. The motor shaft is screwed to a steel T-type nut which is glued with to the back of shutter plate via adhesive conductive epoxy (AA-DUCT 902) and dried at room temperature for 24 hours. With this setup, the vertical distance between the sensor and shutter plates was about 1 cm. If this distance increases, a lower overall gain would be expected.

As the brushless motor rotates the shutter plate, two parts of sensor plate (red and blue pieces) are being exposed to electric field lines alternately. This exposure will induce electric charge on the sensor electrodes, as given by Equation 5.1, resulting to an oscillating signal.

$$q(t) = \varepsilon_0 E \times A(t) \tag{5.1}$$

This signal has an amplitude proportional to the electric field normal to the plane of the sensor, a frequency of about 500 Hz which was 8 times (number of holes on the shutter plate) of the speed of motor, and a phase related to the position of the shutter with respect to the sensor plate. By calculating the time derivative of charge on the sensor surface, the induced current could be written as Equation 5.2, where E is the magnitude of electric field and A is the total area of the sensor.

$$i(t) = \varepsilon_0 E \times \frac{dA}{dt} \tag{5.2}$$

The theoretical amplitude of the field mill sensor is then calculated using the area, gain of amplifier and frequency. This calculation will be used later to compare with calibration results.

The induced current is sent through a charge amplification stage using a Toshiba isolation amplifier TLP7920 with up to 5 kV isolation voltage. This amplifier provides a Common-Mode Rejection Ratio (CMRR) of 80 dB which significantly reduces the common noise between the two ends of the differential signal. The oscillating voltage from the amplifier is then sent to the FPGA board with a built-in 15-bit ADC to digitize and record the waveform. By applying the Fourier Transform on the recorded waveform, the amplitude and frequency of the waveform is extracted, and magnitude of electric field is then calculated using the calibration data.

This setup has been calibrated by placing the sensor between two 1 m$\times$1.5 m aluminum plates which were separated by several 1 cm tall insulators. The maximum applied voltage across the plates was 3000 V which enabled us to measure external electric field magnitudes between 1 kV/m and 300 kV/m. Assuming the response of amplifier stays linear over its whole range of operation, this device can measure electric field magnitudes up to 1 MV/m. To avoid the field enhancement from charge build-up on the sensor, a hole in the center of bottom aluminum plate (ground) was made with the same diameter as the shutter plate, and the sensor location was adjusted to fit inside this hole and it would be leveled with the plate. This allowed us to minimize this enhancement effects and accurately calibrate the field mill sensor. The theoretical amplitude along with the calibration results are plotted in Figure 5.8. The difference between slope of two lines could be associated with errors in the effective area of sensor plate and gain variation of amplifier.

To determine the polarity of the measured electric field, the location of the shutter holes with respect to sensor plate was needed. For this purpose, an additional base was included on the side of the main platform to hold an IR laser (OPV332) and a Silicon PIN Photodiode (OSRAM, BPW 34). The OPV332 is a Vertical Cavity Surface Emitting Laser (VCSEL) packaged in a dome lens with an average wavelength of 850 nm. The dome lens packaging provides a narrow 4-degree beam angle from the device which minimizes the deflection of the light beam. The OSRAM photodiode

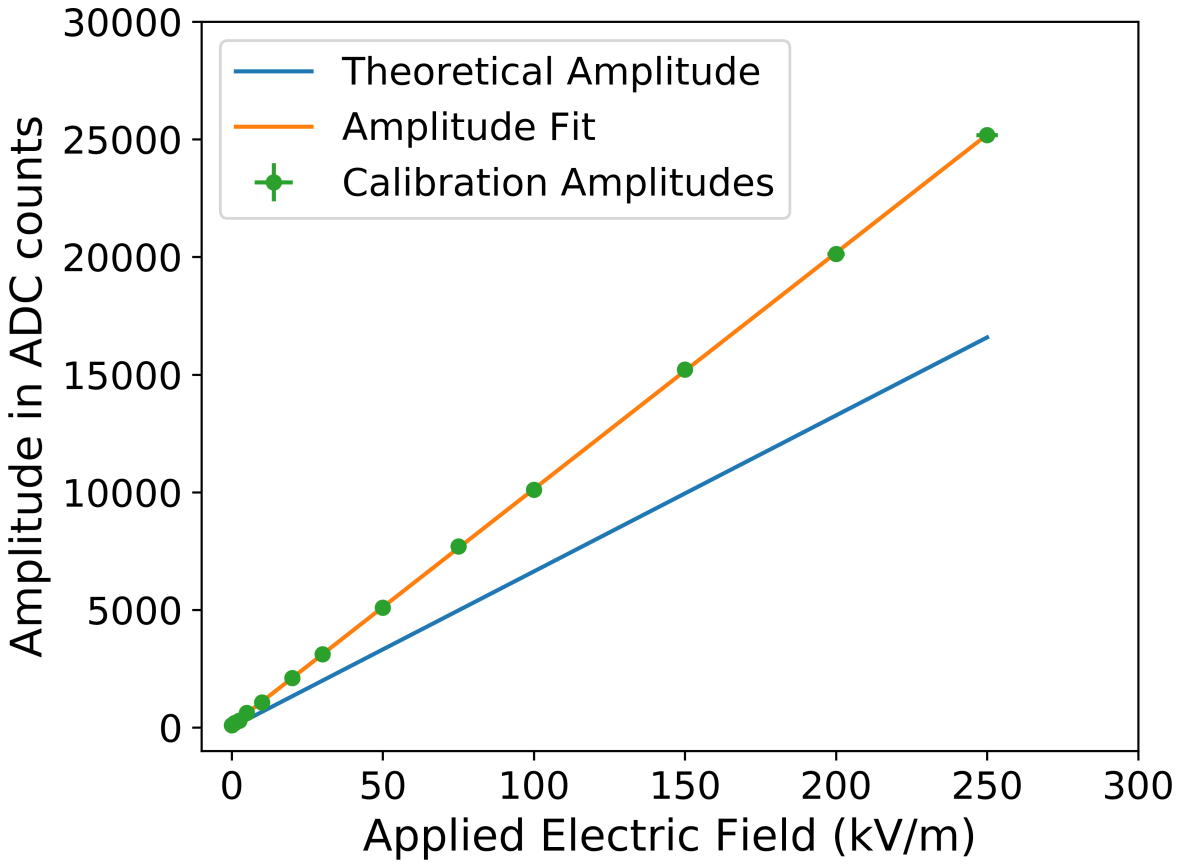

Figure 5.8: Amplitude of signal in ADC counts versus the applied electric field. The green points are the calibration points and blue lines represent the theoretical amplitude.

has a wavelength of maximum sensitivity of 850 nm which is optically and spectrally compatible with the chosen laser and maximizes the amplitude of the signal. IR laser and photodiode were mounted 5 cm away with an angle of 45 degree. During the operation, laser beam is being reflected from the back of shutter plate and emits through the photodiode. To maximize the reflection of the IR beam, back of the shutter plate was colored black with non-conductive paint. The signal from photodiode is sent through an amplification stage and a comparator, to produce a square wave output with a 3.3 V amplitude and similar frequency to electric field waveform. This setup enables us to record the azimuthal angle of the shutter with respect to sensor plate and determine which end of the differential signal (blue or red patterns) was exposed to the electric field lines during the

flight. By aligning the field mill and photodiode signal, we can determine the polarity of electric field.

5.2.4 Auxiliary Data

In addition to the instruments explained so far, there are three additional Peripheral Modules (Pmod) onboard including GPS, Real Time Clock (RTC) and Inertial Measurement Unit (IMU) (see Figure 5.9). All the Pmod devices were purchased from Digilent. The Pmod GPS uses the MediaTeK GPS MT3329 on a GlobalTop FGPMMOPA6H GPS antenna module to receive positional data over UART. By default, the Pmod operates using the National Marine Electronics Association (NMEA) protocols for data output from the GPS module. The interface operates at a baud rate of 9600 baud, with 8 data bits, no parity, and with a single stop bit. The led indicates the status of the user's positional fix. If the module has a constant fix (2D or 3D) this led stays low, but if the module is unable to get a fix then the led will blink every second. Pmod RTC provides real time clock and calendar module with battery backup capabilities. It communicates with the host board via I2C protocol and needs to be initialized with the GPS time during startup. The Pmod NAV uses the LSM9DS1 3-axis accelerometer, 3-axis gyroscope, 3-axis magnetometer, plus the LPS25HB digital barometer to provide users with 10-DOF functionality. Data from these devices are being monitored and recorded every second during the flight.

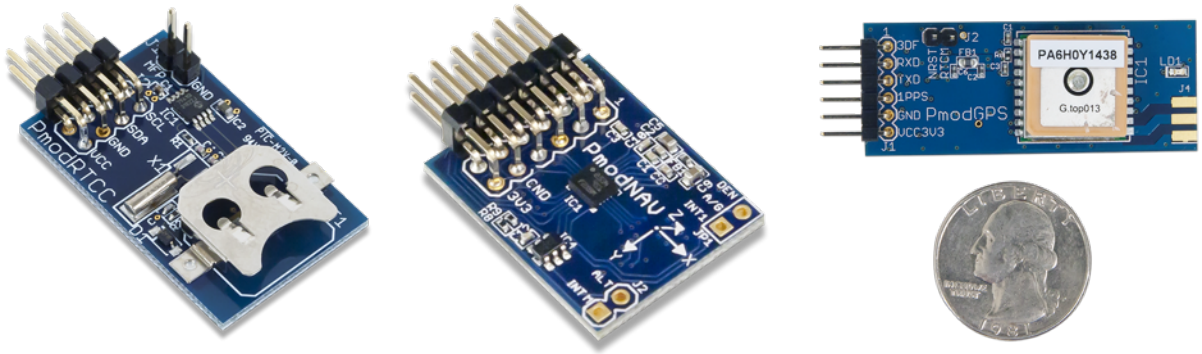

Figure 5.9: The image of Peripheral Modules including Real Time Clock (left), IMU (center) and GPS (right). RTC and GPS modules have backup battery capability.

5.2.5 Data Acquisition

We have developed and programmed our data acquisition on an Arty Z7-20 board. It is a ready-to-use development platform designed based on the Zynq-7000 All Programmable System-on-Chip (AP SoC) which integrates a dual-core, 650 MHz ARM Cortex-A9 processor with Xilinx 7-series Field Programmable Gate Array (FPGA) logic. The design process is very straightforward and provides a systematic path between defining your custom peripheral set and bringing its functionality up to a Linux OS running on the processor. The Arty board has Arduino/chipKIT Shield connector which provides up to 49 GPIO pins, 6 Single-ended 0 – 3.3 V and 4 differential 0 – 1 V inputs to XADC. The differential and single-ended inputs were used to read the field mill amplitude and SiPM bias voltage and temperature, respectively. The GPIO pins were used to communicate with the analog board of scintillator and Real Time Clock. In addition, the board provides two standard Pmod ports which were being used by the GPS and IMU sensors.

Programming of FPGA starts with a block design which is built inside Xilinx Vivado software. ZYNQ as the main physical processor is added to block design and one built-in Intellectual Property (IP) for each of GPS and IMU sensors is included. Another custom IP was developed in Verilog language to collect the count rate from GM tubes, pulse height from analog board of scintillator and amplitude of field mill sensor and integrate them along with time into three 32-bit integers. This IP samples the data every 26 μs ($\sim$ 38.4 kHz), allowing us to look at variation of electric field and radiation dosage with a high time resolution. These IPs are automatically wired to the processor through software. After data are collected from instruments on FPGA side, they are sent to the CPU side to be recorded on a SD card in binary format. This is done through Xilinx SDK platform, where we can manage the processor cores and program them individually. One of the CPU processors was dedicated to the reading data from FPGA and placing that into memory and the other was used to write them into SD card. During the read process, a software filtering was applied to eliminate the false triggers and reduce the size of data. The two cores were communicating through an IP called Mailbox which acted as a FIFO. Every 30 seconds of data ($\sim$ 15 MB) was written to a text file tagged with the GPS, IMU and RTC information.

5.2.6 Data Telemetry

The ground station installed on the roof of physics department at Florida tech utilizes two 900 MHz patch antennas with 60 degrees of vertical and 120 degrees of horizontal coverage, and one 900 MHz Omni-directional antennae to track and receive data from the balloons. This system is capable of tracking and receiving data from up to 3 flights simultaneously, allowing us to launch multiple balloons into a thunderstorm to map the radiation regions. We also used a 900 MHz 1W transceiver to transmit data to the ground station. There are two common baud rates, 9200 and 115200 bits per second, with a range of about 22 km and 11 km respectively. We used this system during the balloon campaign of summer of 2017, however it was found later that having an RF transmitter onboard payload could potentially interfere with the measurements of ambient electric fields, so we decided to stop data telemetry in the following summers.

5.2.7 Real-Time Tracking System

In addition to recording the location of the payload on the SD card, we have used two independent GPS tracking systems, as shown in Figure 5.10, to recover the payload immediately after landing. First one is an anti-theft tracking device called Spot Trace. Once Spot Trace is activated and powered on, it will acquire its exact coordinates from the GPS network and sends

Figure 5.10: Image of RockBLOCK Tracking System (left) and Spot Trace (right).

it to communication satellites. The satellites relay the message to a ground network, which uses the internet to route the message to mobile phone or computer. SPOT Trace allows us to monitor the payload and track its movement in near real-time via Google Maps. This device can transmit a location update as fast as every 2.5 minutes and it can operate up to 12 days with one 4-pack of AAA batteries. Second one is a custom designed system that utilizes an Iridium satellite communication module, called RockBLOCK, to send the coordinates to our website: `http://balllightning.sr.unh.edu/balloontracking`.

In this design, a microcontroller (Model# Teensy 3.6) retrieves the location data from GPS module (Model# Garmin 15x-w) every 5 minutes, then wakes up the RockBLOCK module and sends a message to satellite which is being received by ground network. This information is received via email and our website, where it plots the trajectory in real time and enables us to monitor the altitude as well. After the transmission is complete, RockBLOCK is sent to sleep to save battery. This design requires up to 470 mA at 5 V during startup and it uses about 70 mA during normal operation. In addition, location is being recorded on the SD card with a higher time resolution.

5.3 Balloon Launch Protocol

5.3.1 FAA Regulations

Although High Altitude Balloon (HAB) launches can be fun and educational, care must be taken to abide by the governing laws and regulations to ensure the safety of pilots and those that may be impacted by the launch and landing. Here is a summary of the applicable rules and regulations that apply to your weather balloon.

1. Cell phones are not permitted to transmit in flight on high-altitude weather balloons.

2. You may not launch a high-altitude weather balloon which creates a hazard to other people and property.

3. Payloads cannot exceed a package weight/size ratio of three ounces per square inch. You can determine this by dividing the total package weight by the area in square inches of the smallest surface.

4. No payload package may weigh more than 6 pounds.

5. The entire weight of all payloads cannot exceed 12 pounds in total weight. This does not include the weight of the balloon.

6. No one may use a high-altitude weather balloon to drop objects.

Operators should consider notifying local air traffic facilities as a courtesy if the balloons are launched near an airport, in a populated area or if multiple balloons will be launched from one location. In addition, the burst alttiude of the payload should be set under 15 km to avoid any danger for nearby airplanes.

5.3.2 Balloon Launch Parameters

Balloons are rarely perfectly spherical; however, a sphere is used to approximate its volume here. There are several forces acting on an ascending balloon carrying a payload including the downward gravitational force, the upward buoyant force and the drag force which are given by Equation 5.3, 5.4 and 5.5 respectively.

$$F_G = \frac{4}{3}\pi r^3 \rho_{gas} g + (M_{payload} + M_{balloon})g \tag{5.3}$$

$$F_B = \frac{4}{3}\pi r^3 \rho_{air} g \tag{5.4}$$

$$F_G = \frac{1}{2}\rho_{air} v^2 C_D A \tag{5.5}$$

C_D is the drag coefficient ($\sim$ 0.25), r is the radius of the balloon and A is the reference area (2D cross sectional area). As the balloon is ascending with a constant velocity of v, the net force on the

system should be equal to zero which requires $F_B = F_G + F_D$. Solving this equation for v, results to an ascent rate given by Equation 5.6.

$$v = \sqrt{\frac{[\frac{4}{3}\pi r^3(\rho_{air} - \rho_{gas}) - M_{payload} - M_{balloon}]g}{\frac{1}{2}\rho_{air} C_D A}} \tag{5.6}$$

We have used Kaymont HAB-350 latex balloons ($M_{balloon}$=350 grams) during this campaign. The maximum allowed mass of the payload is 6 pounds ($\sim$ 2.7 Kg), however the total mass which includes the strings, swivel, parachute and flashlight could increase the $M_{payload}$ up to 3500 grams. This additional weight is still in agreement with FAA regulations, as long as the payload itself does not weight more than 6 pounds. Density of the air and Helium are 1.225 and 0.179 kg/m^3 respectively. By filling up the balloon to a radius of 1.12 m, the calculated ascent rate will be about 6.1 m/s. This is equivalent to a burst altitude of 13 km and a burst time of 35 minutes which requires about 216 ft^3 of Helium gas.

Four upper corners of the payload are connected to the parachute via 15 ft long strings and parachute is attached to the neck of balloon via a 6 ft long string. A double round eye swivel was used between the parachute and balloon to avoid the twisting of the strings. After the balloon bursts, parachute activates and carries the payload back to the ground. The descent rate depends on many parameters including the weight of the payload, surface area of the parachute and air density. Figure 5.11 shows the calculated descent rate versus payload weight for two common size of Rocketman parachutes. For a 4 ft and 5 ft parachute carrying a 6 pounds payload, descent rates of about 6.8 m/s and 5.4 m/s were calculated. This would result to a descent time of 35 minutes and 45 minutes. For the final configuration of the launch, a 4 ft parachute is recommended.

5.3.3 Flight Path Prediction

To anticipate the trajectory of the payload during the flight, we have used the predictor of habhub.org website to determine the burst and landing locations. The required inputs are Latitude/Longitude/Altitude of launch location, launch time in UTC, ascent rate, burst altitude and descent rate. This predictor utilizes the wind profile at different altitudes to anticipate the trajec-

tory and works to a very high accuracy during the fair-weather condition. However, during the thunderstorm weather, it is not fully reliable and there are large margins of error.

5.3.4 Payload Recovery

The payload retrieval team must be notified prior to the launch to facilitate a successful recovery. Prior to the launch is identified as a minimum of 1 hour. This team was made up of at least two members. Each member of this team will be equipped with a balloon retrieval kit and must wear clothing identifying them as FIT students and/or GPL employees. Additionally, all tracking apps and software must be preinstalled on recovery team member's phones and laptops. This kit is designed to recover payloads from different environments including river, swamp, rural, residential and ocean. Protocols need to be devised to address how to approach retrievals based on the landing environment. Once payload is located by the retrieval team, contact must be made with

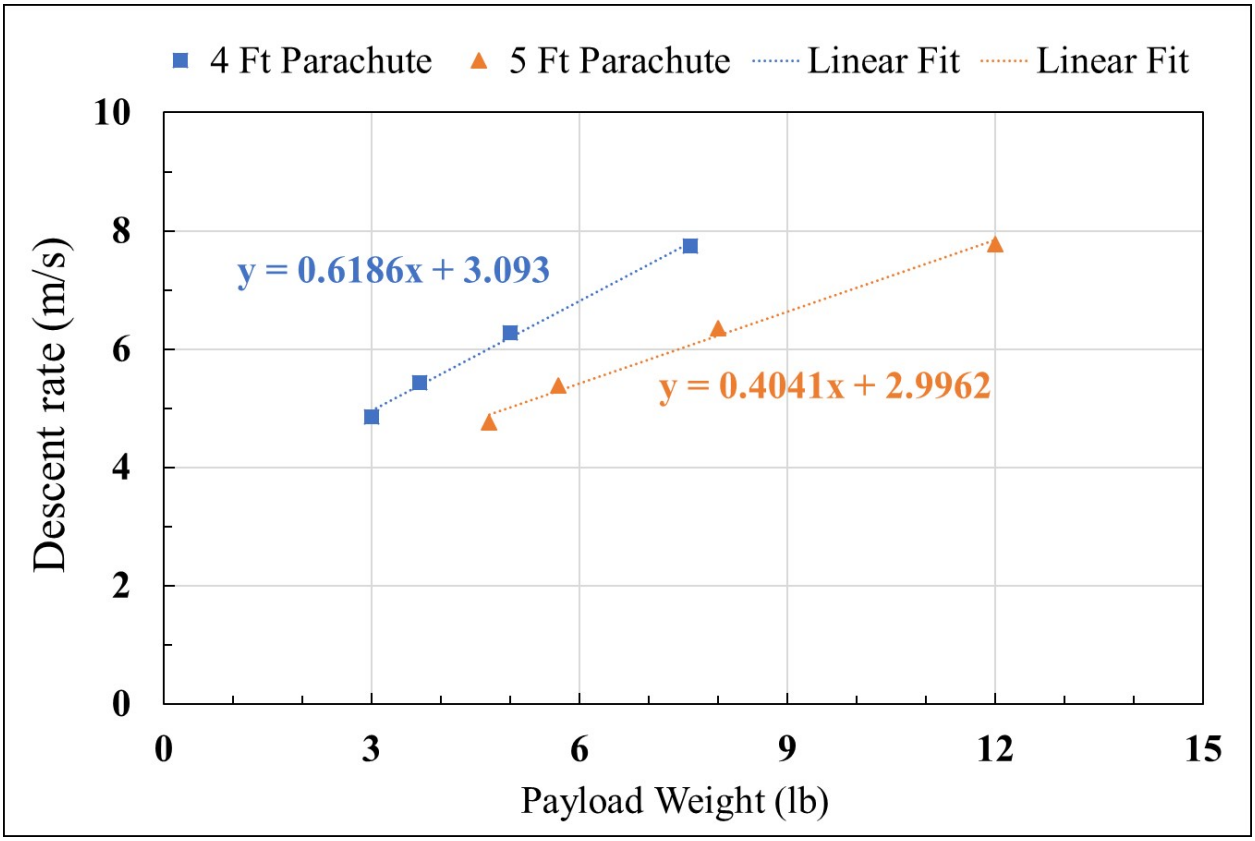

Figure 5.11: Calculated descent rate versus payload weight for 4 ft and 5 ft parachutes. With a 6 pounds payload, a descent rate of 6.8 m/s and 5.4 m/s will be achieved respectively.

the appropriate FIT staff. This will indicate an attempt to retrieve payload.

Swamp Recovery

- Survey surrounding area, indicating brush density and location relative to main roadway.
- Use a tool to measure swamp depth. If no more than ankle deep, recovery can be attempted assuming that swamp location is not isolated.

River Recovery

- Determine location in river relative to closest intersecting main road.
- Attempt to make visual confirmation from closest shoreline.
- If payload is stationary in river (caught on debris or near an island), a kayak retrieval can be attempted, otherwise contact FIT boathouse and inquire about using a boat for retrieval.

Ocean Recovery

- Determine relative distance from shoreline and closest intersecting beach.
- Monitor payload to see if current is driving it inland.
- If no indication is made that payload will be retrievable from land, contact FIT boathouse and inquire about boat rentals.

Residential Recovery

- Attempt to contact property owner.
- Identify yourself as a FIT student researcher.
- Recover payload. It is advised that members of the recovery team carry a small amount of cash in case of minor property damage.

- Note property owner, their contact information, address, time of day, and FIT representative meeting with property owner.
- If major property damage occurs, contact the relevant FIT personnel immediately.

Highway/Roadway Recovery

- Attempt to recover at safe time, observe all traffic patterns.
- If major property damage occurs or injury has occurred, contact the relevant FIT personnel immediately.

5.4 Flight Results

5.4.1 Summer of 2017

During the first year of the balloon campaign, several tasks were accomplished including: 1) Upgrading the microcontroller codes to increase the speed and stability of data acquisition, 2) Fixing some issues in the circuitry design of the boards, 3) Design and calibration of field mill sensor, 4) Design and development of RockBLOCK tracking module and its website. At this time, the instruments onboard included two Geiger counters separated by a lead sheet and a field mill mounted on the bottom of box. The total weight of payload was 4 pounds. In overall, three payloads were constructed and launched multiple times during six flights as listed by Table 5.2. Two more additional payloads were prepared to be launched during the possible fall thunderstorms

Launch Date	July 14	July 17	July 18	July 21	July 28	Sep 2
Weather Condition	Fair weather	Thunderstorm	Thunderstorm	Thunderstorm	Fair weather	Fair weather
Flight Duration	2 hours	1 hour and 15 minutes	5 hours	4 hours	2 hours	1 hour and 20 minutes
Burst Altitude	23 km	14.5 km	Not available after 7.2 km	Not available after 8 km	N/A	17 km
Recovery Status	Recovered with data	Recovered with data	Recovered with partial data	Recovered with partial data	Recovered NO data	Recovered with data

Table 5.2: List of balloon launches with flight details during the summer of 2017.

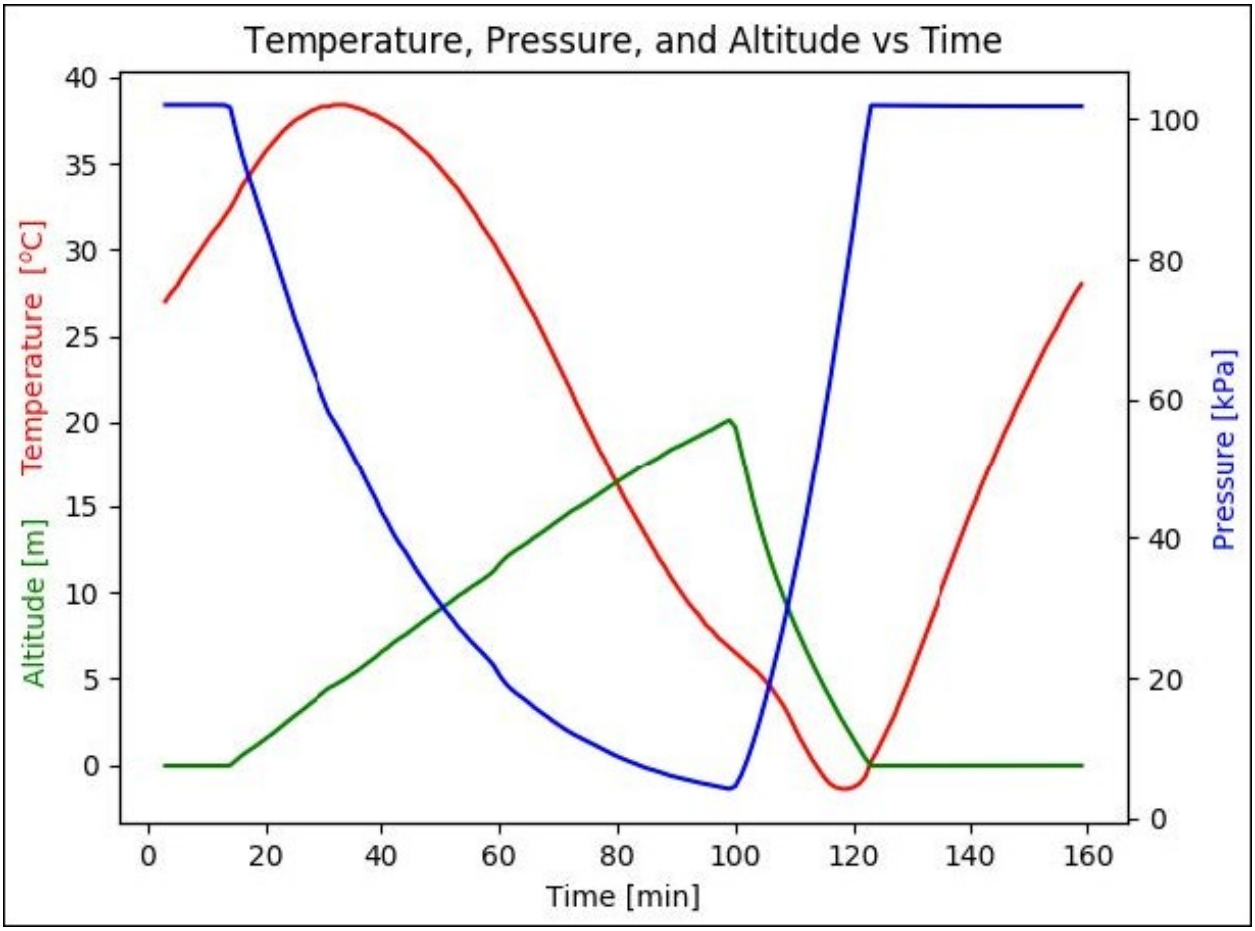

Figure 5.12: The auxiliary data (Pressure, Temperature and Altitude) versus time of flight measured during the fair-weather flight at July 14, 2017.

but were never flown due to lack of lightning activities. 1^{st} launch was performed during fair-weather activity on July 14, 2017. This flight took about 2 hours with a burst altitude of 23 km and was successfully recovered. No significant enhancement was measured above the background; however, the pressure and temperature profile were measured which are shown in Figure 5.12. Note that temperature lags pressure due to the fact that the measurements were made from within the insulating foam container.

During the 2^{nd} flight on July 17, payload traveled near an active thunderstorm cell with high-field regions nearby. The KSC LMA data showed that payload moved towards north with an active cell on the west side of balloon trajectory as shown by Figure 5.13. The main activity of the storm was between altitudes of 5 to 10 km. The total flight time was about 1 hour and

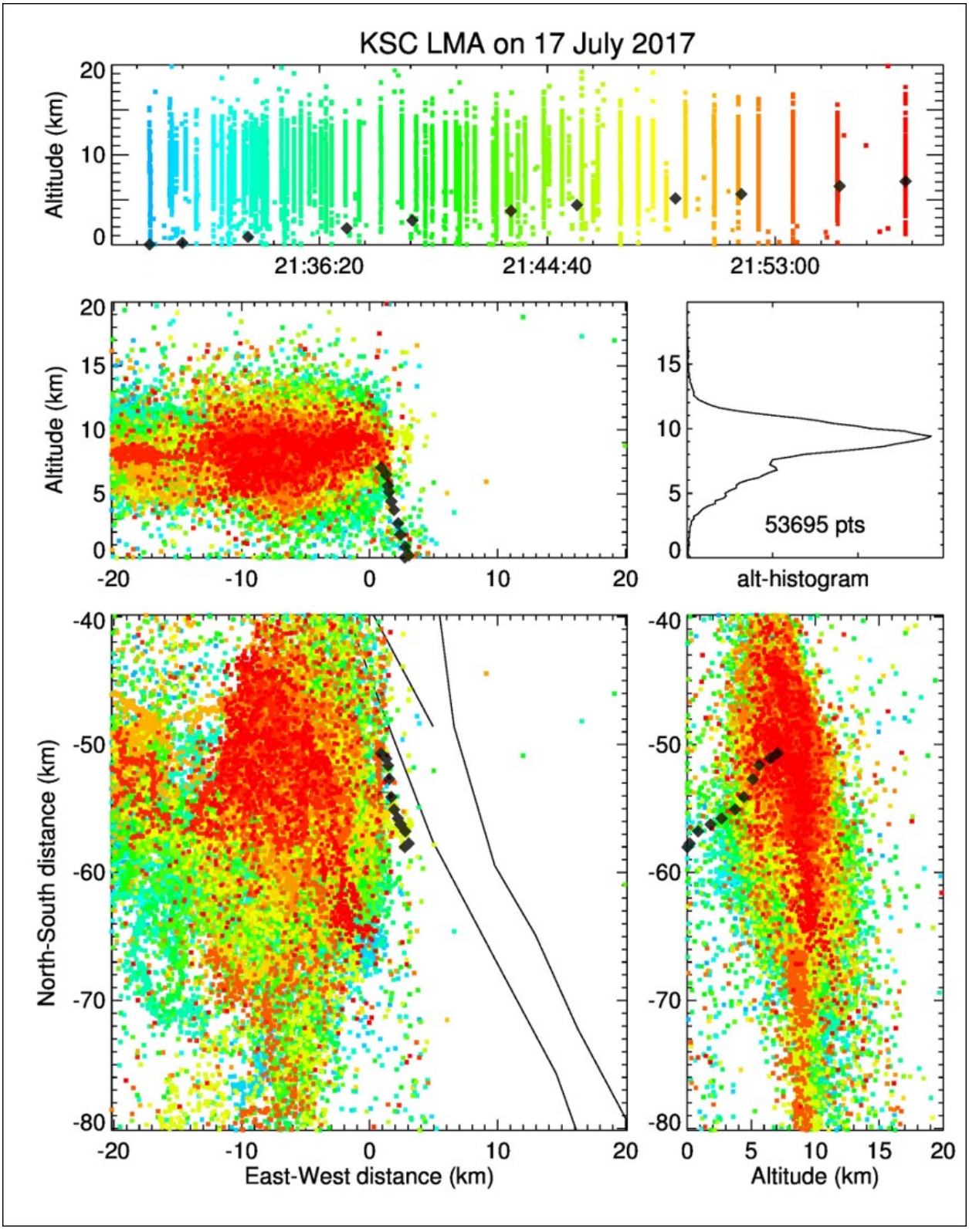

Figure 5.13: KSC LMA data during the balloon flight at July 17, 2017 with nearby thunderstorm.

15 minutes with a burst altitude of 14.5 km, but after about 30 minutes the data acquisition was interrupted due to an unknown reason. There is this possibility that payload was struck by a lightning discharge and power was lost or turbulent weather have disconnected the batteries. Given that in the first 30 minutes of the flight payload reached an altitude of 5 km, where most of the lightning activities were occurring, we expected to observe some enhancement in the electric field measurements. An example of measured electric field amplitude versus time is shown in Figure 5.14. This measurement was done between 21:40 and 21:50 UTC, when the payload altitude was between 2 to 3 km. As the waveform reveals, the high frequency noises were minimized by using an ADC with common-mode rejection feature. The peak amplitude was found to be about 700 kV/m based on the calibration, however it was noticed later that the mechanical design of the field mill might have caused unrealistic enhancement which affects both the calibration and actual measurement of ambient electric field. The distance between the sensor plate and shutter is a very important parameter which can significantly affects the measured electric fields. In addition, the shutter plate needed to be leveled with the surrounding ground plane to not affect the penetrating field lines.

There were three additional balloon launches on July 18, 21 and 28 which during all of them the data acquisition was interrupted due to several reasons. On July 18, due to some issues with the GPS lock, the GM tubes data acquisition was interrupted after about 7 km which also made the electric field measurement difficult to interpret because of not knowing the time and location. On July 21, payload started to lose altitude at about 8 km before reaching burst altitude due to helium leakage from the balloon and descended very slowly. The slow descent rate increased the overall flight time to about 4 hours. There was also no GPS information during most of the descent which did not allow us to correlate most of the measurements with actual events. During this flight, there was a power loss during which the data was partially overwritten, however this problem was taken care of in later flights. On July 28, due to the severe winds at the time of launch, we lost communication with payload in the first kilometer and unfortunately there was no data available

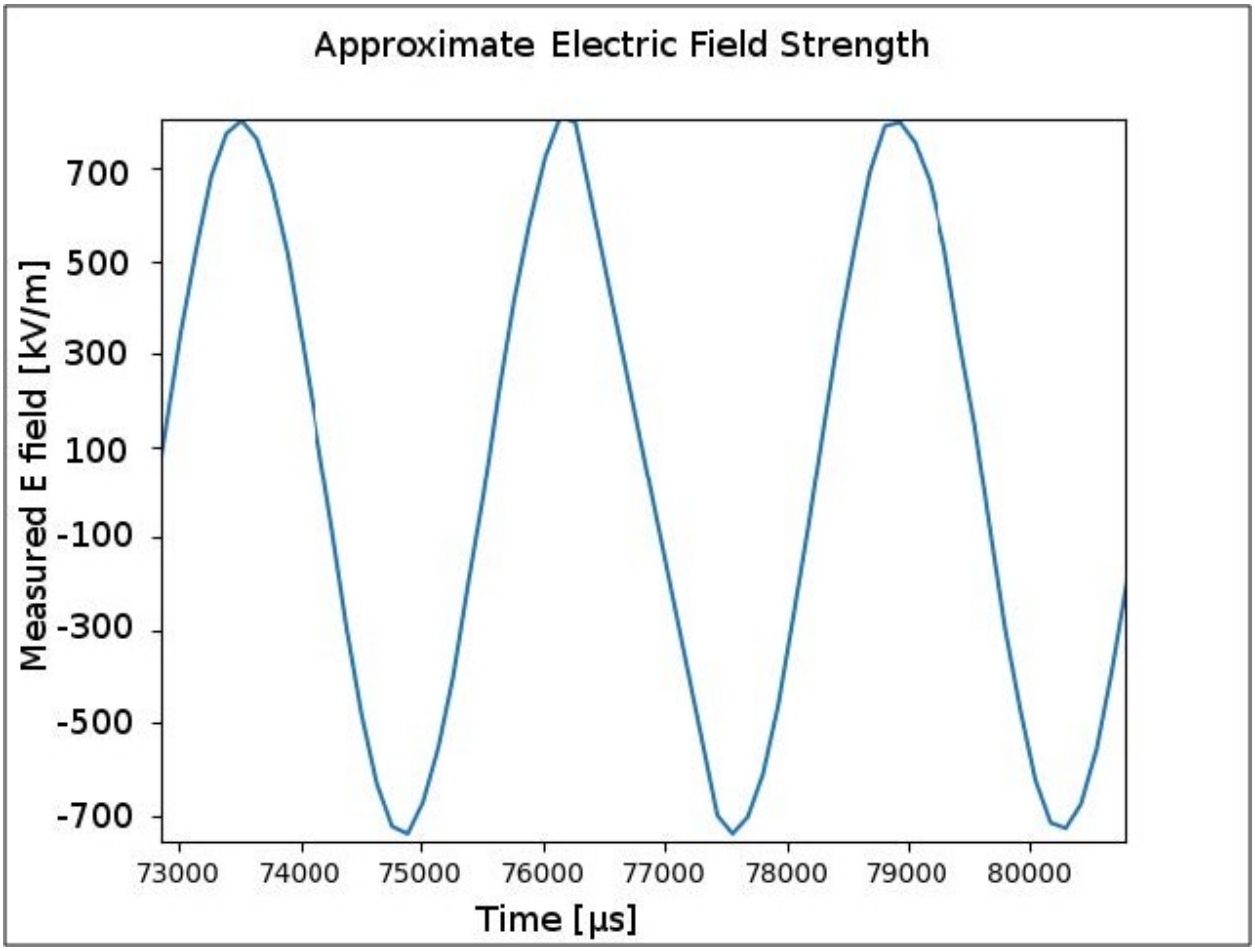

Figure 5.14: The measured electric field during the thunderstorm activity on July 17, 2017.

from this flight. In overall, these three partially successful flights helped us to determine and solve several possible issues.

After re-programming the GPS device and modifying the flight parameters, the last flight of this summer was performed on September 2, 2017. Payload reached a burst altitude of 17 km with a total flight time of 80 minutes. Given that there was no thunderstorm nearby, electric field measurements matched with the fair-weather profile. Both of GM tubes measured similar count rates versus altitude which is shown in Figure 5.15. The count rates during ascent and descent matched with background rate from cosmic rays, reaching to a maximum of about 50 counts/second at 17 km. In overall, we were able to design, calibrate and test our instruments during both fair-weather and thunderstorm by the end of summer.

5.4.2 Summer of 2018

Prior to the 2^{nd} summer of balloon campaign, payload instrumentation was upgraded in several aspects. The lead sheet between the GM tubes was replaced with a BGO scintillation detector, where the light pulses were detected with a Silicon Photomultiplier. An analog board was designed and tested for the readout of the SiPM and pulse height calibration with temperature compensation was performed. The field mill circuitry and sensor plates were redesigned and calibrated. We moved our data acquisition system from Arduino microcontrollers to Xilinx FPGA devices to improve the data collection speed and timing. Given that any device transmitting radio waves can concentrate the electric field lines inside thunderclouds and interfere with the electric field

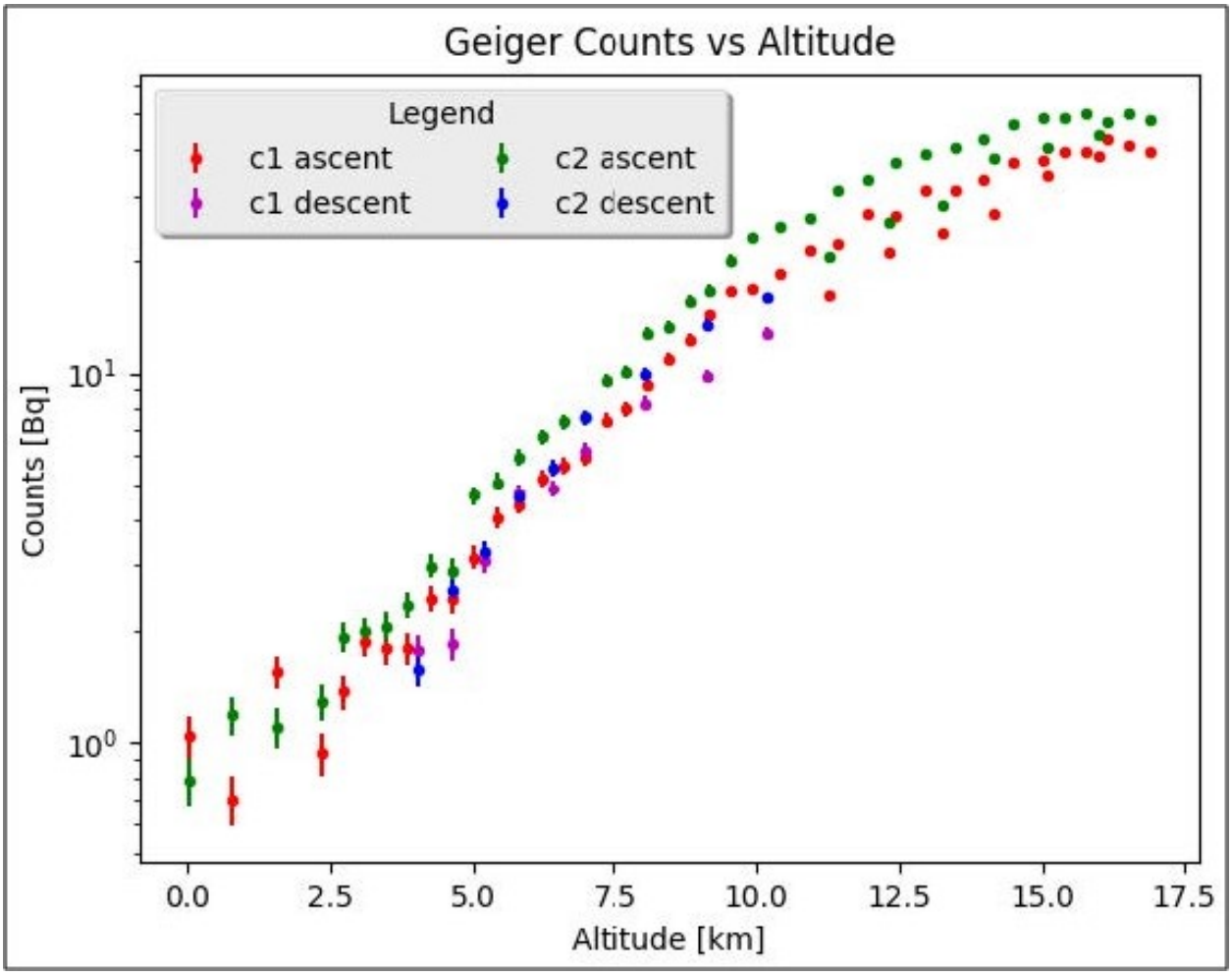

Figure 5.15: The measured count rate of GM tubes versus altitude during the fair-weather flight at September 2, 2017.

Launch Date	July 22	July 25	August 12	August 24
Weather Condition	Fair weather	Thunderstorm	Fair weather	Thunderstorm
Flight Duration	Unknown	5 hour	1 hours	1 hours
Burst Altitude	Unknown	Unknown	13 km	15 km
Recovery Status	Lost in ocean	Lost in ocean	Recovered	Recovered with data

Table 5.3: List of balloon launches with flight details during the summer of 2018.

measurements, the RF transmitter was removed from the payload. In addition, the Styrofoam box was covered with a sheet of aluminum foil connected to the ground of our electronics. This way the surrounding of shutter plate of field mill would be at the same voltage as the ADC ground. A detailed list of balloon launches performed during summer of 2018 is given in Table 5.3.

1^{st} balloon payload was launched on July 22, 2018 at fair-weather condition. Unfortunately, due to complete isolation of the Styrofoam box with aluminum foil, the box acted as a faraday cage and blocked all outgoing GPS signals which disabled us from tracking and recovering it. This incident made us to redesign the shielding of next payloads by placing a conductive surface inside the box above other instruments, connecting that to the exterior shielding with a wire and mounting the GPS antennas above that surface. This way all of instruments were still isolated, but GPS antennas were able to communicate with satellite. The 2^{nd} payload was launched three days later on July 25, 2018 at 5 pm with active cells of thunderstorm coming from west. The path prediction software anticipated a trajectory towards North-East with a burst altitude over the ocean, a total flight time of 1 hour and landing point about 40 km off the coast. Given that this was our first balloon launch with a 6 pounds payload, the calculated launch parameters did not match well enough with actual experiment which allowed the payload to travel towards North-East farther than expected. The payload landed on ocean at a diagonal distance of 160 km from FIT campus with a total flight time of 5 hours. There was a boat following the payload during the first 2 hours of the flight, however captain decided to cancel the recovery after realizing that payload is too far from the coast. We think that the balloon never burst and started to lose altitude very slowly which is the reason for the long flight time. Based on the meteorological data and tracking information, this payload traveled very closely to the active thunderstorm region and could have

recorded valuable data from inside the thundercloud, however it landed too far for any boat to recover it. The batteries onboard allowed us to track the payload for almost 12 days after which we lost its location. In order to minimize the margins of error in the path prediction, we decided to re-calculate the launch parameters from scratch and quantify our launch system accurately. These calculations are reported in Section 5.3.2. A test flight was performed on August 12, 2018 during fair-weather to confirm the accuracy of calculations. The payload box was filled up with bottles of water and a Spot tracker device up to 6 pounds and the balloon was filled up to 2.2 m in diameter. The flight took about 1 hour which agreed with our calculations and landed near the predicted locations. Since payload was landed on the ground, we were able to recover it without hassle. These launch parameters were used for the later flights during the campaign to avoid long flight times and achieve a landing location near the FIT campus. Last balloon launch of this summer was performed at 20:32 UTC on August 24, 2018 which lasted about 55 minutes, burst at 15 km and payload was recovered afterwards successfully. The prediction system anticipated a trajectory towards east with landing point on the Indian river, as shown in Figure 5.16.

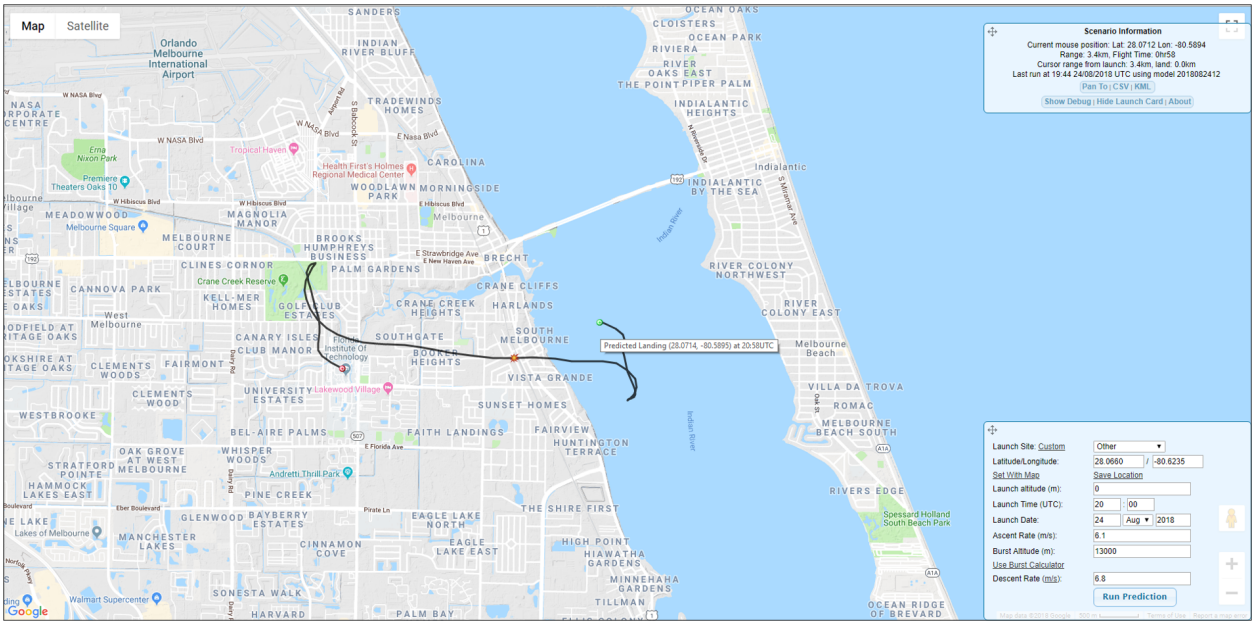

Figure 5.16: The predicted trajectory of the payload using the predict.habhub.org with a launch time at 20:00 UTC on August 24, 2018. The total flight time and landing location was very close to actual flight.

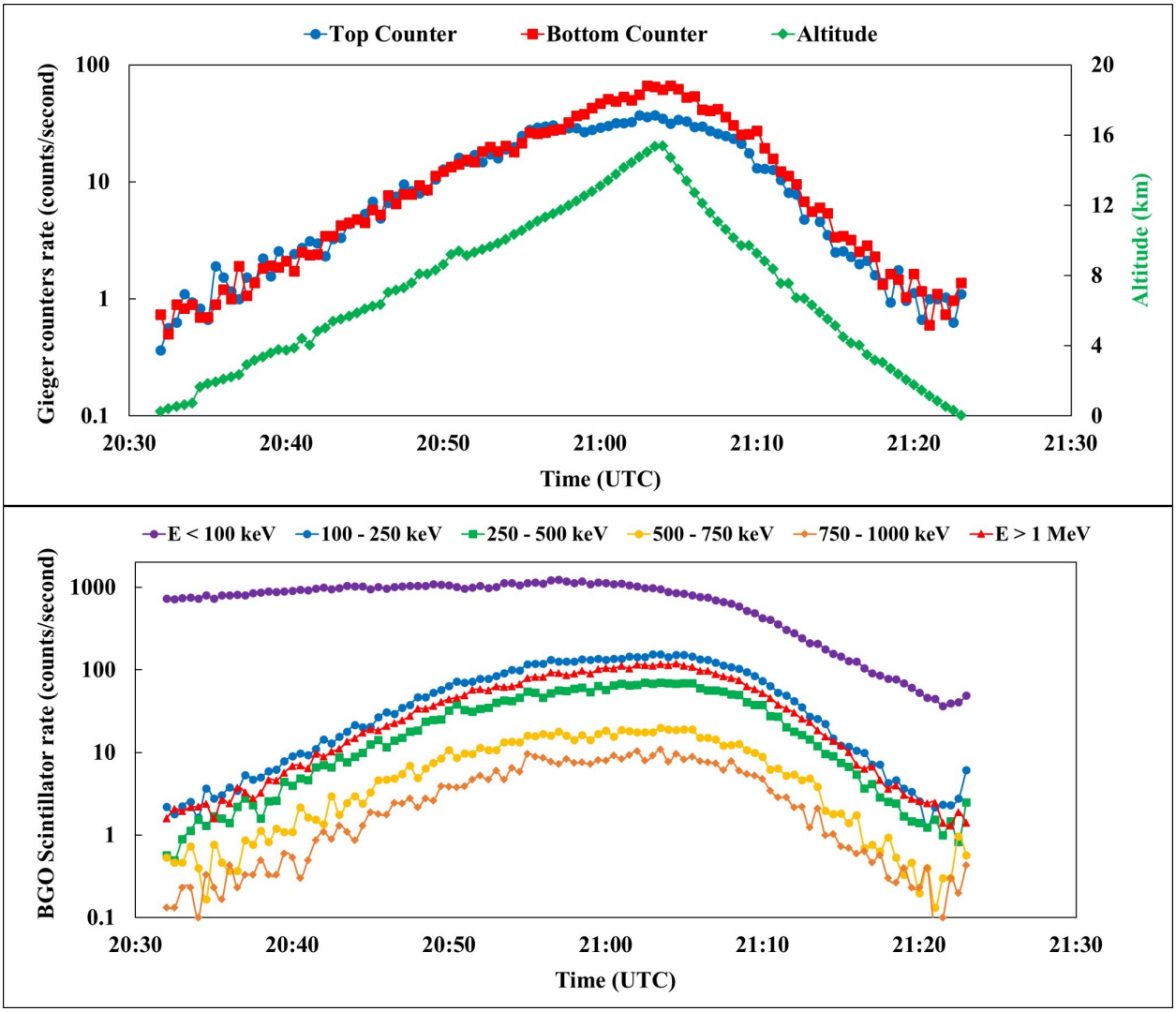

Figure 5.17: Measured count rates of two Geiger tubes (top) and scintillator in 6 energy channels (bottom) versus time (UTC). The observed enhancement in the bottom counter was due to higher gain and temperature sensitivity of the tube and no actual glow seems to be observed.

Figure 5.17 shows the measured count rate from GM tubes and BGO scintillator versus time along with the altitude profile. The scintillator energy channels were selected as following: $E < 100$ keV, 100-250 keV, 250-500 keV, 500-750 keV, 750-1000 keV and $E > 1$ MeV. During the ascent, both GM tubes measured similar count rates until 10 km (20:53 UTC), where the bottom tube started to observe an enhancement. This enhancement continued to grow and reached an increase rate of 100% at the burst altitude and then started to fall off during the descent. It eventually disappeared at about 8 km (21:10 UTC). By looking at the Table 5.1, this type of enhancement

agrees with an upward electron/positron beam, however it requires large fluxes of particles during that time period in the scintillator data as well. Given that sensitivity of BGO crystal is high enough for both gamma rays and charged particles, if the payload had passed through an energetic beam of charged particles, it was expected to be seen as an enhancement at least in one of energy channels, however that did not happen. There could be two reasons for such behavior. First, the observed enhancement in the bottom tube was caused by a low-energy beam of electrons which was dominated by the background and dark current at $E < 100$ keV band of scintillator. This seemed unlikely given that a low-energy beam of charged particles is expected to be produced isotopically and would have no preferred direction. However, the observed beam was mostly directed upward. Second, the bottom tube might have had issues with the atmospheric conditions. To investigate this issue, we tested both of the GM tubes under similar atmospheric conditions as 10 km altitude (low temperature and pressure) with a Cs-137 radioactive source to find out if this was the case. It turns out that as the temperature drops below 5 °C, the bottom tube produces additional pulses a few microseconds after the main pulse which were being counted as extra events, however we were never able to reproduce the exact enhancement pattern as seen during the flight. We believe that the enhancement observed in the bottom tube was due to the dependency of the gain on temperature and no actual gamma-ray glows were observed.

Figure 5.18 shows the measured electric field profile versus time (top panel) and 10 ms of the recorded waveform with the highest amplitude (bottom panel). During this flight, payload entered through three main high-field regions at altitudes of 9.3 km and 13.4 km (during ascent) and 6.1 km (during descent). In the first region, electric field reached to its peak amplitude ($\sim$ 150 kV/m) very quickly, lasted about 5 minutes and was terminated in less than a minute. It is possible that this sudden termination is caused by several lightning discharges. On the other hand, the electric field amplitude at the second and third region increased gradually, reaching to peak amplitudes of 100 kV/m and 250 kV/m and lasting about 2 minutes and 5 minutes, respectively. The gradual increase and decease of electric field suggests that the payload left the high-field area before the ambient field would be discharged completely. Note that we have used an automated Fourier transform to

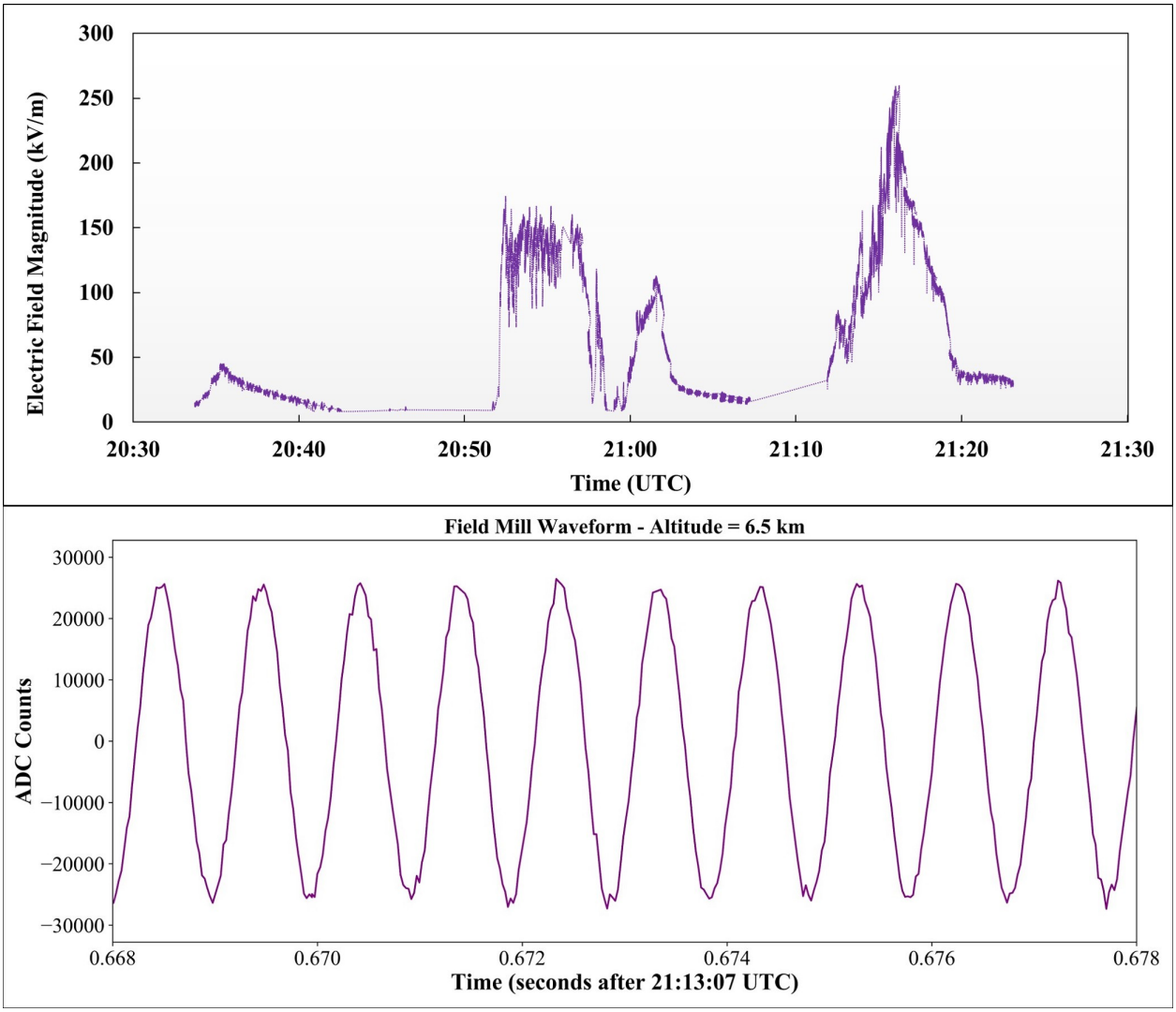

Figure 5.18: The electric field magnitude versus time (top) and an example of recorded waveform from field mill (bottom) during the balloon flight at August 24, 2018.

retrieve the amplitude of electric field from waveform, and whenever the waveform is the same order of magnitude as noise level, the amplitude was considered zero which is the reason for flat lines in the electric field profile.

One great challenge with the in-situ measurement of electric field inside thundercloud is charge build-up on the balloon and payload box. This excess charge can potentially produce corona discharges and interfere with the ambient electric field which significantly increases the measured electric field. In this flight, the maximum amplitude of the electric field was measured at 6.5 km during descent ($\sim$250 kV/m) which is equivalent to an electric field magnitude of 500 kV/m at sea

level. Since this field is significantly higher than the runaway threshold, it is possible that excess charge on the payload have enhanced the actual field. As a matter of fact, aircraft measurements of thundercloud electric field have shown that charge build-up can enhance the background field up to two orders of magnitude, so these effects needs to be considered in order to retrieve the correct amplitude of electric field. Unfortunately, we are not able to confirm that the electric field reported here are directly caused by charge build-up, however such affects could be avoided in future by including a second field mill sensor on top of the payload. This way if the charge build-up is enhancing the ambient field, average of those two independent measurements would give us the correct amplitude of background electric field.

The KSC LMA data for the total duration of the flight is shown in Figure 5.19. Lightning activates were mostly occurring between altitudes of 5 km and 12 km (top panel). As showed earlier, during the first two electric field enhancement events, balloon was at altitudes of 9.3 km and 13.4 km, where multiple lightning flashes were occurring nearby (mostly green and yellow dots on the map). As the payload reached to the top of the active region, the balloon burst, and electric field amplitude reduced. On the way back to the ground, payload went through the same active region (orange dots), where again lightning flashes were occurring nearby. In overall, it seems payload passed through an active region twice with nearby lightning discharges and electric fields with very high amplitudes were measured.

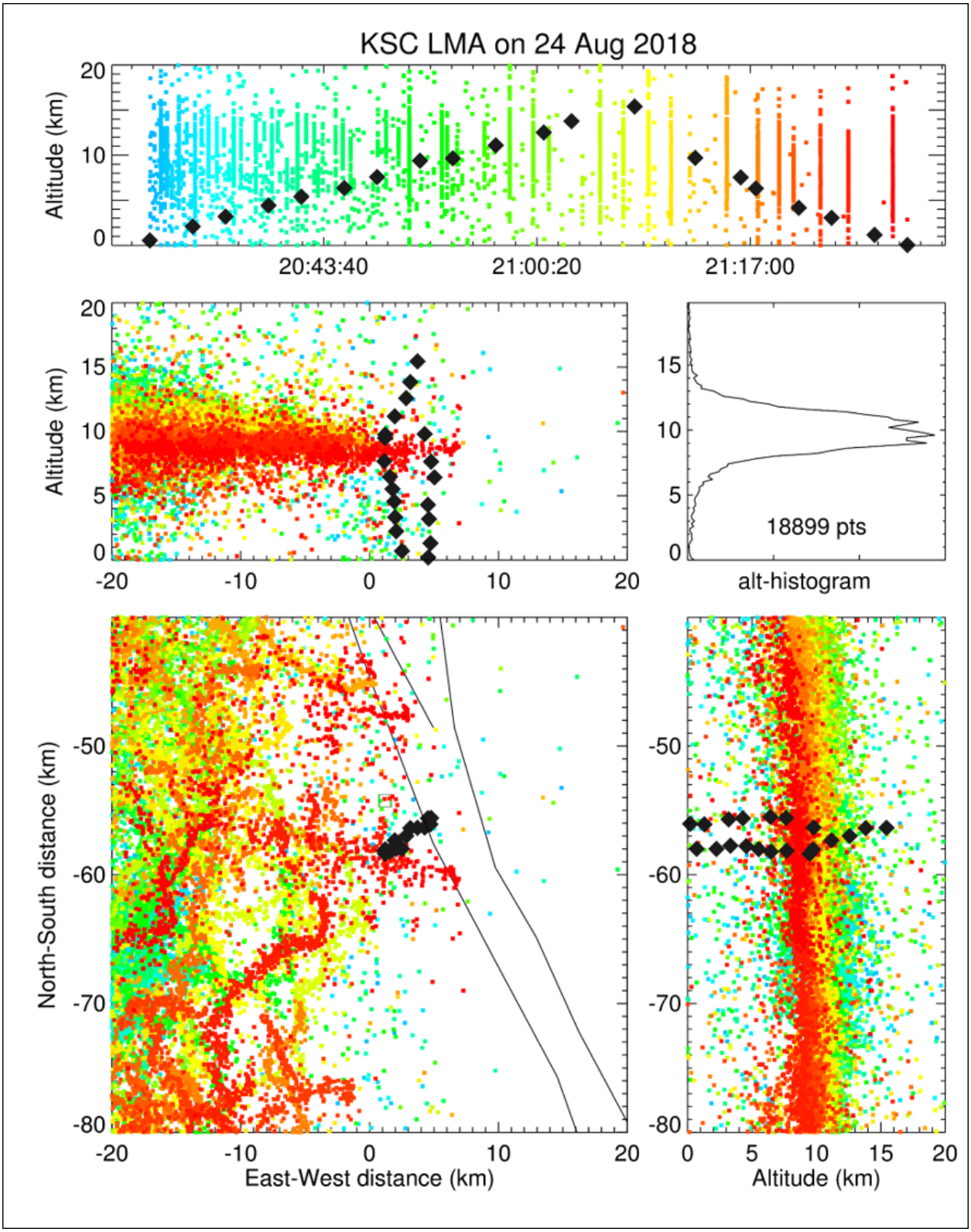

Figure 5.19: KSC LMA data during the balloon flight at August 24, 2018.

CHAPTER 6

SUMMARY AND FUTURE WORK

6.1 Summary

The materials provided in this dissertation is aimed to improve our knowledge of lightning physics and associated radiations produced during lightning activities, such as runaway electrons, TGFs, X-rays and Gamma-ray glows. This research investigates both theoretical and observational aspects of lightning physics in planetary atmospheres including Venus and Earth. Furthermore, Several Monte Carlo simulations were performed to characterize the source geometry and temporal properties of runaway electrons and TGFs. Finally, a series of instruments were designed, calibrated and launched into thunderstorms to measure gamma-ray glows.

Recent observations by Venus Express and Pioneer Venus have recorded signals attributed to lightning discharges in the Venus clouds. We used the Runaway Electrons Avalanche Model (REAM) to simulate the generation and propagation of runaway electrons and gamma-ray flashes through Venus middle and upper clouds. Results from avalanche length and energy spectrum of runaway electrons showed that Venus middle clouds and Earth sea level have almost the same runaway electron properties, which leaded to the same threshold electric field. It seems if electrification occurs in the clouds of Venus, and the gamma-ray flashes initiate in the middle and upper clouds are similar to that on the Earth, they should be detectable by spacecrafts at low-Venus orbit. We proposed calling these events Venusian Gamma-ray Flashes (VGFs). This work has been published in the Journal of Geophysical Research: Space Physics *[Bagheri and Dwyer, 2016]*.

Even though TGFs have been detected more than two decades ago, it has been difficult to disentangle the source altitude and the width and direction of the gamma-ray beam using single point spacecraft measurements. Polarimetry has been used widely to characterize astrophysical sources

which raises the question: Do TGFs and X-rays from lightning have observable polarization, and if so, what would this polarization tell us about their source? By modifying the REAM Monte Carlo code, we have recorded the linear polarization of X-rays and gamma rays as a function of source altitude and beam geometry. It was found out that mid-altitude TGFs could be polarized as high as 10%, but because only a few tens of counts are typically detected by spacecraft, detecting this level of polarization is unlikely. Furthermore, very low-altitude ground-level TGFs produced during rocket-triggered lightnings showed a maximum polarization of 13% on the ground, with the TGF's fluence was large enough for polarimetry. The dominant mechanism of the polarization was found to be Compton scattering. This work is currently under revision in the Journal of Geophysical Research: Space Physics *[Bagheri et al., 2019]*.

Temporal properties of TGFs has been changed significantly since their discovery and can be used to discriminate between models of the origin of TGFs and provide some basic physical properties of the TGF process. We have investigated the effect of beam geometry, source altitude and distance between the source and satellite on the spectral and temporal distribution of TGFs seen in space. It has been shown that t50 parameter is increasing with off-axis distance and source altitude, while having a higher cut-off energy reduces the t50 of TGFs. In addition, the incompressible time dispersion caused by Compton scattering for a wide and instantaneous source is about 20 μs at 300 km distance which is about 2.5 times smaller than was it was thought before. Then, if TGFs are produced by fast processes such as stepping of lightning leaders, it is possible that their duration would be much shorter than 50 μs proposed by earlier Fermi measurements. These results are currently under preparation to be submitted to JGR: Space Physics.

One of the greatest unsolved problems in the atmospheric sciences is explaining how lightning initiates inside thunderstorms. It is an interesting question whether or not the enhanced flux of energetic electrons and gamma rays plays some role in the lightning initiation process or if the gamma-ray glow is instead just a useful tracer of the strong electric fields required for lightning initiation. We have designed balloon-based instrumentation for flying into thunderstorms with the aim of detecting such radiation. The instrumentation includes one BGO scintillator coupled to

a Sensl J-series Silicone Photomultiplier, two Geiger-Muller tubes, and a low-power lightweight electric field mill, designed and calibrated to measure both polarity and amplitude of the vertical electric field inside the thunderstorm region. The insertion of scintillator between two GM tubes along with the electric field's polarity helps us to differentiate between gamma rays, electrons and positrons. We have conducted several test flights of this system during the summers of 2017 and 2018 and their result were provided. The preliminary results of this balloon campaign were presented at AGU Fall meeting of 2017 and 2018.

6.2 Future Work

During the last two summers of our balloon campaign, we have redesigned several aspects of the payload to overcome the challenges with the measurement of electric fields and gamma-ray radiations inside thunderclouds.

One major problem with flying balloon payloads inside a charged region is the charge build-up on the body of the payload which can significantly increase the measured electric field. In fact, the electric field measurements performed via aircraft have shown that charge build-up can enhance the background field up to two orders of magnitude. To overcome this challenge, an additional field mill sensor could be mounted to the top of the Styrofoam box to measure electric field amplitude on both ends of the payload. This would allow us to have two independent measurements of electric field and their polarity state and determine whether or not they were caused by the background electric field or the charge build-up.

In addition to charge build-up problem, payload should be fully wrapped inside a grounded layer of aluminum foil to minimize the distortion caused by the instruments onboard, and also to make the simulation of the setup easier. This requirement means that all GPS devices onboard should be placed inside a 2^{nd} box to be able to communicate with the satellite. One box will carry two field mill sensors (one on top and one on the bottom), the gamma-ray detector (Scintillator and GM tubes) and the FPGA board. This box will be completely insulated with aluminum sheets to provide a common ground. During the flight, data is being retrieved and timestamped using

RTC module. This clock is pre-synchronized with a second clock which will be placed inside the second box. The second box will carry all tracking devices including Spot Trace, GPS sensor and RockBLOCK. The GPS location of the payload will be timestamped using the second RTC module. Given that both clocks are synchronized before the flight, collected data could be easily correlated with time and location. This way GPS devices will be operating normally and there will be minimum interference with field mill sensors measurements.

One other challenge with the measurement of electric field signal is the high sampling rate required to construct the sinusoidal waveform. To reduce the sampling rate, field mill signal could be feed into an RMS to DC converter which converts the sinusoidal signal to DC signal which can be sampled at 10 to 100 Hz rate. This will reduce both the sampling rate and data writing to the SD card.

More work could be done towards the simulation of balloon payload inside gamma-ray glow region based upon relativistic feedback mechanism. This would give us a better estimate of the charged particles and gamma rays fluence and amplitude of electric field present near the source region. In addition, since the experimental calibration of the dual field mill setup seems to be difficult inside the lab, due to very high voltage that is required, an accurate modeling of the payload box inside a high-field region is needed to confirm the measured amplitude of the electric field mill. Furthermore, launching several balloon payloads at once would give us the benefit of multi-point measurements which improves the accuracy of the modeling. Collected data from simulation and balloon observation along with radar information (e.g., LMA and NLDN) would allow us to fully characterize the gamma-ray glows and correlate that with the initiation of lightning.

Another feature which could be added to the current design of the payload is an on-command cut-down system which would allow us to partially control the trajectory of the payload. During the thunderstorm season of the Florida, most of the released balloons travel eastward which carries the payload into ocean. This would make the recovery of the payloads both difficult and expensive. Adding an on-command system between the parachute and balloon would allow us to cut down the payload when it travels more than the recoverable distance. This cut-down system could be wire-

lessly connected to the RockBLOCK tracking module to send and receive cut-down commands on-demand.

APPENDIX A

POLARIZATION CALCULATIONS

Here we explain the method that is used to calculate the polarization and its error bars based on the maximum likelihood technique. The degree of linear polarization varies between 0 (non-polarized) and 1 (fully polarized). We assume that n is number of photons for each TGF event, P is the calculated value of polarization and φ is the angle with respect to the x-axis of the linear polarization direction.

$$\forall\, i \in C = \{0, 1, 2, ..., 1000\} : p_i = 0.001 \times i \tag{A.1}$$

Then, two numbers (n_1 and n_2) are drawn randomly from Poisson distributions with $\lambda_1 = n \times p_i$ and $\lambda_2 = n \times (1 - p_i)$ respectively such that n_1 is number of polarized photons, n_2 is the number of unpolarized photons and $n_{total} = n_1 + n_2$ is the total number of photons. Then,

$$\theta_{polarized} = A[n_1] = 0 \tag{A.2}$$

$$\theta_{unpolarized} = \pi \times (B[n_2] - 0.5) \tag{A.3}$$

where A and B are arrays with size n_1 and n_2 respectively and B is a uniform random distribution between 0 and 1. Based on those, $\theta_{polarized}$ and $\theta_{unpolarized}$ would be the angular distribution of polarized and unpolarized photons with respect to x-axis of linear polarization. After appending these arrays, total angular distribution of photons will follow as:

$$\theta_{total} = [\theta_{polarized}; \theta_{unpolarized}] \tag{A.4}$$

Then the polarization vector and density matrix for each photon are calculated as:

$$\varepsilon_x^j = cos(\theta_{total}) \tag{A.5}$$

$$\varepsilon_y^j = sin(\theta_{total}) \tag{A.6}$$

$$\rho_{\alpha\beta} = \frac{1}{n_{total}} \sum_{k=1}^{n_{total}} \begin{pmatrix} \varepsilon_x^k \varepsilon_x^k & \varepsilon_x^k \varepsilon_y^k \\ \varepsilon_y^k \varepsilon_x^k & \varepsilon_y^k \varepsilon_y^k \end{pmatrix} \tag{A.7}$$

Using the density matrix, the linear polarization degree and angle for each sample is calculated as:

$$P_j = \sqrt{4\rho_{12}^2 + (\rho_{11} - \rho_{22})^2} \tag{A.8}$$

$$\varphi_j = \frac{\rho_{12} + \rho_{21}}{\rho_{11} - \rho_{22}} \tag{A.9}$$

This calculation is repeated 100 times and the average polarization and angle are reported as:

$$\bar{P} = \frac{1}{100} \sum_{j=1}^{100} P_j \tag{A.10}$$

$$\bar{\varphi} = \sqrt{\frac{1}{100} \sum_{j=1}^{100} \varphi_j^2} \tag{A.11}$$

Then, for the lowest i-index that average polarization ($\bar{P}$) of total samples equals or exceeds the initial polarization (P), the P_i associated with that index would be stored as the best polarization. Also, for the i-index that half-sigma of average polarization distribution equals or exceeds (falls behind) the initial polarization (P), that P_i would be chosen as the lower bound (upper band) of polarization. An example of this method is shown with details in the Figure A.1 for P = 0.5. The distance between lower and upper bound would be selected as the margins of error of polarization degree.

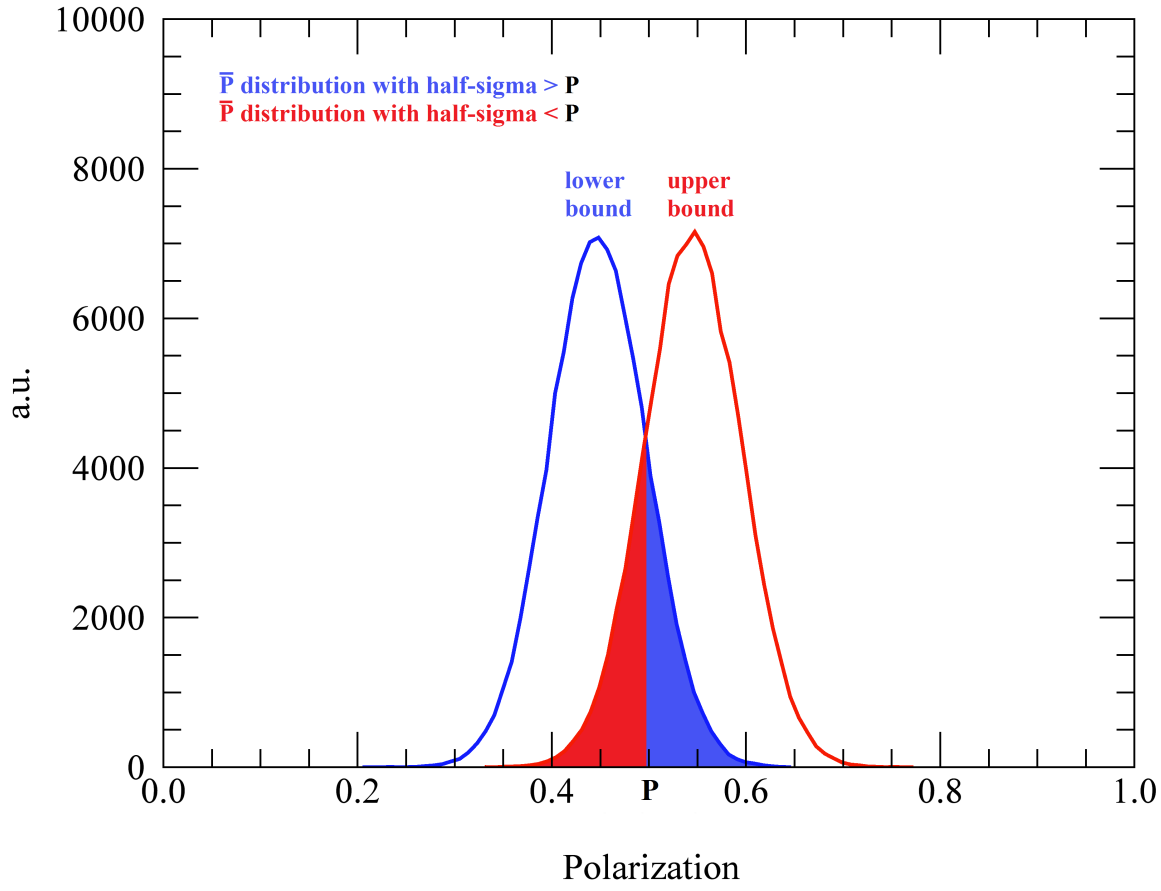

Figure A.1: Lower (upper) bound distribution of average polarization with half-sigma greater (smaller) than polarization. Here P is assumed to be 0.5, while lower and upper bound are approximately 0.45 and 0.55. Colored areas are covering half-sigma of each distribution.

BIBLIOGRAPHY

Alexeenko, V. V. et al. [2002], 'Transient variations of secondary cosmic rays due to atmospheric electric field and evidence for pre-lightning particle acceleration', *Phys. Lett. A* **301**, 299.

Arabshahi, S. et al. [2014], 'The energy spectrum of X-rays fromrocket-triggered lightning', *J. Geophys. Res. Atmos.* **120**, 10,951–10,963.

Babich, L. P. [2003], 'High-Energy Phenomena in Electric Discharges in Dense Gases', *Futurepast, Arlington* .

Babich, L. P., Donskoy, E. N. and Kutsyk, I. M. [2005], 'The feedback mechanism of runaway air breakdown', *Geophys. Res. Lett.* **32**, L09809.

Babich, L. P., Donskoy, E. N. and Roussel-Dupre, R. A. [2007], 'Study of relativistic electron avalanche enhancement in the atmosphere at low overvoltages due to avalanche bremsstrahlung', *Geomagn. Aeron.* **47**(4), 515–524.

Babich, L. P. et al. [1998], 'New data on space and time scales of relativistic runaway electron avalanche for thunderstorm environment: Monte Carlo calculations', *Phys. Lett. A* **245**, 460–470.

Babich, L. P. et al. [2001], 'Comparison of relativistic runaway electron avalanche rates obtained from Monte Carlo simulations and kinetic equation solution', *IEEE Trans. Plasma Sci.* **29**(3), 430–438.

Babich, L. P. et al. [2004], 'Fundamental parameters of a relativistic runaway electron avalanche in air', *Plasma Phys. Rep.* **30**, 616–624.

Bagheri, M. and Dwyer, J. R. [2016], 'An investigation of the possibility of detecting gamma-ray flashes originating from the atmosphere of Venus', *J. Geophys. Res. Space Physics* **121**, 9020–9029.

Bagheri, M., Dwyer, J. R. and McConnell, M. [2019], 'On the linear Polarization of TGFs and X rays from natural and rocket triggered lightning and its association with source geometry', *Under Review at JGR: Space Physics* .

Bateman, M. G. et al. [2007], 'A Low-Noise, Microprocessor-Controlled, Internally Digitizing Rotating-Vane Electric Field Mill for Airborne Platforms', *J. Atmos. Oceanic Technol.* **24**, 1245–1255.

Bazelyn, E. M. and Raizer, Y. P. [1998], 'Spark Discharge', *Boca Raton, Florida; CRC Press* p. 294.

Bengtsson, L. R. et al. [2013], 'Towards understanding the climate of Venus', *ISSI Scientific Report Series* **11**.

Berestetskii, V. B., Lifshitz, E. M. and Pitaevskii, L. P. [1982], 'Quantum Electrodynamics', *Pergamon Press* **Oxford**, 321–370.

Berger, K. [1978], 'Blitzstrom-Parameter von Aufwärtsblitzen', *Bull. Schweiz. Elektrotech.* **69**, 353–360.

Bezard, B. and de Bergh, C. [2007], 'Composition of the atmosphere of Venus below the clouds', *J. Geophys. Res.* **112**, E04S07.

Bloser, P. F. et al. [2005], 'GRAPE – A balloon-borne gamma-ray polarimeter experiment', *arXiv* **0508314**.

Borucki, W. J. et al. [1981], 'Optical search for lightning on Venus', *Geophys. Res. Lett.* **8**(3), 233–236.

Briggs, M. S. et al. [2010], 'First results on terrestrial gamma ray flashes from the Fermi Gamma-ray Burst Monitor', *J. Geophys. Res.* **115**, A07323.

Brunetti, M. et al. [2000], 'Gamma-ray bursts of atmospheric origin in the MeV energy range', *Geophys. Res. Lett.* **27**, 1599–1602.

Carlson, B. E., Gjesteland, T. and Ostgaard, N. [2011], 'Terrestrial gamma-ray flash electron beam geometry, fluence, and detection frequency', *J. Geophys. Res.* **116**, A11217.

Carlson, B. E., Lehtinen, N. G. and Inan, U. S. [2009], 'Terrestrial gamma ray flash production by lightning current pulses', *J. Geophys. Res.* **114**, A00E08.

Celestin, S. and Pasko, V. [2010], 'Soft collisions in relativistic runaway electron avalanches', *J. Phys. D: Appl. Phys.* **43**, 315206.

Celestin, S. and Pasko, V. [2011], 'Energy and fluxes of thermal runaway electrons produced by exponential growth of streamers during the stepping of lightning leaders and in transient luminous events', *J. Geophys. Res.* **116**, A03315.

Celestin, S. and Pasko, V. [2012], 'Compton scattering effects on the duration of terrestrial gamma-ray flashes', *Geophys. Res. Lett.* **39**, L02802.

Chauvin, M. et al. [2016], 'The design and flight performance of the PoGOLite Pathfinder balloon-borne hard X-ray polarimeter', *Exp. Astron.* **41**, 17–41.

Chilingarian, A., Mailyan, B. and Vanyan, L. [2012], 'Recovering of the energy spectra of electrons and gamma rays coming from the thunderclouds', *Atmos. Res.* **114**, 1–16.

Chilingarian, A. et al. [2010], 'Ground-based observations of thunderstorm-correlated fluxes of high-energy electrons, gamma rays, and neutrons', *Phys. Rev. D* **82**(4), 043009.

Chuang, K. W. et al. [1992], 'The spatial distribution of gamma-ray bursts from Pioneer Venus orbiter', *The Astrophys. J.* **391**, 242–245.

Chubenko, A. P. et al. [2000], 'Intense X-ray emission bursts during thunderstorms', *Phys. Lett. A* **275**, 90–100.

Cimino, J. B. and Elachi, C. [1979], 'Precipitation on Venus: Properties and possibilities of detection', *J. of Atmos. Sci.* **36**, 1168–1177.

Coleman, L. M. and Dwyer, J. R. [2006], 'Propagation speed of runaway electron avalanches', *Geophys. Res. Lett.* **33**, L11810.

Collier, A. B., Gjesteland, T. and Ostgaard, N. [2011], 'Assessing the power law distribution of TGFs', *J. Geophys. Res.* **116**, A10320.

Connaughton, V. et al. [2010], 'Associations between Fermi Gamma-ray Burst Monitor terrestrial gamma ray flashes and sferics from the World Wide Lightning Location Network', *J. Geophys. Res.* **115**(A12), A12307.

Cummer, S. A. et al. [2005], 'Measurements and implications of the relationship between lightning and terrestrial gamma ray flashes', *Geophys. Res. Lett* **32**, L08811.

Cummer, S. A. et al. [2015], 'Lightning leader altitude progression in terrestrial gamma-ray flashes', *Geophys. Res. Lett.* **42**, 7792–7798.

de Bergh, C. et al. [2006], 'The composition of atmosphere of Venus below 100 km altitude: an overview', *Planet. Space Sci.* **54**, 1389–1397.

Delitsky, M. L. and Baines, K. [2015], 'Storms on Venus: lightning-induced chemistry and predicted products', *Planet. Space Sci.* **113**, 184–192.

Dwyer, J. R. [2003], 'A fundamental limit on electric fields in air', *Geophys. Res. Lett.* **30**(20), 2055.

Dwyer, J. R. [2004], 'Implications of x-ray emission from lightning', *Geophys. Res. Lett.* **31**, L12102.

Dwyer, J. R. [2005], 'The initiation of lightning by runaway air breakdown', *Geophys. Res. Lett.* **32**(20), L20808.

Dwyer, J. R. [2007], 'Relativistic breakdown in planetary atmospheres', *Space Sci. Rev.* **14**(4), 042901.

Dwyer, J. R. [2008], 'Source mechanisms of terrestrial gamma-ray flashes', *J. Geophys. Res.* **113**, D10103.

Dwyer, J. R. and Smith, D. M. [2005], 'A comparison between Monte Carlo simulations of runaway breakdown and terrestrial gamma-ray flash observations', *Geophys. Res. Lett* **32**, L22804.

Dwyer, J. R., Smith, D. M. and Cummer, S. A. [2012], 'High-Energy atmospheric physics: terrestrial gamma-ray flashes and related phenomena', *Space Sci. Rev.* **173**(1-4), 133–196.

Dwyer, J. R. and Uman, M. A. [2014], 'The physics of lightning', *Physics Reports* **534**, 147–241.

Dwyer, J. R. et al. [2006], 'Runaway breakdown in the Jovian atmospheres', *Geophys. Res. Lett* **33**, L22813.

Dwyer, J. R. et al. [2011], 'High-speed x-ray images of triggered lightning dart leaders', *J. Geophys. Res.* **116**, D20208.

Dwyer, J. R. et al. [2015], 'Positron clouds within thunderstorms', *J. of Plasma Phys.* **81**(4), 475810405.

Eack, K. B. et al. [1996*a*], 'Initial results from simultaneous observation of X rays and electric fields in a thunderstorm', *J. Geophys. Res.* **101**(D23), 29637–29640.

Eack, K. B. et al. [1996*b*], 'X-ray pulses observed above a mesoscale convective system', *Geophys. Res. Lett.* **23**(21), 2915–2918.

Eack, K. B. et al. [2000], 'Gamma-ray emission observed in a thunderstorm anvil', *Geophys. Res. Lett.* **27**, 185–188.

Enoto, T. et al. [2017], 'Photonuclear reactions triggered by lightning discharge', *Nature* **551**, 481–484.

Evans, W. D. et al. [1979], 'Gamma-ray burst observations by Pioneer Venus orbiter', *Science* **205**(4401), 119–121.

Fishman, G. J. et al. [1994], 'Discovery of intense gamma-ray flashes of atmospheric origin', *Science* **264**(5163), 1313–1316.

Fishman, G. J. et al. [2011], 'Temporal properties of the terrestrial gamma- ray flashes from the Gamma-Ray Burst Monitor on the Fermi Observatory', *J. Geophys. Res.* **116**, A07304.

Fitzpatrick, G. et al. [2014], 'Compton scattering in terrestrial gamma-ray flashes detected with the Fermi gamma-ray burst monitor', *Phys. Rev. D* **90**(4), 043008.

Gjesteland, T. N. et al. [2010], 'Effects of dead time losses on terrestrial gamma ray flash measurements with the Burst and Transient Source Experiment', *J. Geophys. Res.* **115**, A00E21.

Gluckstern, R. L. and Hull, M. H. [1953], 'Polarization dependence of the integrated bremsstrahlung cross section', *Phys. Rev.* **90**, 1030–1035.

Grefenstette, B. W. et al. [2008], 'Time evolution of terrestrial gamma ray flashes', *Geophys. Res. Lett.* **35**(6), L06802.

Greiner, J. et al. [2012], 'GRIPS-Gamma-Ray Imaging, Polarimetry and Spectroscopy', *Exp. Astron.* **34**, 551–582.

Griffiths, R. F. and Phelps, C. T. [1976], 'A Model for Lightning Initiation Arising from Positive Corona Streamer Development', *J. Geophys. Res.* **81**, 3671–3676.

Gurevich, A. [1961], 'On the Theory of Runaway Electrons', *Sov. Phys. JETP* **12**(5), 904–912.

Gurevich, A. V., Milikh, G. M. and Roussel-Dupre, R. A. [1992], 'Runaway electron mechanism of air breakdown and preconditioning during a thunderstorm', *Phys. Lett. A* **165**, 463–467.

Hansell, S. A., Wells, W. K. and Hunten, D. M. [1995], 'Optical detection of lightning on Venus', *Icarus* **117**, 345–351.

Hare, B. M. et al. [2016], 'Ground-level observation of a terrestrial gamma ray flash initiated by a triggered lightning', *J. Geophys. Res. Atmos.* **121**, 6511–6533.

Hazelton, B. J. et al. [2009], 'Spectral dependence of terrestrial gamma-ray flashes on source distance', *Geophys. Res. Lett.* **36**, L01108.

Hill, J. E. et al. [2008], 'POET: POlarimeters for energetic transients', *arXiv* **0810.2499**.

Howard, J. M. et al. [2011], 'Measured close lightning leader-step electric field-derivative waveforms', *J. Geophys. Res.* **116**, D08201.

Kliore, A. J., Elachi, C. and Patel, I. [1979], 'Liquid content of the lower clouds of Venus as determined from Mariner 10 radio occultation', *Icarus* **37**(1), 51–72.

Knoll, G. F. [2010], 'Radiation Detection and Measurement', *John Wiley & Sons, New Jersey* **4th Edition**.

Krasnopolsky, V. A. [2006], 'A sensitive search for nitric oxide in the lower atmosphere of Venus and Mars: Detection on Venus and upper limit for Mars', *Icarus* **182**, 80–91.

Krasnopolsky, V. A. [2011], 'Atmospheric chemistry on Venus, Earth and Mars: main features and comparison', *Planet. Space Sci.* **59**, 952–964.

Landau, L. D. and Lifshitz, E. M. [1975], 'The Classical Theory of Fields', *Pergamon Press* **2**, 129–133.

Lehtinen, N. G., Bell, T. F. and Inan, U. S. [1999], 'Monte Carlo simulation of runaway MeV electron breakdown with application to red sprites and terrestrial gamma ray flashes', *J. Geophys. Res.* **104**, 24699–24712.

Lei, F. et al. [1996], 'Characteristics of COMPTEL as a polarimeter and its data analysis', *Astron. Astrophys. Suppl. Ser.* **120**, 695–698.

Levine, J. S. et al. [1982], 'Production of nitric oxide by lightning on Venus', *Geophys. Res. Lett.* **9**(8), 893–896.

Lin, R. P. et al. [2002], 'The Reuven Ramaty High-Energy Solar Spectroscopic Imager (RHESSI)', *Solar Physics* **210**, 3–32.

Liu, N. and Dwyer, J. R. [2013], 'Modeling Terrestrial Gamma-Ray Flashes Produced by Relativistic Feedback Discharges', *J. Geophys. Res.* **118**, 2359–2376.

Liu, N. Y. et al. [2012], 'Formation of streamer discharges from an isolated ionization column at subbreakdown conditions', *Phys. Rev. Lett.* **109**, 025002.

Lorenz, R. D. and Lawrence, D. [2015], 'Gamma rays and cosmic rays at Venus: The Pioneer Venus gamma ray detector and considerations for future measurements', *Planet. Space Sci.* **109**, 129–134.

Lotti, S. et al. [2012], 'Polarization Studies with NuSTAR', *Proc. SPIE: Space Telescopes and Instrumentation 2012: Ultraviolet to Gamma Ray* **8443**, 84434X.

MacGorman, D. R. and Rust, W. D. [1998], 'The electrical nature of storms', *Oxford University Press, New York* .

Marisaldi, M. et al. [2010], 'Detection of terrestrial gamma ray flashes up to 40 MeV by the AGILE satellite', *J. Geophys, Res.* **115**, A00E13.

Marisaldi, M. et al. [2015], 'Enhanced detection of terrestrial gamma-ray flashes by AGILE', *Geophys. Res. Lett.* **42**, 9481–9487.

Marshall, T., McCarthy, M. and Rust, W. [1995], 'Electric field magnitudes and lightning initiation in thunderstorms', *J. Geophys. Res.* **100**, 7097–7103.

May, M. M. [1951], 'On the polarization of high energy bremsstrahlung and of high energy pairs', *Phys. Rev.* **84**, 265–270.

McCarthy, M. and Parks, G. K. [1985], 'Further observations of X-rays inside thunderstorms', *Geophys. Res. Lett.* **12**, 393–396.

McConnell, M. L. et al. [2013], 'Plans for the next GRAPE balloon flight', *Proc. SPIE: UV, X-Ray, and Gamma-Ray Space Instrumentation for Astronomy XVIII* **8859**, 885909.

McConnell, M. L. et al. [2018], 'The continued development of a low energy Compton imager for GRB polarization studies', *Proc. SPIE: Space Telescopes and Instrumentation 2018: Ultraviolet to Gamma Ray* **10699**, 106992O.

Meegan, C. et al. [2009], 'The fermi gamma-ray burst monitor', *Astrophys. J.* **702**, 791.

Michael, M. et al. [2009], 'Highly charged cloud particles in the atmosphere of Venus', *J. Geophys. Res.* **114**, E04008.

Mills, F. P. and Allen, M. [2007], 'A review of selected issues concerning the chemistry in Venus' middle atmosphere', *Planet. Space Sci.* **55**, 1729–1740.

Moore, C. B. et al. [2001], 'Energetic radiation associated with lightning stepped-leaders', *Geophys. Res. Lett.* **28**, 2141–2144.

Moroz, V. I. [1981], 'The atmosphere of Venus', *Space Sci. Rev.* **29**, 3–127.

Moss, G. D. et al. [2006], 'Monte Carlo model for analysis of thermal runaway electrons in streamer tips in transient luminous events and streamer zones of lightning leaders', *J. Geophys. Res.* **111**, A02307.

Motz, J. W. [1956], 'Bremsstrahlung Polarization Measurements for 1.0-Mev Electrons', *Phys. Rev.* **104**, 557–562.

Nagai, Y., Kawamata, S. and Edano, Y. [1982], 'Observation of preceding leader and its downward traveling velocity in Utsunomiya district', *Res. Lett. Atmos. Electr.* **2**, 53–56.

Neubert, T. et al. [2019], 'The ASIM mission on the International Space Station', *Space Sci. Rev.* **215**, 26.

Nordheim, T. A. et al. [2015], 'Ionization of the Venusian atmosphere from solar and galactic cosmic rays', *Icarus* **245**, 80–86.

Olsen, H. and Maximon, L. C. [1959], 'Photon and electron polarization in high-energy bremsstrahlung and pair production with screening', *Phys. Rev.* **114**, 887–904.

Oreshkin, E. V. et al. [2012], 'Simulation of the runaway electron beam formed in a discharge in air at atmospheric pressure', *Phys. Plas.* **19**, 043105.

Ostgaard, N. T. et al. [2008], 'Production altitude and time delays of the terrestrial gamma flashes: Revisiting the Burst and Transient Source Experiment spectra', *J. Geophys. Res.* **113**, A02307.

Ostgaard, N. T. et al. [2012], 'The true fluence distribution of terrestrial gamma flashes at satellite altitude', *J. Geophys. Res.* **117**, A03327.

Ostgaard, N. et al. [2019], 'The Modular X- and Gamma-Ray Sensor (MXGS) of the ASIM Payload on the International Space Station', *Space Sci. Rev.* **215**(2), 23.

Parks, G. K. et al. [1981], 'X-ray enhancements detected during thunderstorm and lightning activities', *Geophys. Res. Lett.* **8**, 1176–1179.

Pasko, V. P., Inan, U. S. and Bell, T. F. [1998], 'Ionospheric effects due to electrostatic thundercloud fields', *Geophys. Res. Lett.* **25**, 2123–2126.

Peterson, D. et al. [2008], 'A brief review of the problem of lightning initiation and a hypothesis of initial lightning leader formation', *J. Geophys. Res.* **113**, D17205.

Rakov, V. A. and Uman, M. A. [2003], 'Lightning: physics and effects', *Cambridge University Press* .

Roos, M. et al. [1993], 'The upper clouds of Venus: determination of the scale height from NIMS-Galileo infrared data', *Planet. Space Sci.* **41**, 505–514.

Roussel-Dupre, R. A. et al. [2008], 'Physical processes related to discharges in planetary atmospheres', *Space Sci. Rev.* **137**, 51–82.

Russell, C. T., Strangeway, R. J. and Zhang, T. L. [2006], 'Lightning detection on the Venus Express mission', *Planet. Space Sci.* **54**, 1344–1351.

Russell, C. T. et al. [2007], 'Lightning on Venus inferred from whistler-mode waves in the ionosphere', *Nature* **450**, 661–662.

Russell, C. et al. [2011], 'Venus lightning: comparison with terrestrial lightning', *Planet. Space Sci.* **59**, 965–973.

Saleh, Z. et al. [2009], 'Properties of the X-ray emission from rocket-triggered lightning as measured by the Thunderstorm Energetic Radiation Array (TERA)', *J. Geophys. Res.* **114**, D17.

Scarf, F. L. and Russell, C. [1983], 'Lightning measurements from the Pioneer Venus', *Geophys. Res. Lett.* **10**(12), 1192–1195.

Schaal, M. M. et al. [2012], 'Spatial Energy Spatial and energy distributions of X-ray emissions from leaders in natural and rocket triggered lightning', *J. Geophys. Res.* **117**, D15201.

Schaal, M. M. et al. [2013], 'The angular distribution of energetic electron and X-ray emissions from triggered lightning leaders', *J. Geophys. Res. Atmos.* **118**, 11712–11726.

Shao, X., Hamlin, T. and Smith, D. M. [2010], 'A closer examination of terrestrial gamma-ray flash-related lightning processes', *J. Geophys. Res.* **115**, A00E30.

Singh, R. N. and Russell, C. [1986], 'Further evidence for lightning on Venus', *Geophys. Res. Lett.* **13**(10), 1051–1054.

Smith, D. M. et al. [2005], 'Terrestrial gamma-ray flashes observed up to 20 MeV', *Science* **307**(5712), 1085–1088.

Smith, D. M. et al. [2010], 'Terrestrial gamma ray flashes correlated to storm phase and tropopause height', *J. Geophys. Res.* **115**, A00E49.

Smith, D. M. et al. [2011*a*], 'A terrestrial gamma ray flash observed from an aircraft', *J. Geophys. Res.* **116**, D20124.

Smith, D. M. et al. [2011*b*], 'The rarity of terrestrial gamma-ray flashes', *J. Geophys. Res.* **38**(8), L08807.

Stanley, M. et al. [2006], 'A link between terrestrial gamma-ray flashes and intracloud lightning discharges', *Geophys. Res. Lett.* **33**, L06803.

Suarez-Garcia, E. et al. [2006], 'X-ray polarization of solar flares measured with RHESSI', *Solar Physics* **239**, 149–172.

Suszcynsky, D., Roussel-Dupré, R. and Shaw, G. [1996], 'Ground-based search for X rays generated by thunderstorms and lightning', *J. Geophys. Res.* **101**, 23505.

Svedhem, H. et al. [2007], 'Venus as a more Earth-like planet', *Nature* **450**, 629–632.

Takahashi, Y. J. et al. [2008], 'Lightning Detection by LAC Onboard the Japanese Venus Climate Orbiter, Planet-C', *Space Sci. Rev.* **137**, 317–334.

Tavani, M. et al. [2011], 'Terrestrial gamma-ray flashes as powerful particle accelerators', *Phys. Rev. Lett.* **106**, 018501.

Torii, T., T., M. T. and Hosono, T. [2002], 'Observation of gamma-ray dose increase associated with winter thunderstorm and lightning activity', *J. Geophys. Res.* **107**, 4324.

Torii, T. et al. [2009], 'Gradual increase of energetic radiation associated with thunderstorm activity at the top of Mt. Fuji', *Geophys. Res. Lett.* **36**, L13804.

Torii, T. et al. [2011], 'Migrating source of energetic radiation generated by thunderstorm activity', *Geophys. Res. Lett.* **38**, L24801.

Tran, M. D. et al. [2015], 'A terrestrial gamma-ray flash recorded at the Lightning Observatory in Gainesville, Florida', *J. Atmos. Sol. Terr. Phys.* **136**, 86–93.

Tsuchiya, H. et al. [2009], 'Observation of an energetic radiation burst from mountain-top thunderclouds', *Phys. Rev. Lett.* **102**, 255003.

Tsuchiya, H. et al. [2011], 'Long-duration gamma ray emissions from 2007 and 2008 winter thunderstorms', *J. Geophys. Res.* **116**, D09113.

Tzur, I. and Levin, Z. [1982], 'A one-dimensional model of the atmospheric electric field near the Venusian surface', *Icarus* **52**, 346–353.

Uman, M. A. [2001], 'The Lightning Discharge', *Academic Press, London, 1987, revised paperback edition, Dover, New York* .

Weisskopf, M. C., Elsner, R. F. and O'Dell, S. L. [2010], 'On understanding the figures of merit for detection and measurement of x-ray polarization', *Proc. SPIE* **7732**, 77320E.

Williams, E. R. [2010], 'Origin and context of C. T. R. Wilson's ideas on electron runaway in thunderclouds', *J. Geophys. Res.* **115**, A00E50.

Williams, M. A., Krider, E. P. and Hunten, D. M. [1983], 'Planetary lightning: Earth, Jupiter, and Venus', *Rev. of Geophys. and Space Phy.* **21**(4), 892–902.

Wilson, C. T. R. [1925], 'The electric field of a thunderstorm and some of its effects', *Proc. Phys. Soc. Lond.* **37**, 32D–37D.

Winkler, C. et al. [2003], 'The INTEGRAL mission', *A & A* **411**, L1–L6.

Yair, Y. G. et al. [2008], 'Updated review of planetary atmospheric electricity', *Space Sci. Rev.* **137**, 29–49.

Yonetoku, D. et al. [2011], 'Gamma-Ray Burst Polarimeter (GAP) aboard the Small Solar Power Sail Demonstrator IKAROS', *Publ. Astron. Soc. Japan.* **63**, 625–638.